

**Measurement of the London Penetration Depth in the  
Meissner State of NbSe<sub>2</sub> using Low Energy Polarized  
<sup>8</sup>Li.**

by

Md Masrur Hossain

A THESIS SUBMITTED IN PARTIAL FULFILMENT OF  
THE REQUIREMENTS FOR THE DEGREE OF

Master of Science

in

The Faculty of Graduate Studies

(Physics)

THE UNIVERSITY OF BRITISH COLUMBIA

October 5, 2007

© Md Masrur Hossain 2006

# Abstract

In this thesis, the Meissner state of NbSe<sub>2</sub> was investigated using low energy beam of spin polarized <sup>8</sup>Li. The <sup>8</sup>Li nuclear spin relaxation rate  $\frac{1}{T_1}$  was measured as a function of temperature and magnetic field. The spin relaxation rate is sensitive to low frequency nuclear spin dynamics of the host Nb spins and is strongly field dependent. This is used to determine the reduction in the magnetic field upon cooling into the Meissner state. Using a calculated implantation profile and a model field distribution, one can extract a measure of the absolute value of the London penetration depth  $\lambda$  in Meissner state. In addition, a model field distribution, assuming a suppression of order parameter near surface, was developed. In this case, we can extract another length scale which is related to the “coherence” length  $\xi$ . The value of  $\lambda$  depends on the model field distribution but is significantly longer than that obtained previously in the vortex state using  $\mu$ SR. From the measured internal magnetic field distribution, London penetration  $\lambda_L$  is extracted as a function of temperature. There is also evidence of the coherence peak in  $\frac{1}{T_1}$  of host nuclear spins.  $\lambda_L(T)$  follows the two-fluid model of superconductivity. Depending on the model for internal field distribution,  $\lambda_L(0)$  varies in the range (1795-2434)Å.

Md Masrur Hossain  
masrur@phas.ubc.ca

# Contents

<b>Abstract</b> . . . . .	ii
<b>Contents</b> . . . . .	iii
<b>List of Tables</b> . . . . .	v
<b>List of Figures</b> . . . . .	vi
<b>Acknowledgements</b> . . . . .	ix
<b>I Thesis</b>	<b>1</b>
<b>1 Introduction</b> . . . . .	<b>2</b>
<b>2 Superconductivity in London and Ginzburg-Landau Theories</b> . . . . .	<b>7</b>
2.1 London Theory . . . . .	7
2.2 Ginzburg-Landau Theory . . . . .	10
2.3 Zero field case near superconducting boundary . . . . .	11
2.4 BCS penetration depth . . . . .	17
<b>3 Time Dependence of Polarization and Relaxation</b> . . . . .	<b>21</b>
3.1 Evolution of $^8\text{Li}$ Spin Polarization in $\text{NbSe}_2$ in the Absence of Relaxation . . . . .	21
3.2 Korringa Relaxation & Knight Shift . . . . .	26
3.3 Low Field Spin Relaxation from Fluctuating Dipolar Fields . . . . .	31
<b>4 Experimental</b> . . . . .	<b>34</b>
4.1 Beamline Properties and Spectrometer . . . . .	34
4.2 The sample . . . . .	37
4.3 Measurement of Polarization in Low Field . . . . .	41
4.3.1 $P(t)$ in short pulse method . . . . .	41

---

4.3.2	P(t) in Long pulse method . . . . .	41
<b>5</b>	<b>Measurements and Results . . . . .</b>	<b>44</b>
5.1	Normal State in High Magnetic Field . . . . .	44
5.1.1	Korringa Relaxation . . . . .	44
5.1.2	Dipolar Broadening of the Resonance . . . . .	44
5.2	Low Field Measurements in the Normal State . . . . .	49
5.3	Low Field Measurements in the Meissner State . . . . .	52
5.4	Low Field Measurements in the Vortex State . . . . .	55
5.5	Stopping Distribution . . . . .	56
5.6	Analysis and fitting to determine $\lambda_L$ and $\xi$ . . . . .	58
<b>6</b>	<b>Summary &amp; Conclusions . . . . .</b>	<b>68</b>
	<b>Bibliography . . . . .</b>	<b>70</b>
<b>A</b>	<b>Low Field Spin Relaxation from Fluctuating Dipolar Fields</b>	<b>74</b>

## List of Tables

5.1	Penetration depth $\lambda_L(0)$ and coherence length $\xi(0)$ at $T = 0$	63
5.2	Average magnetic field, calculated using parameter in two models. . . . .	64
5.3	Penetration depth $\lambda_L$ and coherence length $\xi$ at temperature $T = 0K$ , using a common initial amplitude for fitting. . . . .	64
5.4	Average magnetic field, in two models, using parameters from table 5.3 . . . . .	64

# List of Figures

1.1	Critical temperature history. . . . .	4
2.1	Magnetic field, as it enters a superconducting sample, according to the London model. . . . .	9
2.2	(a) Numerical solution ( $B_{\text{nsol}}$ ) and its phenomenological fit ( $B_{\text{phen}}$ as given in Eq. 2.41) of the magnetic field in G-L theory. (b) Difference between them. $\xi = 150\text{\AA}$ and $\lambda_L = 2100\text{\AA}$ in both figures. . . . .	16
2.3	Typical density of states in a superconductor. The dashed line represents the normal state while the solid line represents the superconducting state. . . . .	18
2.4	Temperature dependence of the superconducting energy gap in the weak coupling limit of BCS interaction. . . . .	20
3.1	Time integrated polarization, as a function of magnetic field, showing resonant dips at level crossings with a single neighboring Nb. . . . .	24
3.2	Time integrated polarization in low magnetic fields. . . . .	25
3.3	Functions $f(E)$ , $1 - f(E)$ , and $f(E)[1 - f(E)]$ . The thicker bell-shaped curve shows $f(E)[1 - f(E)]$ . . . . .	30
3.4	Typical spectral density plot. . . . .	33
4.1	A schematic of the experimental layout. The 28 KeV $^8\text{Li}^+$ ion beam is neutralized in the Na cell and then reionized in the He cell. In between, the beam is optically pumped with a laser tuned to the D1 optical transition of the $^8\text{Li}$ atom. The resulting polarized beam is guided to $\beta$ -NMR and $\beta$ -NQR spectrometers. . . . .	35
4.2	Optical Pumping scheme for polarizing $^8\text{Li}$ . . . . .	36

---

4.3	A schematic of the spectrometer for $\beta$ -detected nuclear resonance. The spin polarization is perpendicular to the beam direction. The principal axis of the electric field gradient at the $^8\text{Li}$ stopping site must have a component along $\hat{z}$ in order for a signal to be detected at zero applied field. . . . .	38
4.4	(a) Polarization $P_z(B)$ for both helicities (b) Normalized asymmetry is found by subtracting “down” helicity from “up” helicity to remove the background effect. . . . .	39
4.5	Top: $\text{NbSe}_2$ cross-section (in $11\bar{2}0$ plane). Bottom: Three dimensional structure of $2\text{H-NbSe}_2$ . . . . .	40
4.6	(a) Beam is on between time (0,4)s. (b) Schematic polarization $P(t)$ as a function of time. . . . .	43
5.1	The time evolution of normalized spin polarization $^8\text{Li}$ in $\text{NbSe}_2$ in a magnetic field of 3T applied along the c-axis. The time differential measurements were done in short pulse mode. The solid lines are fits to a single exponential without any background. . . . .	45
5.2	Comparison between spin relaxation of Li in Ag and $\text{NbSe}_2$ as a function of temperature. The applied field along c-axis is 3T. . . . .	46
5.3	The $\beta$ -NMR resonance in $\text{NbSe}_2$ as a function of field and orientation. The top two scans were taken with the field parallel to the c-axis but at very different fields; whereas, the bottom scan is with the field perpendicular to the c-axis. The temperature is 10K in all cases and so there is no line broadening due to $^8\text{Li}$ motion. . . . .	47
5.4	Three different field spectra and the corresponding fits. . . . .	50
5.5	Dependence of relaxation rate on magnetic field at $T = 8\text{K}$ . . . . .	51
5.6	Time differential spectra at three temperatures, 3.75K, 6.15K and 6.4K, in long pulse method. Applied magnetic field $B = 30\text{G}$ for all the runs. . . . .	53
5.7	Comparison of average relaxation rate between the vortex state and the Meissner state. . . . .	54
5.8	Three time integrated spectra at $B = 125\text{G}$ . Solid lines represent fitted baseline. Resonance line shape changes due to the asymmetrical field distribution in the vortex state. . . . .	57
5.9	Monte Carlo calculated stopping distribution $\rho(x)$ . Maximum depth $^8\text{Li}$ reaches, at energy 28KeV, is $\approx 4100\text{\AA}$ and the profile is centered at $\approx 1360\text{\AA}$ . . . . .	59

---

5.10	Penetration depth as a function of temperature for an exponential model for $B(x)$ . . . . .	61
5.11	Penetration depth and coherence length as a function of temperature. . . . .	62
5.12	Penetration depth as a function of temperature for an exponential model for $B(x)$ with average overall amplitude. . . . .	65
5.13	Penetration depth and coherence length as a function of temperature with average overall amplitude, for “ $\xi$ model”. . . . .	66
A.1	Typical correlation function. . . . .	78

# Acknowledgements

I would like to thank my supervisor, Professor Rob Kiefl, for his guidance and insight. I would also like to thank Professor Andrew MacFarlane for his guidance and thanks to my colleagues and coworkers D. Wang, Z. Salman, K.H. Chow, S. Daviel, T.A. Keeler, G.D. Morris, R.I. Miller, T.J. Parolin and H. Saadaoui at  $\beta$ -NMR group in TRIUMF. Special thanks to R.I. Miller for helping me with the MINUIT fitting routine.

Also thanking L<sup>A</sup>T<sub>E</sub>X



CTAN lion drawing by Duane Bibby; thanks to [www.ctan.org](http://www.ctan.org)

**Part I**  
**Thesis**

# Chapter 1

## Introduction

Historically superconductivity has played an important role in condensed matter physics. Before the discovery of the phenomena of superconductivity, it was known that the resistivity of a metal drops with decreasing temperature. Resistivity in metals is generally attributed to electron-phonon scattering, the rate of which is proportional to the thermally excited phonons. However, the number of thermally excited phonons is always finite above absolute zero and thus the resistivity should always be finite at any finite temperature. Consequently, K. Onnes' discovery of virtual absence of resistivity in Mercury below 4.15K, in 1911 [1] was rather surprising. Soon after, in 1913, Lead was found to be superconducting below 7.2K and after 17 years of this discovery, niobium was found to be superconducting at 9.2K. The virtual absence of resistance in superconductor has been demonstrated by experiments with persistent currents in superconducting rings. Such currents have a decay time of magnitude of  $10^5$  years. Applications of superconductivity include very high-current transmission lines, high-field magnets and magnetic levitation. In 1954, the first successful superconducting magnet was made using Nb wire, which produced a field of 0.7T at 4.2K. In 1960, persistent current in a solenoid was used to provide the magnetic field for a solid state maser. This was probably the first commercial application of superconductivity.

The other important characteristic beyond zero resistivity is the phenomenon of the Meissner effect in which magnetic field is expelled [2] out of a sample when it's cooled below the so called critical temperature  $T_c$ . The phenomenon of the Meissner effect is different from perfect diamagnetism. In perfect diamagnetism, currents are generated to oppose any change in applied field. However, if the sample already had non-zero magnetic flux through it, cooling through  $T_c$  wouldn't make any change in the field whereas, in the Meissner effect, the field would be expelled from the sample when cooled below  $T_c$ .

This phenomenon of the Meissner effect led London brothers [3] to propose equations to predict how the field is excluded from the sample and in particular, the field penetration near the surface.

London's theory was later (1950) derived from the theory of Ginzburg and Landau [4] (GL), who described superconductivity in terms of a macroscopic complex order parameter  $\phi$  which roughly dictates the extent to which a system is ordered. In the case of superconductivity, the amplitude of order parameter is proportional to superconducting electron density.

Although the phenomenological GL theory had been successful, the microscopic theory only came in 1957 from J. Bardeen, Leon Cooper and John Schrieffer [5]. The carriers of supercurrents were shown to be a pair of electrons ("Cooper pairs" [6]) with opposite spin and momentum. In 1986, J.G. Bednorz and K.A. Muller [7] discovered superconductivity in  $\text{La}_{2-x}\text{Ba}_x\text{CuO}_4$  at 35K, thus initiating the era of high-temperature superconductivity. Although met with initial skepticism, the observations were validated when Uchida *et. al.* and Chu *et. al.* reproduced original results in 1987. The same year, scientists produced Lanthanum compound  $\text{La}_{2-x}\text{Sr}_x\text{CuO}_4$  which went superconducting  $\sim 40\text{K}$ . In subsequent years, remarkable progress has been made in increasing the critical temperature as shown in Fig 1.1.

Besides having a critical temperature  $T_c$ , superconductors also have critical magnetic fields associated with them, above which their properties change. In this respect, superconductors are classified in two broad categories, i) Type I, in which the material becomes normal above a critical magnetic field  $H_{c1}$ . ii) Type II, in which the material has two critical magnetic fields  $H_{c1}$  and  $H_{c2}$ . In type II, at  $H < H_{c1}$ , the sample remains in Meissner state and at  $H_{c1} < H < H_{c2}$ , magnetic field penetrate sample in quantized vortices and for  $H > H_{c2}$ , it becomes normal. Two other parameters characterize superconductivity in general, namely the coherence length  $\xi$  and the magnetic penetration depth  $\lambda$ . The coherence length  $\xi$  is the distance over which order parameter  $\phi$  varies appreciably and penetration depth  $\lambda$  is the depth over which shielding currents circulate to expel the applied external field.  $\lambda$  and  $\xi$  are two fundamental length scales in superconductivity. Other parameters of interest such as Ginzburg-Landau parameter  $\kappa = \frac{\lambda}{\xi}$ , two critical fields  $H_{c1}$ ,  $H_{c2}$ , thermodynamical critical field  $H_c$  may be derived from them.

Niobium compounds such as  $\text{Nb}_3\text{Sn}$  and  $\text{Nb}_3\text{Ti}$  have dominated research in conventional superconductivity since they have the high critical temperature values required for superconducting magnets.  $\text{NbSe}_2$  belongs to a transition metal dichalcogenides which have received considerable attention for their very interesting physical properties, such as superconductivity and existence of a charge density wave transition. Due to the anisotropy, the magnetization depends on the angle which the applied field makes with the c-axis. In a layered structure such as  $\text{NbSe}_2$ , the c-axis is generally perpen-

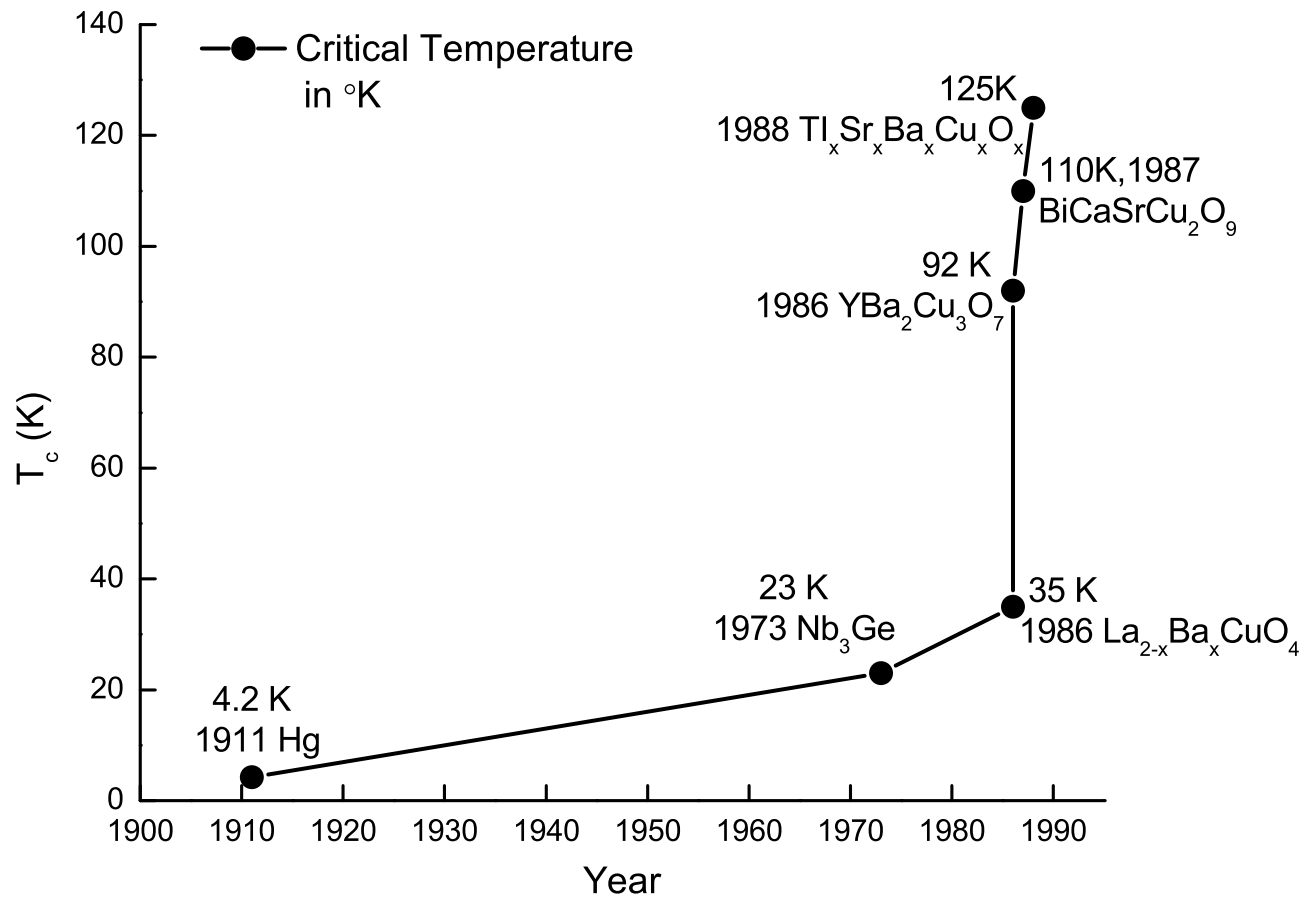


Figure 1.1: Critical temperature history.

pendicular to the plane. NbSe<sub>2</sub> is a quasi 2D crystal where bonding within the layers is strong and the bonding in between the layers is weak.

Until now, the penetration depth has been measured in the vortex state via muon spin rotation [8] and using microwave techniques [9, 10, 11, 12]. In vortex state measurement, Sonier *et al.* used a GL model for magnetic field distribution to extract  $\lambda$  as a function of applied magnetic field. However, it was mentioned that  $\lambda_{ab}$  measured is an effective penetration depth which is model dependent. Consequently, one may expect some difference in  $\lambda$  measured in the Meissner state where there are no vortices.

The microwave techniques used in [9, 10, 11, 12] reported London penetration depth for a number of high- $T_c$  superconductors. The microwave techniques are well-suited to measuring temperature dependence of  $\lambda$  but generally not very sensitive to the absolute value of  $\lambda$ . With the microwave techniques, one obtains some averaged macroscopic penetration depth.

The present experiment is sensitive to the absolute values of the penetration depth and the coherence length in the Meissner state. The relaxation rate  $\frac{1}{T_1}$ , of the <sup>8</sup>Li probe, is dependent on the magnetic field that the <sup>8</sup>Li sees inside NbSe<sub>2</sub>. In a sense, our method [13][14] is a direct way of measuring  $\lambda(T)$  and  $\xi(T)$  since the functional dependence of magnetic field on depth and stopping distribution of probe <sup>8</sup>Li inside the superconductor uniquely determines the relaxation rates, thereby giving  $\lambda(T)$  and in some circumstances,  $\xi(T)$ . The penetration depth is important, since, for example, it is often used to distinguish between different types of superconductivity since, at low temperatures,  $\lambda(T)$  reflects change in the superfluid density. For example,  $\lambda(T)$  is exponentially dependent on temperature in a conventional *s*-wave BCS superconductivity, whereas, in a *d*-wave superconductivity  $\lambda(T)$  is linear in  $T$ . Although the pairing mechanism of NbSe<sub>2</sub> is thought to be that of *s*-wave BCS type, other possible pairing states involving complicated gap functions, have been suggested [15][16][17][18] for other materials such as YBa<sub>2</sub>Cu<sub>3</sub>O<sub>7- $\delta$</sub> . Thus an accurate determination of  $\lambda(T)$  is one way to probe the symmetry of the pairing state.

Recently, it has been suggested that there are two energy gaps in NbSe<sub>2</sub>. This phenomenon has emerged as an explanation for anomalous properties [19] of some *s*-wave superconductors. Interest in the possibility of a double gap is enhanced by the peculiar properties [20] of the 39K superconductor MgB<sub>2</sub>. Since NbSe<sub>2</sub> has a similar planar quasi 2D crystal structure, it was speculated that similar characteristics may also be present in NbSe<sub>2</sub>. Evidence for a second gap in NbSe<sub>2</sub> has since been reported [21][22][23].

In this thesis, we measure a reduction of magnetic field  $B(x)$  as it enters the sample, via the change of nuclear relaxation rate  $\frac{1}{T_1}$ . For an exponen-

---

tially decaying magnetic field, we have only one free parameter, namely the penetration depth  $\lambda_L$ . However, with imperfections on surface, there may be suppression of the order parameter  $\phi$  near the surface thereby introducing a different form for  $B(x)$ . The suppression is thought to be dominant on the range of ‘coherence’ length  $\xi$ . In our model,  $\phi$  varies appreciably within a distance of  $2\sqrt{2}\xi$ . In this case, there are two free parameters  $\lambda$  and  $\xi$ .

In chapter 2, there is an introduction to London and Ginzburg theory and the functional dependence of magnetic field on  $\lambda$  and  $\xi$ . This will be followed by a discussion on BCS superconductivity as it pertains to NbSe<sub>2</sub>.

Chapter 3 contains a discussion of the various mechanisms which lead to time dependence of the nuclear polarization. This includes <sup>8</sup>Li-Nb nuclear Korringa relaxation which is dominant in high magnetic field.

Chapter 4 contains a discussion on experimental setup. This will be followed by a discussion on NbSe<sub>2</sub> structure and on polarization as function of time in two methods of measurement.

The experimental results of measurements will be presented in the chapter 5. I will show that the Korringa relaxation in NbSe<sub>2</sub> is an order of magnitude smaller compared to Ag. I will then discuss the  $\frac{1}{T_1}$  measurements in the vortex state and in the Meissner state. The values of  $\lambda$  and  $\xi$  will be extracted from these measurements according to two models for the internal field distribution. I shall then show that the extracted  $\lambda$  favors a model with the order parameter is suppressed at the surface.

Chapter 6 contains a brief discussion of the results.

## Chapter 2

# Superconductivity in London and Ginzburg-Landau Theories

### 2.1 London Theory

We consider the penetration depth in the Meissner state of a type II superconductor. Below  $H_{c1}$ , the London equations provide a good description of the electromagnetic properties. The relevant Maxwell's equation is

$$\vec{\nabla} \times \vec{E} = -\frac{1}{c} \frac{\partial \vec{B}}{\partial t}. \quad (2.1)$$

In the classical Drude model of electrical conductivity, we have

$$\vec{F} = -m \frac{\vec{v}}{\tau} - e\vec{E} = m \frac{d\vec{v}}{dt}, \quad (2.2)$$

where  $\vec{v}$  is the average velocity of the electrons,  $m$  is the mass of an electron,  $\vec{E}$  is the electric field the electrons are in and  $\tau$  is the relaxation time, i.e., roughly the time required to bring the drift velocity to zero if electric field was suddenly set to zero. In a normal metal, the competition between the scattering and the acceleration in Eq. 2.2 leads to a steady state average velocity

$$\vec{v} = \frac{e\vec{E}\tau}{m}. \quad (2.3)$$

Assuming  $n$  conduction electrons per unit volume, we get the electric current density via Ohm's Law,

$$\vec{J} = ne\vec{v} = \left( \frac{ne^2\tau}{m} \right) \vec{E} = \sigma \vec{E}. \quad (2.4)$$

To describe superconductivity, London assumed that a certain density of electrons  $n_s$  experience no relaxation i.e., letting  $\tau_s$  in Eq. 2.2 go to infinity.

This leads to

$$\frac{d\vec{J}_s}{dt} = \left( \frac{n_s e^2}{m} \right) \vec{E}, \quad (2.5)$$

where  $n_s$  is density of the superconducting carriers. Taking curl on both side of the Eq. 2.5, we get

$$\frac{m}{n_s e^2} \left( \vec{\nabla} \times \frac{d\vec{J}_s}{dt} \right) = \vec{\nabla} \times \vec{E}. \quad (2.6)$$

Substituting Maxwell Eq. 2.1 in 2.6, we obtain the second London equation

$$\frac{mc}{n_s e^2} \left( \vec{\nabla} \times \frac{d\vec{J}_s}{dt} \right) + \frac{d\vec{B}}{dt} = 0. \quad (2.7)$$

Interchanging the order of differentiation with respect to space and time in Eq. 2.7, London postulated

$$\frac{mc}{n_s e^2} \left( \vec{\nabla} \times \vec{J}_s \right) + \vec{B} = 0. \quad (2.8)$$

Assuming no time varying electric field, another Maxwell equation connects  $\vec{J}_s$  with  $\vec{B}$  with the equation

$$\vec{J}_s = \frac{c}{4\pi} \left( \vec{\nabla} \times \vec{B} \right) \quad (2.9)$$

Substituting Eq. 2.9 into Eq. 2.8, we get

$$\begin{aligned} \lambda_L^2 \left( \vec{\nabla} \times \vec{\nabla} \times \vec{B} \right) + \vec{B} &= 0, \\ \lambda_L^2 \nabla^2 \vec{B} + \vec{B} &= 0, \end{aligned} \quad (2.10)$$

where

$$\frac{1}{\lambda_L^2} = \frac{4\pi n_s e^2}{mc^2}. \quad (2.11)$$

In a vacuum-superconductor interface (which is also the case in our experiment), the solution of Eq. 2.10 is given by

$$B(x) = B(0) \exp \left( -\frac{x}{\lambda_L} \right) \quad (2.12)$$

and is schematically shown in Fig 2.1 The quantity  $\lambda_L$  is known as London penetration depth and  $\lambda_L^{-2} \propto n_s$  (i.e, superfluid density). The most important success of the London Eqs. 2.9 and 2.10 is that a static magnetic

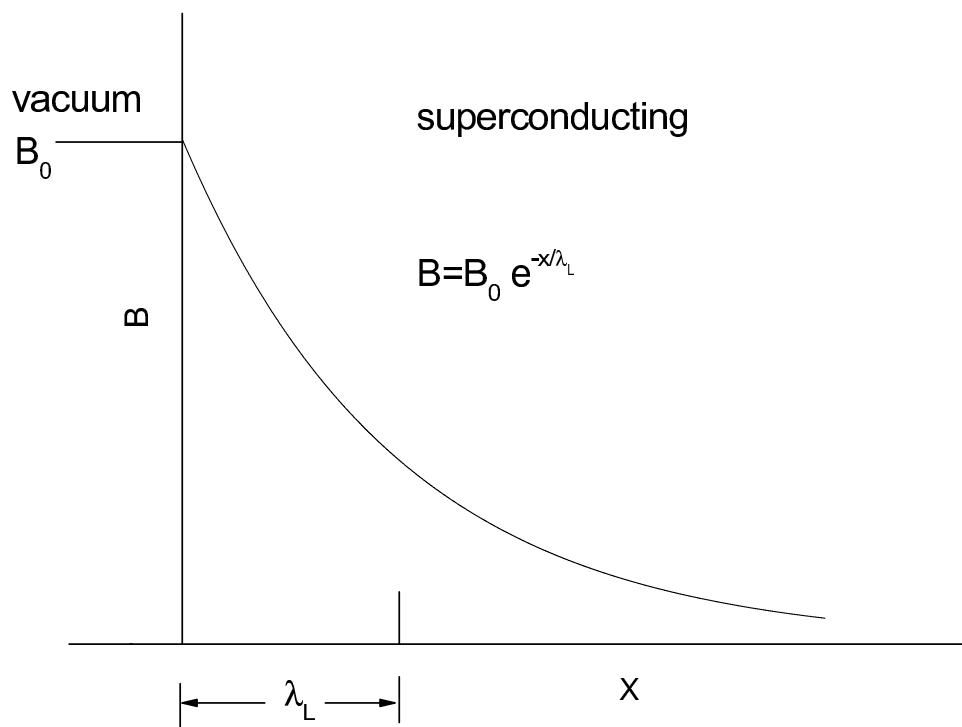


Figure 2.1: Magnetic field, as it enters a superconducting sample, according to the London model.

field is screened from the interior of a bulk superconductor over a characteristic penetration depth  $\lambda_L$ . As one approaches the critical temperature  $T_c$ ,  $n_s \rightarrow 0$  continuously and as a consequence,  $\lambda_L(T)$  diverges as  $T \rightarrow T_c$ , according to Eq. 2.11.

The Eq. 2.12 is true for  $T = 0$ . Gorter and Casimir [24] found that good agreement with early experiments could be obtained if one assumes, what is now known as two-fluid model,

$$n_s(T) = n \left[ 1 - \left( \frac{T}{T_c} \right)^4 \right]. \quad (2.13)$$

By substituting Eq. 2.13 in Eq. 2.11, we get the penetration depth as

$$\lambda_L(T) = \frac{\lambda_L(0)}{\left[ 1 - \left( \frac{T}{T_c} \right)^4 \right]^{\frac{1}{2}}}. \quad (2.14)$$

with

$$\lambda_L(0) = \sqrt{\frac{mc^2}{4\pi ne^2}}. \quad (2.15)$$

## 2.2 Ginzburg-Landau Theory

A phenomenological approach to superconductivity by Ginzburg and Landau (GL, hereafter) is discussed in this section. We shall derive the functional form of the magnetic field as it penetrates the sample, in the Meissner state.

Order parameter: GL theory assumes that the super-electrons(holes) of mass  $m^*$ , charge  $e^*$  and density  $n_s^*$  are connected by relationships

$$\begin{aligned} m^* &= 2m, \\ e^* &= \pm 2e, \\ n_s^* &= \frac{1}{2}n_s, \end{aligned} \quad (2.16)$$

with their hole(electron) counterparts  $m$ ,  $\pm e$ , and  $n_s$  respectively. The GL theory is formulated in terms of complex order parameter  $\phi(\vec{r})$  which may be written as

$$\phi(\vec{r}) = |\phi(\vec{r})|e^{i\Theta}. \quad (2.17)$$

where  $\Theta$  is the phase and  $|\phi(\vec{r})|$  is the modulus of order parameter  $\phi(\vec{r})$ .  $\phi(\vec{r})$  plays a role in superconductivity similar to the role of wavefunction in quantum mechanics. The superelectron density is given by

$$n_s^* = |\phi(\vec{r})|^2. \quad (2.18)$$

and  $|\phi|$  increases from zero as we go below the critical temperature  $T_c$ .

Ginzburg and Landau (G-L) assumed that close to the transition (from superconducting to normal) temperature  $T_c$ , the Gibbs free energy per unit volume  $G_s(\phi)$  may be expanded as a local functional as

$$G_s[\phi] = G_n + \frac{1}{2m^*} \times \left| (-i\hbar\vec{\nabla} + e^*\vec{A})\phi \right|^2 + \frac{H^2}{8\pi} + a|\phi|^2 + \frac{b}{2}|\phi|^4, \quad (2.19)$$

where  $G_n$  is free-energy density of normal state, ' $H$ ' is the applied field and ' $a$ ' and ' $b$ ' are functions of temperature only. To get  $\phi(\vec{r})$ ,  $G_s[\phi]$  is minimized with respect to variations in the order parameter  $\phi(\vec{r})$ . Taking derivative with respect to  $\phi^*$  with  $\phi$  constant, the first GL equation gives

$$\frac{1}{2m^*} \left| -i\hbar\vec{\nabla} + e^*\vec{A} \right|^2 \phi - a\phi - b|\phi|^2\phi = 0. \quad (2.20)$$

The free energy is also a minimum with respect to variations in vector potential  $\vec{A}$  and we get the second GL equation

$$\vec{\nabla} \times (\vec{\nabla} \times \vec{A}) + i\hbar e^*(\phi^*\vec{\nabla}\phi - \phi\vec{\nabla}\phi^*) + \frac{e^{*2}}{m^*}\vec{A}|\phi|^2 = 0. \quad (2.21)$$

The Eqs. 2.20 and 2.21 are the two coupled differential equations which can be solved to determine the properties of superconductors. In the later sections, we will see that the constants in Eq. 2.20 and Eq. 2.21 naturally lead to spatial dependence of the order parameter on the scale of  $\xi$  and a dependence of the magnetic field on the scale of  $\lambda_L$ .

### 2.3 Zero field case near superconducting boundary

In this section we consider a superconducting material having a vacuum boundary. To determine the functional dependence of order parameter  $\phi(r)$  on depth, one must impose some boundary conditions. Assuming that no current flows into the surface, according to Tinkham [25] and de Gennes [26],

$$\left( \frac{\hbar}{i}\vec{\nabla} - \frac{e^*}{c}\vec{A} \right) \phi \Big|_n = 0. \quad (2.22)$$

$\vec{A}$  can be set to zero in the absence of a magnetic field since  $\vec{B} = \vec{\nabla} \times \vec{A}$ . Then, from the second GL Eq. 2.21, we obtain,

$$-\frac{\hbar^2}{2m^*}\nabla^2\phi + a\phi + b|\phi|^2\phi = 0. \quad (2.23)$$

We can choose  $\phi$  to be real as the phase is constant. We assume that the right half-space ( $x > 0$ ) is filled with superconductor and that the left side half-space is vacuum and thereby  $\phi$  is only function of  $x$  and  $\vec{\nabla}$  has only  $x$  component and the Eq. 2.23 may be written as

$$-\frac{\hbar^2}{2m^*} \frac{d^2\phi}{dx^2} + a\phi + b|\phi|^2\phi = 0. \quad (2.24)$$

Changing variables by setting  $\phi = \left(\frac{|a|}{b}\right)^{\frac{1}{2}} f$  and setting  $\eta = \frac{x}{\xi}$  where

$$\xi^2 = \frac{\hbar^2}{2m^*|a|}, \quad (2.25)$$

the Eq. 2.24 becomes

$$\frac{d^2f}{d\eta^2} + f(1 - f^2) = 0. \quad (2.26)$$

To solve the Eq. 2.26, one needs to impose boundary conditions on  $f$ . There is some uncertainty here over the exact boundary condition in a vacuum-superconductor interface. One such condition, proposed by Poole [27] is that the order parameter (and thereby  $f$ ) is zero at surface and takes its full value deep inside the superconductor, i.e,

$$\begin{aligned} f(\eta = 0) &= 0, \\ f(\eta = \infty) &= 1 \end{aligned} \quad (2.27)$$

yielding

$$f = \tanh\left(\frac{\eta}{\sqrt{2}}\right), \quad (2.28)$$

where

$$\phi_\infty = \left(\frac{|a|}{b}\right)^{\frac{1}{2}}, \quad (2.29)$$

giving

$$\phi = \phi_\infty \tanh\left(\frac{x}{\sqrt{2}\xi}\right). \quad (2.30)$$

An alternative assumption mentioned by Tinkham [25] is that the order parameter remains at its maximum value throughout the sample, even at boundary, i.e,

$$f = 1 \quad x \geq 0, \quad (2.31)$$

giving

$$\phi = \phi_\infty. \quad (2.32)$$

I will use both forms (Eq. 2.30 and 2.32) to extract  $\xi$  and  $\lambda_L$ .

Even though the above  $\phi(r)$  has been formulated in absence of magnetic field, the functional form of  $\phi(r)$  is valid even in presence of an applied field with  $\xi$  depending on field and temperature.

We can use Eq. 2.30 and Eq. 2.32 to determine the magnetic field inside the superconductor. For our semi-infinite geometry and for a constant magnetic field  $B_o$  outside superconductor ( $x < 0$ ), the vector potential may be written as

$$\vec{A} = A_y(x)\hat{j} \quad (2.33)$$

where

$$A_y(x) = xB_o + A_o, \quad x < 0 \quad (2.34)$$

and  $A_o$  is a constant for continuity of equation at  $x = 0$ . C. Poole assumed [27] that the phase of the order parameter is constant everywhere throughout the superconductor such that there is no current flowing into the superconductor. The constant phase may thereby conveniently be set equal to 0. It follows from the current density equation that

$$J_y(x) = -\frac{e^{*2}|\phi(x)|^2}{m^*}A_y(x). \quad (2.35)$$

The second GL equation yields

$$\frac{d^2A_y(x)}{dx^2} = \frac{\mu_o e^{*2}|\phi(x)|^2}{m^*}A_y(x). \quad (2.36)$$

Now, for the order parameter  $\phi(r)$  is given in Eq. 2.30, the Eq. 2.36 may be written as,

$$\begin{aligned} \frac{d^2A_y(x)}{dx^2} &\equiv \frac{dB(x)}{dx} \\ &= \tanh^2\left(\frac{x}{\sqrt{2}\xi}\right) \frac{A_y(x)}{\lambda_L^2}, \end{aligned} \quad (2.37)$$

where

$$\lambda_L^2 = \frac{m^*}{\mu_o e^{*2}|\phi_\infty|^2}. \quad (2.38)$$

By differentiating Eq. 2.37 with respect to  $x$  and substituting  $A_y(x)$  with the expression from Eq. 2.37, we get a differential equation in magnetic field  $B(x)$  as

$$\frac{d^2B(x)}{dx^2} = \frac{1}{\lambda_L^2} \tanh^2\left(\frac{x}{\sqrt{2}\xi}\right) B(x) + \frac{2\sqrt{2}}{\xi} \operatorname{cosech}\left(\frac{\sqrt{2}x}{\xi}\right) \frac{dB(x)}{dx}. \quad (2.39)$$

The exact solution of Eq. 2.39 is too complicated for any algebraic manipulation and it was solved numerically for various values of parameters  $\xi$  and  $\lambda_L$  with the boundary conditions

$$\begin{aligned} B(x=0) &= B_o, \\ B(x=\infty) &= 0. \end{aligned} \quad (2.40)$$

Mathematically, we set  $B(x=20\lambda_L) = 0$  since at a depth of  $20\lambda_L$ ,  $B(x) = e^{-20}$  if field were purely exponential. In our case,  $B(x)$  becomes purely exponential at  $x \geq 2\sqrt{2}\xi$ .

A phenomenological function, that agrees well with numerical solutions, is found to be

$$\begin{aligned} B(x) &= B_o \left[ 1 + \left\{ \exp \left[ \frac{\sqrt{2}\xi \tanh\left(\frac{x}{\sqrt{2}\xi}\right)}{\lambda_L} \right] - 1 \right\} \tanh\left(\frac{x}{\sqrt{2}\xi}\right) \right] \\ &\times \exp \left[ -\frac{x \tanh\left(\frac{x}{\sqrt{2}\xi}\right)}{\lambda_L} \right]. \end{aligned} \quad (2.41)$$

The difference between numerical solution of Eq. 2.39 and its phenomenological fit is  $< 1\%$  of applied field suggesting a fairly close approximation to the actual solution.

Very close to the sample surface, i.e  $x \ll \xi$ ,

$$\begin{aligned} \tanh(x) &\approx x, \\ \exp[x] &\approx 1 + x, \end{aligned} \quad (2.42)$$

and Eq. 2.41 may be written as

$$B(x) = B_o \exp \left[ 1 + \frac{c^2 y^3}{2} - \left( \frac{c}{3} + \frac{c^2}{2} - \frac{c^3}{6} \right) y^4 + \dots \right], \quad (2.43)$$

where

$$\begin{aligned} c &\equiv \frac{\sqrt{2}\xi}{\lambda_L}, \\ y &\equiv \frac{x}{\sqrt{2}\xi}. \end{aligned} \quad (2.44)$$

The ratio of the second and third term in Eq. 2.43 is always less than 1 when

$$\frac{3c}{2y} < 1,$$

$$\begin{aligned} \Rightarrow \frac{2y}{3c} &> 1, \\ \Rightarrow x &> 3\frac{\xi^2}{\lambda_L}. \end{aligned} \quad (2.45)$$

For a specific case of  $\xi = 100\text{\AA}$  and  $\lambda_L = 1500\text{\AA}$ , the Eq. 2.45 yields  $x > 20\text{\AA}$ . So, the phenomenological function increases slightly ( $\ll 1\%$ ) within range  $0 < x < 3\frac{\xi^2}{\lambda_L}$  but drops gradually as expected from the numerical solution. Alternatively, for large  $x$

$$\tanh\left(\frac{x}{\sqrt{2}\xi}\right) \approx 1 \quad (2.46)$$

and  $B(x)$  may be written as

$$B(x) = B_o [1 + \Delta] \exp\left[-\frac{x}{\lambda_L}\right], \quad (2.47)$$

where

$$\Delta = \exp\left[\frac{\sqrt{2}\xi}{\lambda_L}\right] - 1. \quad (2.48)$$

Thus,  $B(x)$  is an exponentially decaying function but with a higher amplitude than  $B_o$  if extrapolated to  $x = 0$ . This is reasonable since at  $x \geq 2\sqrt{2}\xi$ , order parameter reaches its bulk value and exponential decay of field starts from there and very close to surface,  $B(x)$  varies slowly i.e, almost flat.

One such numerical solution along with its phenomenological fit is shown in figure 2.2. As we observe from Eq. 2.41, the order parameter  $\phi(r)$  attains it's bulk value inside a superconductor on the distance of the order  $\xi$ .

With the constant order parameter, given in Eq. 2.32, the Eq. 2.36 yields

$$\begin{aligned} \frac{d^2 A_y(x)}{dx^2} &= \frac{1}{\lambda_L^2} A_y(x), \\ \Rightarrow \frac{d^2 B(x)}{dx^2} &= \frac{1}{\lambda_L^2} B(x), \end{aligned} \quad (2.49)$$

since,

$$\frac{dA_y(x)}{dx} = B(x). \quad (2.50)$$

With the boundary condition (Eq. 2.40), the Eq. 2.49 has the solution

$$B(x) = B_o e^{-\frac{x}{\lambda_L}} \quad (2.51)$$

Both magnetic field expressions in Eqs. 2.41 and 2.51 will be used to extract  $\xi$  and  $\lambda_L$ .

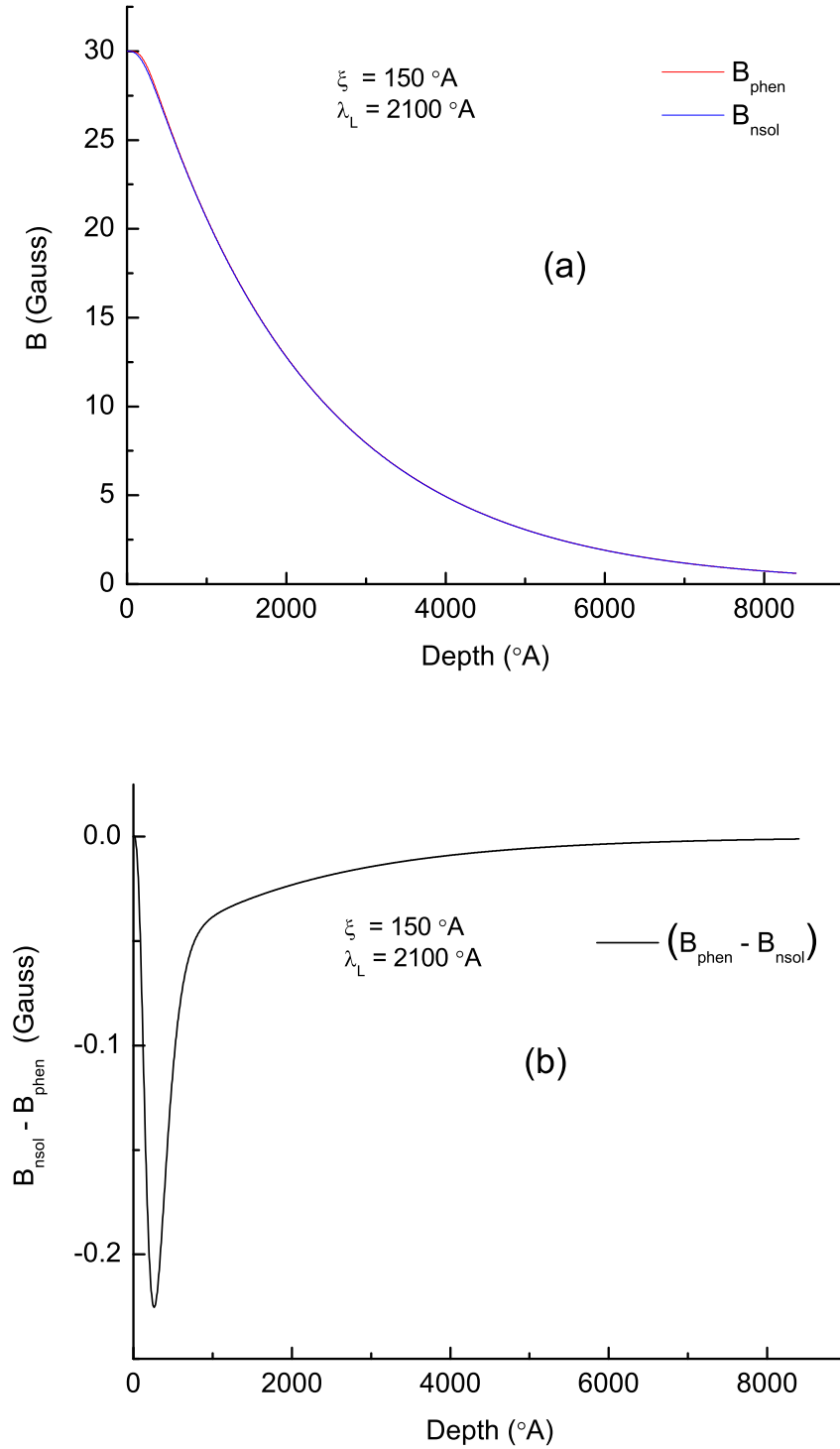


Figure 2.2: (a) Numerical solution ( $B_{\text{nsol}}$ ) and its phenomenological fit ( $B_{\text{phen}}$  as given in Eq. 2.41) of the magnetic field in G-L theory. (b) Difference between them.  $\xi = 150 \text{ \AA}$  and  $\lambda_L = 2100 \text{ \AA}$  in both figures.

## 2.4 BCS penetration depth

The basic idea for BCS superconductivity is that an attractive interaction between electrons, regardless of their strength, can bind the electrons into pairs [6]. We consider a case for only two electrons added to the Fermi sea. The first electron attracts positive ions and these ions, in turn, attract the second electron giving rise to an effective attractive interaction between electrons. Due to the movement of ion cores, phonon waves are generated and the interaction between electrons is thereby phonon mediated. The total energy of the electron system is minimized when there are Cooper pairs compared to a Fermi gas with no correlation. The center of mass of a Cooper pair is zero since the electrons tend to have opposite momenta and spin  $|\hbar\vec{k}, \uparrow\rangle$  and  $|-\hbar\vec{k}, \downarrow\rangle$ . Due to this opposite momenta and spin, it is labeled *s*-wave pairing since the relative angular momenta of the two electrons is zero. Although NbSe<sub>2</sub> is thought to be a conventional *s*-wave superconductor, recent works suggest that an other form of pairing involving non-zero angular momenta (eg. *d*-wave with  $L = 2, S = 0$ ) may be involved in the superconductivity other materials such as YBa<sub>2</sub>Cu<sub>3</sub>O<sub>7</sub>. However, the macroscopic phenomenology of the resulting superconducting state, treated earlier by Ginzburg-Landau equations, is basically the same.

One important consequence of the BCS theory is that the presence of a momentum dependent energy gap  $\Delta_k$  at the Fermi surface so that an amount of  $2\Delta_k$  energy is required to break a Cooper pair. The energy gap is schematically shown in Figure 2.3. The gap is opened at the Fermi energy as the temperature is lowered below the critical temperature.

In the weak coupling limit, where the gap  $\Delta$  is much smaller than the characteristic phonon energy  $\hbar\omega_D$ ,

$$\frac{2\Delta(0)}{k_B T_c} = 3.52. \quad (2.52)$$

The numerical factor 3.52 is well tested in experiments and found to be reasonable, in purely BCS type interactions. It is interesting to note that in NbSe<sub>2</sub>, it has been suggested that the upper energy band behaves largely like BCS<sup>1</sup> but the smaller energy gap follows non-BCS behavior [22].  $\Delta(T)$  remains fairly constant until the phonon energy becomes enough to thermally excite the quasiparticles. Near the transition temperature  $T_c$ ,  $\Delta(T)$  varies as

$$\frac{\Delta(T)}{\Delta(0)} \sim 1.74 \left(1 - \frac{T}{T_c}\right)^{\frac{1}{2}}, \quad T \sim T_c \quad (2.53)$$

<sup>1</sup>The constant factor in Eq. 2.52 being  $\approx 3.9$

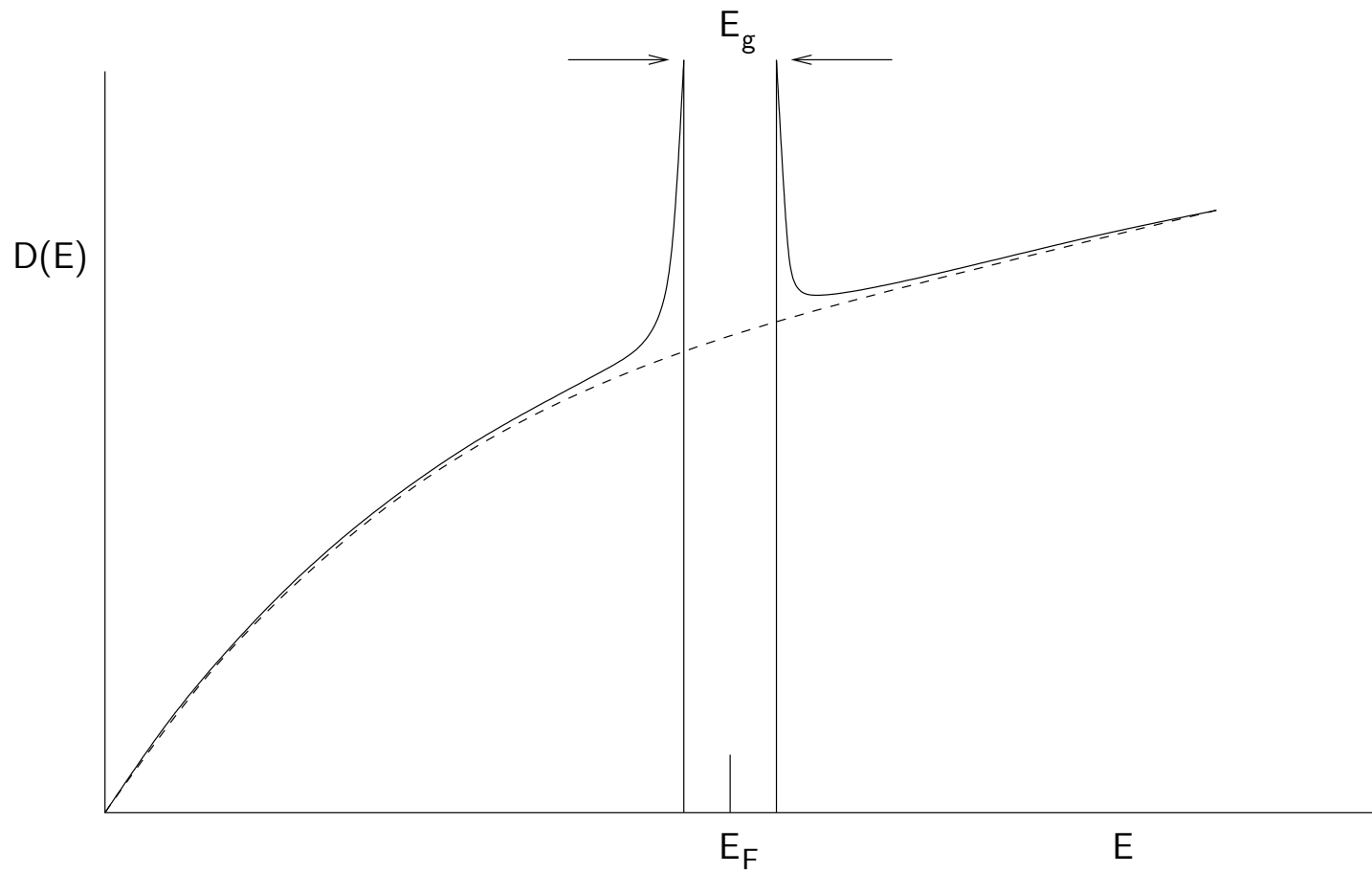


Figure 2.3: Typical density of states in a superconductor. The dashed line represents the normal state while the solid line represents the superconducting state.

and is graphically shown in Fig 2.4.

Finally, we mention that the electronic properties of NbSe<sub>2</sub> are anisotropic. This is largely due to the layered structure of the material. The degree of anisotropy is expressed in terms of a anisotropy parameter given by

$$\gamma = \left( \frac{m_c^*}{m_{ab}^*} \right) = \frac{\lambda_c}{\lambda_{ab}} = \frac{\xi_{ab}}{\xi_c} = \frac{H_{c2}^{\parallel ab}}{H_{c2}^{\parallel c}}, \quad (2.54)$$

where  $\parallel ab(\parallel c)$  indicates the field  $H$  perpendicular(parallel) to the  $c$ -axis of the sample and  $m^*$ ,  $\lambda$ ,  $\xi$  and  $H_{c2}$  are GL effective mass, penetration depth, coherence length and upper critical field, respectively.

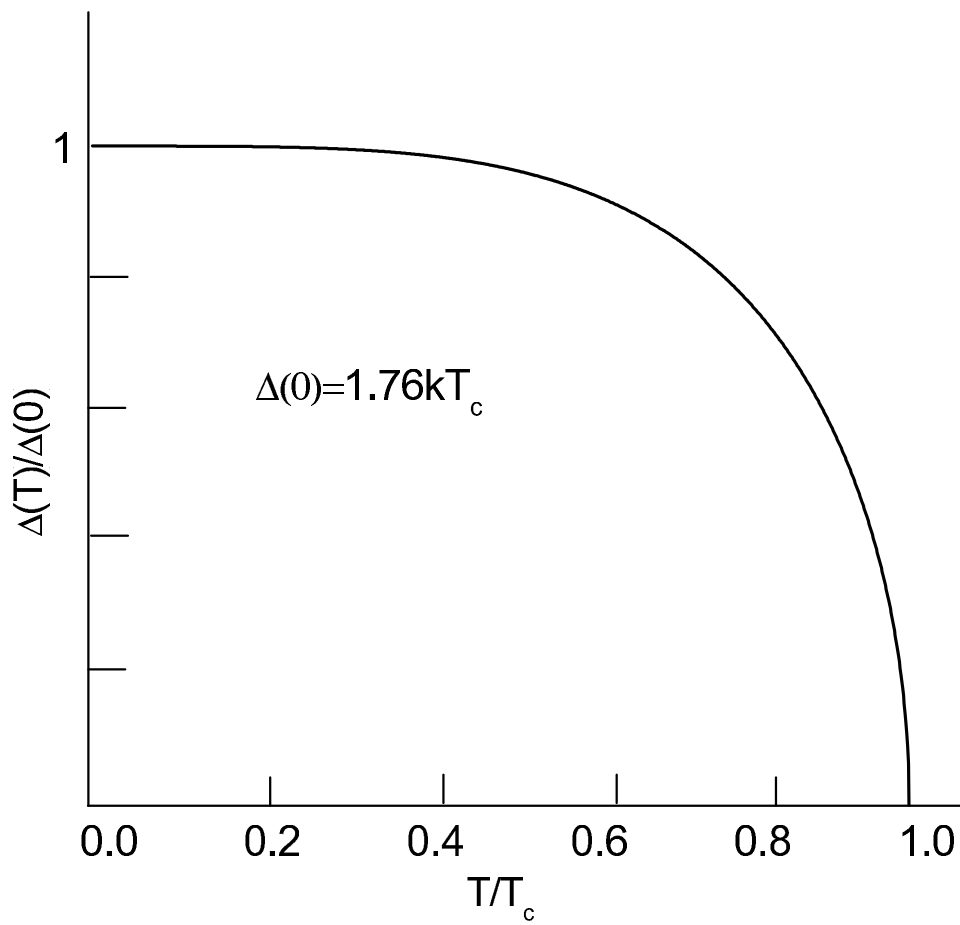


Figure 2.4: Temperature dependence of the superconducting energy gap in the weak coupling limit of BCS interaction.

## Chapter 3

# Time Dependence of Polarization and Relaxation

In this chapter, I shall discuss three important processes that lead to time dependence of the nuclear polarization.

- Coherent transfer of polarization between  $^8\text{Li}$  and Nb nuclei, through the magnetic dipolar interaction, but no relaxation of  $^8\text{Li}$ .
- Korringa relaxation mechanism at high magnetic field due to scattering of conduction electrons off the nuclear spin.
- Low field relaxation from fluctuating nuclear dipolar interaction between the  $^8\text{Li}$  and, the host, Nb nuclear spins.

### 3.1 Evolution of $^8\text{Li}$ Spin Polarization in $\text{NbSe}_2$ in the Absence of Relaxation

For simplicity, we consider the time evolution of spin polarization in a situation where the  $^8\text{Li}$  is coupled to a single Nb spin through the magnetic dipolar interaction.  $^8\text{Li}$  nucleus interacts with a few host Nb nuclei. However, interaction of one pair (involving one  $^8\text{Li}$  and one Nb nuclei) is almost independent of the interaction of other pairs and it will be sufficient to discuss one pair only. The applied magnetic field direction is defined to be  $\hat{z}$  direction. Only that component of spin polarization is of interest since that is the observed quantity.

The evolution of  $^8\text{Li}$  polarization, in the  $\hat{z}$  direction, is given by

$$\begin{aligned} P_z(t) = \langle I_z \rangle &= \text{Tr}\{\rho \cdot I_z\} \\ &= \text{Tr}\left(I_z e^{-i\mathcal{H}t/\hbar} \rho_0 I_z e^{i\mathcal{H}t/\hbar}\right), \end{aligned} \quad (3.1)$$

where  $\rho$  is the density operator (with  $\rho_0$  being its initial value) of the system and  $I_z$  is the  $z$ -component of the  $^8\text{Li}$  spin operator and  $\mathcal{H}$  is the spin

Hamiltonian. Considering the case where we ignore  $S$  spin dynamics and any diffusion of  ${}^8\text{Li}$ , at 10K and below, the effective Hamiltonian may be written as

$$\mathcal{H} = \mathcal{H}_I + \mathcal{H}_S + \mathcal{H}_{IS}, \quad (3.2)$$

where  $I$  and  $S$  are  ${}^8\text{Li}$  and host (Nb) spins respectively.  $\mathcal{H}_I$  and  $\mathcal{H}_S$  are the Zeeman plus quadrupolar parts of Hamiltonian and  $\mathcal{H}_{IS}$  is the dipolar interaction between  $I$  and  $S$ . For simplicity, we treat  ${}^8\text{Li}$  to be of pseudo spin- $\frac{1}{2}$  nuclei and thereby having no quadrupolar interaction. The gyromagnetic ratio of this pseudo-spin  $\frac{1}{2}$  particle would still be that of  ${}^8\text{Li}$ . Nb would be treated with its real spin  $\frac{9}{2}$ . The Hamiltonian may be written as, in frequency units,

$$\frac{\mathcal{H}}{\hbar} = -\gamma_{\text{Li}} I_z B - \gamma_n J_z B + \nu_q J_z^2 + \beta \mathcal{H}_{IS}, \quad (3.3)$$

where  $\gamma_{\text{Li}} = 6.3\text{MHz/T}$  and  $\gamma_n = 10\text{MHz/T}$  are gyromagnetic ratios respectively and  $\nu_q = 1.325\text{MHz}$  [28] is the quadrupolar frequency of Nb,  $\beta$  is the strength of dipolar interaction. For simulation of polarization,  $\beta$  was chosen to be 0.49 kHz since that is a rough estimate of the dipolar interaction strength (see chapter 5).  $\mathcal{H}_{IS}$  is the classical dipolar Hamiltonian and can be written as [29],

$$\mathcal{H}_{IS} = A + B + C + D + E + F, \quad (3.4)$$

where,

$$\begin{aligned} A &= I_z J_z (1 - 3\cos^2\theta), \\ B &= -\frac{1}{4} (I^+ J^- + I^- J^+) (1 - 3\cos^2\theta), \\ C &= -\frac{3}{2} (I^+ J_z + I_z J^+) \sin\theta \cos\theta e^{-i\phi}, \\ D &= -\frac{3}{2} (I^- J_z + I_z J^-) \sin\theta \cos\theta e^{i\phi}, \\ E &= -\frac{3}{4} (I^+ J^+) \sin^2\theta e^{-2i\phi}, \\ F &= -\frac{3}{4} (I^- J^-) \sin^2\theta e^{2i\phi}, \end{aligned} \quad (3.5)$$

with  $I^+$  and  $I^-$  being spin raising and spin lowering operators, respectively, for  ${}^8\text{Li}$  while  $J^+$  and  $J^-$  are spin raising and spin lowering operator, respectively, for Nb,  $\theta$  and  $\phi$  are the polar and azimuthal angle for the angle between the vector connecting  ${}^8\text{Li}$  and Nb nuclei and applied field

direction. The effect of raising and lower operators on eigenstates are given by the relationships

$$\begin{aligned} J^+|j, m\rangle &= \hbar\sqrt{j(j+1)-m(m+1)}|j, m+1\rangle, \\ J^-|j, m\rangle &= \hbar\sqrt{j(j+1)+m(m-1)}|j, m-1\rangle, \end{aligned} \quad (3.6)$$

where  $j$  is the spin quantum number for operator  $J$ .

Polarization  $P_z(t)$  from equation 3.1 may be written for a spin- $\frac{1}{2}$  probe as [30]

$$\begin{aligned} P_z(t) &= \frac{P}{N} \sum_{m,n} |\langle m|\sigma_z|n\rangle|^2 \exp(i\omega_{mn}t) \\ &= \frac{P}{N} \sum_{m,n} \{|\langle m|\sigma_z|n\rangle|^2 + 2 \sum_{n<m} |\langle m|\sigma_z|n\rangle|^2 \cos(\omega_{nm}t)\} \end{aligned} \quad (3.7)$$

where  $P$  is the total polarization at  $t = 0$  and  $N$  is the number of states available,  $|m\rangle, |n\rangle$  are the eigenkets of  $\mathcal{H}$  with energies  $\hbar\omega_m, \hbar\omega_n$ .

By averaging Eq. 3.7 over Lithium lifetime as,

$$\overline{P_z(B)} = \frac{1}{\tau} \int_0^\infty P_z(t) e^{-\frac{t}{\tau}} dt, \quad (3.8)$$

where  $\tau = 1.2\text{s}$  is the  $^8\text{Li}$  lifetime, we may get polarization along  $z$  direction  $P_z(B)$  which varies with magnetic field, as the resonance frequencies  $\omega_{mn}$  vary according to magnetic field.  $P_z(B)$  for equation 3.7 is shown in Fig 3.1 and in Fig 3.2. Note that the polarization at zero magnetic field is almost zero as the energy levels of  $^8\text{Li}$  and that of Nb are degenerate and flip-flop process in spin states can go on without any energy expense. The polarization is near 1 except near the magnetic fields where the Zeeman and quadrupolar interaction energies of  $^8\text{Li}$  and Nb match. Also, it may be noted from Fig 3.2 that the polarization takes nearly its full value over a range of 0-20G. The range scales with the dipolar interaction strength  $\beta$ .

Although we have considered an interaction of a spin- $\frac{1}{2}$  nucleus with Nb, a density matrix, with  $^8\text{Li}$  spin being 2, will cause changes in the amplitudes but not in the frequencies (see Ref.[31] and references therein). In particular, the ratio between time dependent and time independent parts of polarization will depend on the initial density matrix.

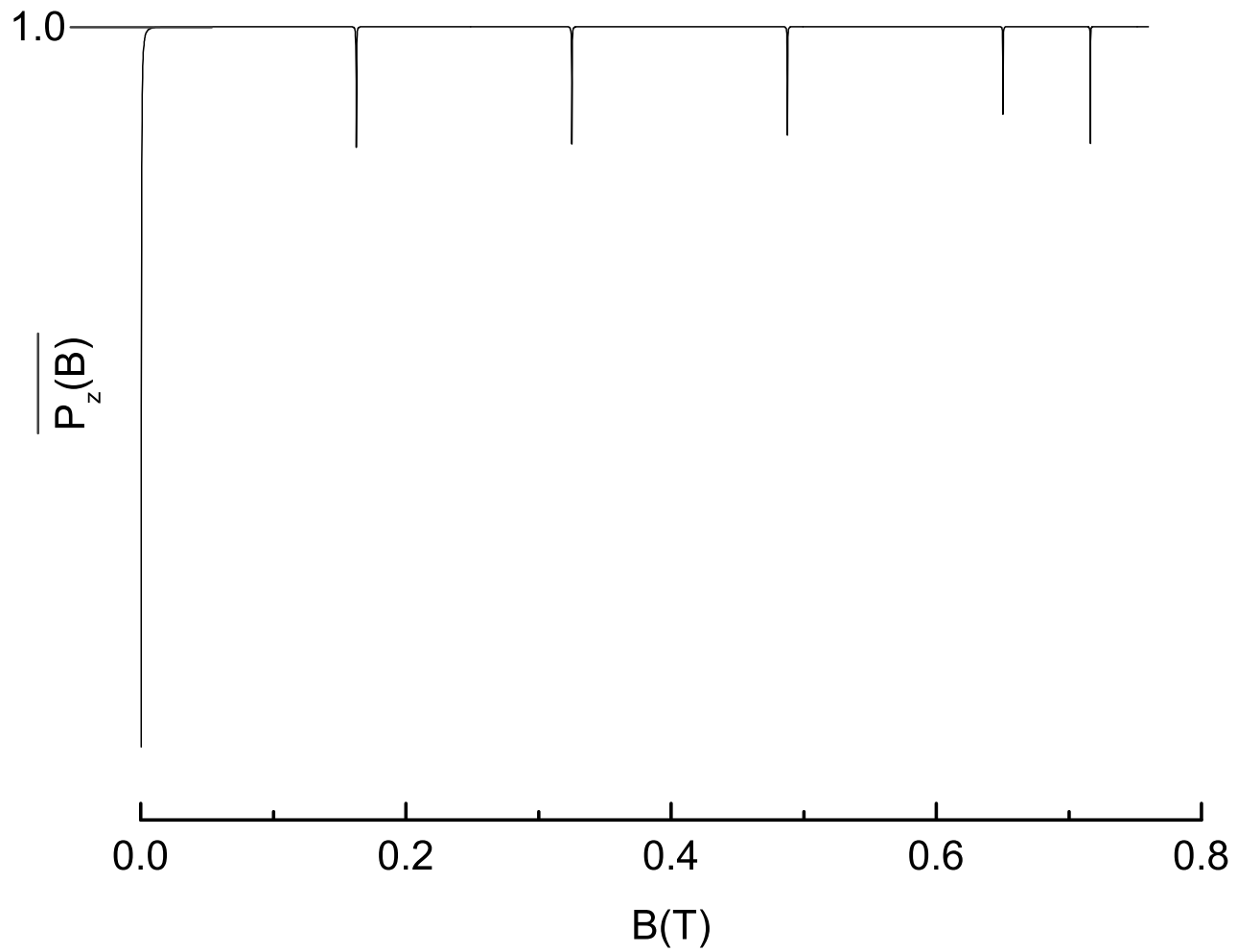


Figure 3.1: Time integrated polarization, as a function of magnetic field, showing resonant dips at level crossings with a single neighboring Nb.

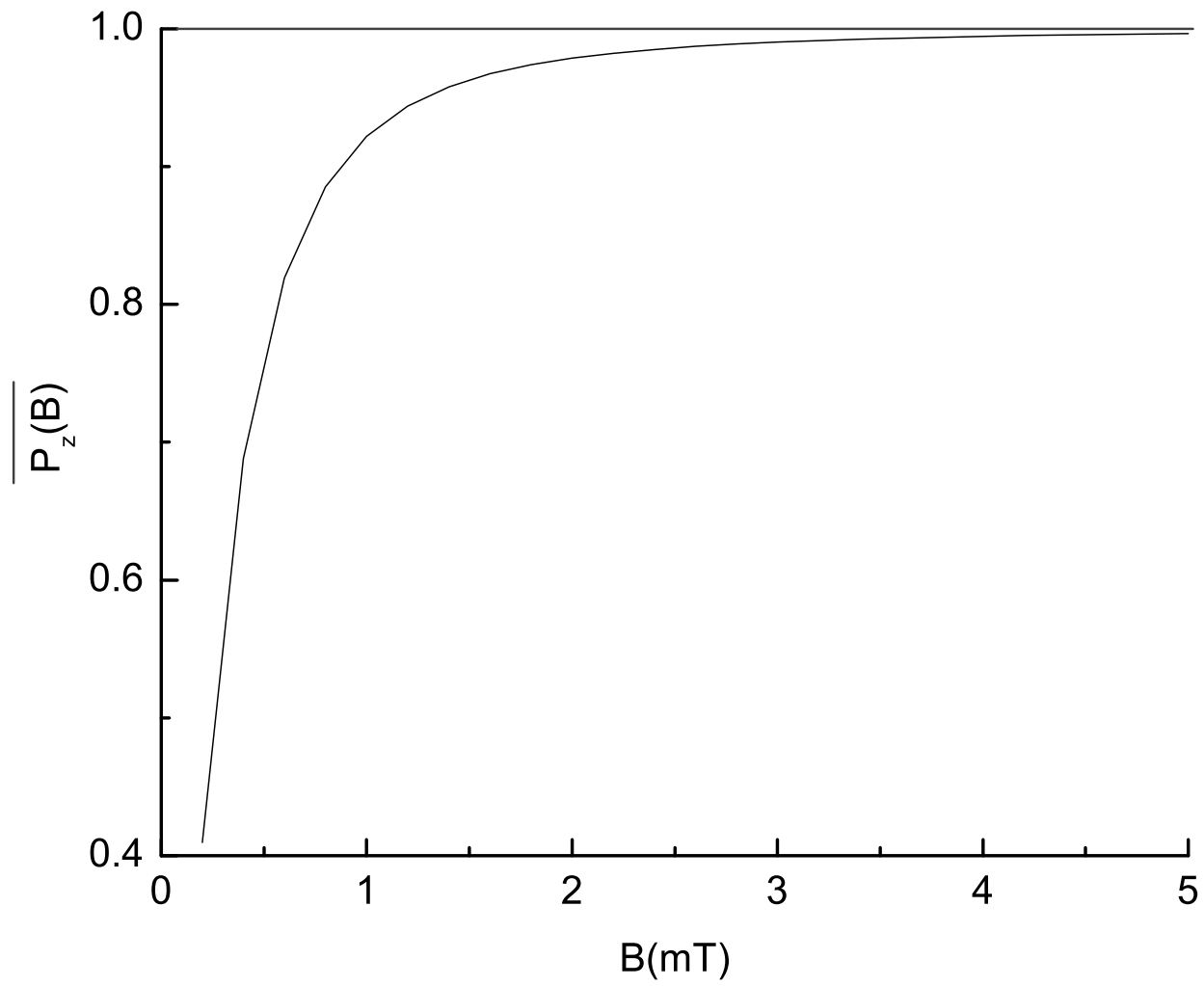


Figure 3.2: Time integrated polarization in low magnetic fields.

### 3.2 Korringa Relaxation & Knight Shift

In metals, there is a magnetic coupling between nuclear spins and the conduction electrons. If the nuclear and electronic moments are far apart, their magnetic interaction is given by the dipole interaction,

$$\mathcal{H}_d = \frac{\vec{\mu}_e \cdot \vec{\mu}_n}{r^3} - \frac{3(\vec{\mu}_e \cdot \vec{r})(\vec{\mu}_n \cdot \vec{r})}{r^5}, \quad (3.9)$$

where  $\vec{r}$  is radius vector from nucleus to electron and  $\vec{\mu}_n$  and  $\vec{\mu}_e$  are nuclear and electronic moments respectively. There is also a Fermi contact interaction between electron and nucleus given by

$$\mathcal{H}_{hf} = -\frac{8\pi}{3}\gamma_n\gamma_e\delta(\vec{r})\vec{I} \cdot \vec{S}, \quad (3.10)$$

which depends on the electron density at the site of the nucleus. Generally, this is much larger than the dipolar interaction.

As the conduction electrons move through the crystal, a specific nucleus experiences a magnetic coupling with many electrons and an effective interaction is found by averaging the expression in equation 3.10. In the absence of an external field, there is no preferential direction for electron moments and thereby zero average coupling with the nucleus. In contrast, application of magnetic field polarizes the electrons slightly, giving a small but finite average hyperfine field, through  $s$ -state wave function coupling to the nuclei. Since the  $s$ -state interaction leads to the nucleus experiencing a magnetic field parallel to the electron spin polarization direction, the effective field at the nucleus is increased. This translates into an increase of the resonance frequency in a metal, compared to non-metallic insulators and is given by

$$\omega_m = \omega_o + \Delta\omega \equiv \gamma(H_o + \Delta H), \quad (3.11)$$

where  $\omega_m$  is the observed Zeeman frequency in metal,  $\omega_o$  is the corresponding frequency in a non-metallic compound,  $H_o$  is the applied field and  $\Delta H$  is the increase in magnetic field at the nucleus due to its interaction with polarized conduction electrons.  $\frac{\Delta H}{H}$  is the fractional change in the resonance frequency and is called the Knight shift.

In a resonance measurement,  $^8\text{Li}$  is inserted into a sample and a radiofrequency(RF) magnetic field is applied perpendicular to the applied static field  $H_o$ . As  $H_o$  is stepped through different values, the  $^8\text{Li}$  polarization is unaffected unless the RF frequency is close to  $\omega_m$  causing a loss of polarization of  $^8\text{Li}$ . On or near resonances, the  $^8\text{Li}$  spin polarization will precess about

an effective field which is counted with respect to the applied field. Since, electrons are ejected preferentially in the direction of  ${}^8\text{Li}$  spin, a dip (i.e resonance) in the beta decay asymmetry is observed at  $\omega_m$ .

The shift in the resonance frequency is proportional to the degree of electronic polarization which scales with the magnetic field. In a normal metal, where the Pauli spin susceptibility is  $T$ -independent, the fractional shift in frequency  $\frac{\Delta\omega}{\omega_0}$  is temperature independent.

We now discuss the magnetization for the nuclei ( ${}^8\text{Li}$ ) after they are inserted into the sample. Initially, the  ${}^8\text{Li}$  spins are highly polarized and thereby out of temperature equilibrium with the lattice. Eventually, they relax to a common temperature of the lattice. We consider the relaxation of a system of nuclear spins whose Hamiltonian  $\mathcal{H}$  has eigenvalues  $E_n$  with an occupation probability  $p_n$ . If a system of  $N$  identical spins ( ${}^8\text{Li}$  in our case) is in thermal equilibrium with the lattice (Nb) at temperature  $T$ , then the rate of  ${}^8\text{Li}$  making downward transitions in energy would be equal to the rate of  ${}^8\text{Li}$  making upward transitions. We also assume that the transitions between every pair of energy levels are in equilibrium, i.e,

$$p_m W_{mn} = p_n W_{nm}, \quad (3.12)$$

where  $W_{mn}$  the probability per second that the lattice induces a transition of the system from  $|m\rangle$  to  $|n\rangle$ . Put in another way, the frequencies of transition in either direction of equilibrium, between any two energy states, are equal. This is also known as the principle of detailed balance [32]. Under these conditions, the rate of change of temperature of the  ${}^8\text{Li}$  system may be written as [24]

$$\frac{d\beta}{dt} = \frac{\beta_L - \beta}{T_1}, \quad (3.13)$$

where

$$\frac{1}{T_1} = \frac{1}{2} \frac{\sum_{mn} W_{mn} (E_m - E_n)^2}{\sum_n E_n^2}, \quad (3.14)$$

with  $\beta_L = \frac{1}{kT_L}$ , the thermal equilibrium temperature assuming that the transitions occur in  ${}^8\text{Li}$  being thermal equilibrium with the lattice and  $\frac{1}{T_1}$  is the relaxation rate of  ${}^8\text{Li}$  polarization. We also assume that transitions are rapid enough to guarantee thermal equilibrium and after each lattice transition, the nuclei readjust among their approximate energy levels so that the lattice is once again in thermal equilibrium.

For coupling to conduction electrons, the process may be viewed as being some electron with state  $|\mathbf{k}, s\rangle$  scattering off a  ${}^8\text{Li}$  nucleus, with energy state

$|m\rangle$ , to  $|\mathbf{k}', s'\rangle$  while the  ${}^8\text{Li}$  nuclei makes it's transition to state  $|n\rangle$ . The transition rate per second may be written as

$$W_{m\mathbf{k}s, n\mathbf{k}'s'} = \frac{2\pi}{\hbar} |\langle m\mathbf{k}s | V | n\mathbf{k}'s' \rangle|^2 \delta(E_m + E_{\mathbf{k}s} - E_n - E_{\mathbf{k}'s'}), \quad (3.15)$$

where the  ${}^8\text{Li-}e^-$  wavefunction is

$$|m\mathbf{k}s\rangle = |m\rangle|s\rangle u_{\mathbf{k}}(\mathbf{r}) e^{i\mathbf{k}\cdot\mathbf{r}}, \quad (3.16)$$

and  $V$  is the interaction potential given by equation 3.10. The delta function in equation 3.15 makes sure that the total energy is conserved in the transition. The transition rate for  ${}^8\text{Li}$  may be found by summing over all the possible electron configurations,

$$W_{mn} = \sum_{\mathbf{k}, s; \mathbf{k}', s'} W_{m\mathbf{k}s, n\mathbf{k}'s'} p_{\mathbf{k}s} (1 - p_{\mathbf{k}'s'}), \quad (3.17)$$

with  $p_{\mathbf{k}s}$  being unity if  $\mathbf{k}s$  is occupied and zero otherwise. Writing the equation 3.17 in terms of energy and replacing  $p_{\mathbf{k}s}$  by the Fermi function,  $W_{mn}$  may be written as<sup>1</sup>

$$\begin{aligned} W_{mn} &= \frac{64}{9} \pi^3 \hbar^3 \gamma_e^2 \gamma_n^2 \sum_{\alpha} \langle m | I_{\alpha} | n \rangle \langle n | I_{\alpha} | m \rangle \\ &\times \int \langle |u_{\mathbf{k}}(0)|^2 \rangle_E \rho^2(E) f(E) [1 - f(E)] dE, \end{aligned} \quad (3.18)$$

where  $\gamma_e$  and  $\gamma_n$  are gyromagnetic ratios for electrons and  ${}^8\text{Li}$  nucleus, respectively,  $I_{\alpha}$ 's are the three spin components of  ${}^8\text{Li}$ ,  $\rho(E)$  is the density of states,  $\langle |u_{\mathbf{k}}(0)|^2 \rangle_E$  is the average density of electrons, with energy  $E$ , at the nuclei position and  $f(E)$  is the Fermi occupation probability where

$$f(E) = \frac{1}{e^{\frac{(E-E_F)}{kT}} + 1}. \quad (3.19)$$

The Fermi function  $f(E)$  and it's two derivatives  $1 - f(E)$  and  $f(E)[1 - f(E)]$  are shown in Fig 3.3. As  $f(E)[1 - f(E)]$  peaks up within a width of  $kT$  of Fermi energy  $E_F$ , it may be approximated as

$$f(E)[1 - f(E)] \sim kT \delta(E - E_F). \quad (3.20)$$

<sup>1</sup>For a detailed discussion, see C.P. Slichter, *Principles of Magnetic Resonance* (Springer-Verlag, New York, 1990), p 151-156.

By utilizing equation 3.20, the equation 3.14 may be written as

$$\frac{1}{T_1} = \frac{64}{9} \pi^3 \hbar^3 (\gamma_n \gamma_e)^2 \langle |u_k^2(0)| \rangle_{E_F}^2 \rho^2(E_F) kT. \quad (3.21)$$

It may be noted from the Eq. 3.21 that the Korringa relaxation rate is dependent on the electron density at the nuclear position and on the density of states available at the Fermi energy and on the lattice temperature. Since the energy exchange between the  $^8\text{Li}$  and conduction electron is very small compared to  $kT$ , most electrons can't take part in this interaction since they have no empty states nearby to make transition into. Thus, only electrons within  $k_B T$  of the Fermi surface take part in such process.

Note that the quantity  $\langle |u_k^2(0)| \rangle_{E_F}$  in Eq. 3.21 is also involved in the Knight shift,

$$\frac{\Delta H}{H_0} = \frac{8\pi}{3} \langle |u_k^2(0)| \rangle_{E_F} \chi_e^S, \quad (3.22)$$

where  $\chi_e^S$  is the total spin susceptibility of the electrons defined in terms of total  $z$ -magnetization of the electrons,  $\bar{\mu}_z$  via the equation,

$$\bar{\mu}_z = \chi_e^S H_0. \quad (3.23)$$

By using the equation 3.22 and the expression for a Fermi gas of noninteracting gas,

$$\chi_e^S = \frac{\gamma_e^2 \hbar^2}{2} \rho(E_F), \quad (3.24)$$

the Eq. 3.21 may written as,

$$TT_1 \left( \frac{\Delta H}{H_0} \right)^2 = \frac{\hbar}{4\pi k} \left( \frac{\gamma_e}{\gamma_n} \right)^2. \quad (3.25)$$

One can define a Korringa ratio as,

$$\mathcal{K} = \frac{K^2 T_1 T}{S} \quad (3.26)$$

where

$$S = \frac{\hbar}{4\pi k} \left( \frac{\gamma_e}{\gamma_n} \right)^2, \quad (3.27)$$

with  $K = \frac{\Delta H}{H_0}$  being the Knight shift. The Korringa ratio in Eq. 3.26 is close to 1 for a perfect metal.

Note that, the Korringa relaxation is the only dominant relaxation mechanism at high applied magnetic fields ( $H > 1T$ ). At low fields, dipolar interaction between host nuclei Nb and probe  $^8\text{Li}$  turns out to be far more important than the hyperfine interaction and is discussed in the next section.

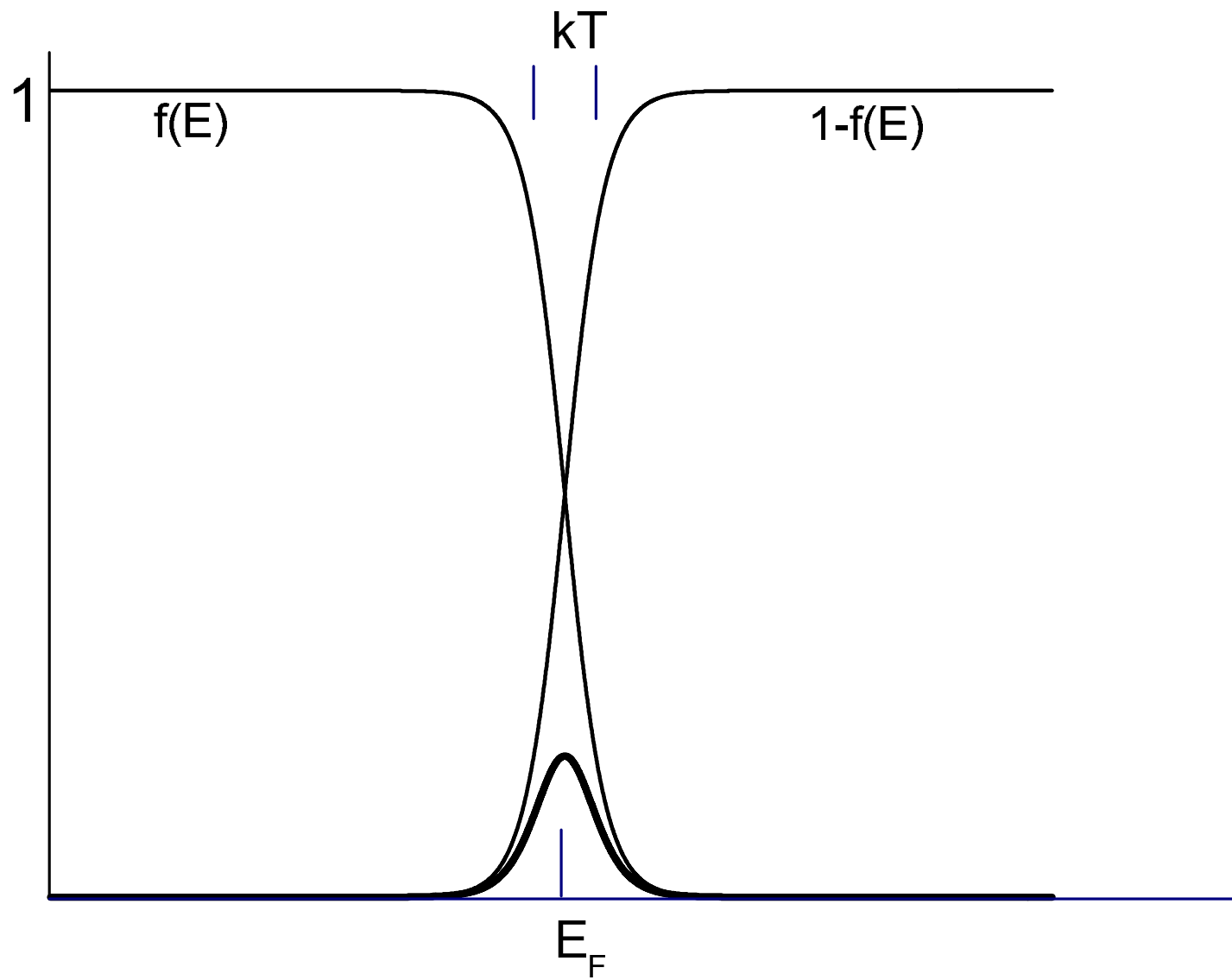


Figure 3.3: Functions  $f(E)$ ,  $1 - f(E)$ , and  $f(E)[1 - f(E)]$ . The thicker bell-shaped curve shows  $f(E)[1 - f(E)]$ .

### 3.3 Low Field Spin Relaxation from Fluctuating Dipolar Fields

At low fields, the interactions between  $^8\text{Li}$  and Nb are dipolar in nature. Random thermal fluctuations of Nb nuclei create random fluctuating effective field causing  $^8\text{Li}$  polarization to relax. For a randomly fluctuating dipolar field, we may assume an effective interaction Hamiltonian,

$$\mathcal{H}_1(t) = -\gamma_n \hbar \sum_{q=x,y,z} H_q(t) I_q. \quad (3.28)$$

We assume that the fields  $H_q$ 's take only two values  $\pm h_q$ , with an autocorrelation function [29],

$$\overline{H_q(t)H_{q'}(t+\tau)} = h_q^2 e^{-\frac{|\tau|}{\tau_o}}, \quad (3.29)$$

where  $\tau_o$  is the ‘‘correlation time’’ which roughly estimates the time for  $H_q(\tau)$  to jump from  $\pm h_q$  to  $\mp h_q$ . For simplicity, we assume  $^8\text{Li}$  to be a pseudo spin- $\frac{1}{2}$  system. For such a system, the relaxation rate  $\frac{1}{T_1}$  is given by

$$\frac{1}{T_1} = 2W_{\frac{1}{2},-\frac{1}{2}}. \quad (3.30)$$

In general, the transition rate  $W_{km}$  is given by [see appendix A for a detailed discussion]

$$W_{km} = \frac{J_{mk}(m-k)}{\hbar^2}, \quad (3.31)$$

where the spectral density  $J_{mk}(\omega)d\omega$  gives the interaction strength of  $\mathcal{H}_1(t)$  over a frequency range  $\omega + d\omega$ . A typical density  $J_{mk}(\omega)$  is shown in Fig 3.4.  $J_{mk}(\omega)$  has the Fourier transformation

$$J_{mk}(\omega) = \int_{-\infty}^{\infty} G_{mk}(\tau) e^{-i\omega\tau} d\tau, \quad (3.32)$$

where  $G_{mk}(\tau)$  is known as the ‘‘correlation function’’ of  $\mathcal{H}_1(t)$  and is given by [29]

$$G_{mk}(\tau) = \overline{\langle m | \mathcal{H}_1(t) | k \rangle \langle k | \mathcal{H}_1(t+\tau) | m \rangle} \quad (3.33)$$

$G_{mk}(\tau)$  gives us the functional dependence of  $\mathcal{H}_1(t)$  with  $\mathcal{H}_1(t+\tau)$ . For a randomly fluctuating field as given in Eq. 3.28,  $W_{mk}(\tau)$  in equation 3.31 may be written as

$$W_{km} = \frac{1}{\hbar^2} \sum_q j_{mk}^q(m-k). \quad (3.34)$$

Using equations 3.28 and 3.33, the equation 3.32 may be written as

$$j_{mk}^q(\omega) = \gamma_n^2 \hbar^2 |\langle m|I_q|k\rangle|^2 \int_{-\infty}^{\infty} \overline{H_q(t)H_q'(t+\tau)} e^{-i\omega\tau} d\tau. \quad (3.35)$$

Using the exponential correlation given in equation 3.29, one may obtain from equation 3.35,

$$j_{mk}^q(\omega) = \gamma_n^2 \hbar^2 |\langle m|I_q|k\rangle|^2 h_q^2 \frac{2\tau_o}{1 + \omega^2 \tau_o^2} \quad (3.36)$$

and transition rate  $W_{km}$  may be written as

$$W_{km} = \left[ \sum_q \gamma_n^2 h_q^2 |\langle m|I_q|k\rangle|^2 \right] \frac{2\tau_o}{1 + (m-k)^2 \tau_o^2}. \quad (3.37)$$

For a strong static field along  $\hat{z}$ , non-zero components in expectation values of  $\langle m|I_q|k\rangle$  are

$$\begin{aligned} |\langle m|I_q|k\rangle| &= \frac{1}{2}, \quad q = x, y \\ |\langle m|I_z|k\rangle| &= 0. \end{aligned} \quad (3.38)$$

Due to the randomness of fluctuating field, we assume that all the components of the field are equal, i.e,  $h_x = h_y = h_z = h_o$ , giving

$$h_i^2 = \frac{1}{3} h_o^2$$

Using equation 3.30, one may obtain,

$$\frac{1}{T_1} = 2\gamma_n^2 \frac{h_o^2}{3} \frac{\tau_o}{1 + \omega_o^2 \tau_o^2} \equiv \Delta^2 \frac{\tau_o}{1 + \omega_o^2 \tau_o^2}, \quad (3.39)$$

where  $\Delta \equiv \sqrt{\frac{2}{3}} \gamma_n h_o$  and  $\omega_o = m - k = \gamma H_o$  is the Larmor frequency at applied field  $H_o$ , for a spin- $\frac{1}{2}$  system. Equation 3.39 is an important relationship between  $\frac{1}{T_1}$  and applied field. The temperature dependence of  $\tau_o$  induces temperature dependence into relaxation rate. Equation 3.39 will be used to extract values of  $\Delta$  and  $\tau_o$  in a later chapter.

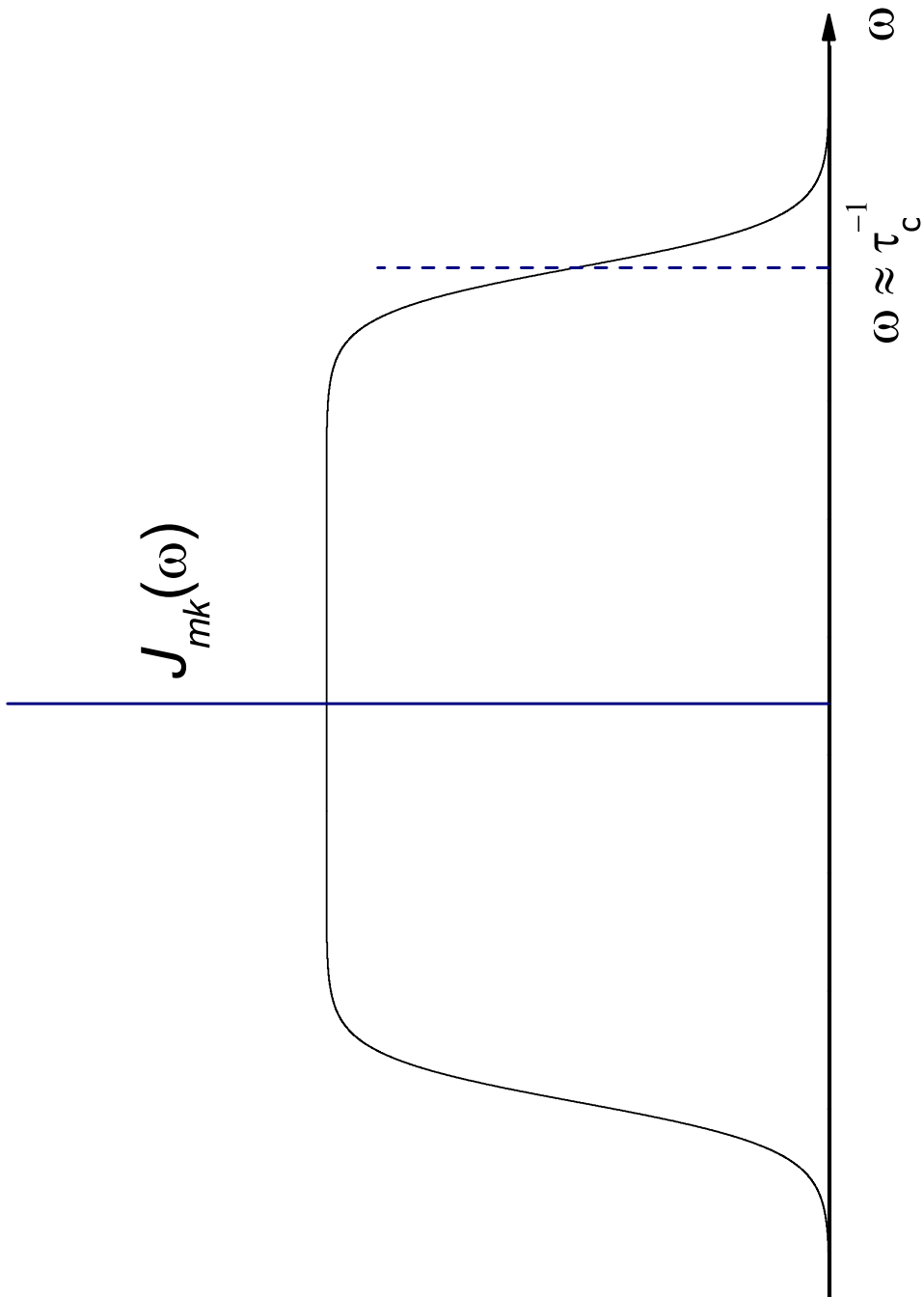


Figure 3.4: Typical spectral density plot.

## Chapter 4

# Experimental

### 4.1 Beamline Properties and Spectrometer

In our experiment, a beam of radioactive nuclei [33] is given a significant polarization and then implanted onto the sample. In low fields and low temperatures,  ${}^8\text{Li}$  loses its nuclear polarization primarily by exchanging energy with host nucleus Nb. Loss in polarization is detected via the  $\beta$ -decay



where  $e^-$  is emitted preferentially in the direction of  ${}^8\text{Li}$  spin at the time of its decay. The asymmetry (i.e directional dependence) in the decay of nuclear polarization contains information about the local electronic and magnetic environment of the sample.

The isotope separator and accelerator (ISAC) delivers a continuous beam low energy ( $\approx 28\text{KeV}$ )  ${}^8\text{Li}$  at a rate  $\approx 10^7/\text{s}$ .  ${}^8\text{Li}$  is a spin 2 nucleus with a mean lifetime  $\tau = 1.21\text{s}$ , a gyromagnetic ratio  ${}^8\gamma = 630.15\text{Hz/G}$  and a small electric quadrupole moment  $Q = +33 \text{ mB}$ . The unpolarized  ${}^8\text{Li}$  is polarized as it passes through the “optical pumping region”, shown in the figure 4.1. The ion beam is first neutralized as it passes through a Na vapor cell. During its passage through this region, the  ${}^8\text{Li}$  atoms are excited by a dye laser ( $\lambda \approx 671 \text{ nm}$ ) tuned to the D1 atomic transition  ${}^2S_{1/2} \rightarrow {}^2P_{1/2}$  of  ${}^8\text{Li}$ (Fig. 4.2), where the outer shell electron is excited from  $l = 0$  to  $l = 1$ . The ground state and its first excited state energies are further split by hyperfine interaction between electron orbital angular momentum ( $l = 0, 1$ ) with total angular momentum  $= (2 \pm \frac{1}{2}) = \frac{5}{2}, \frac{3}{2}$ . For circular polarized light with positive helicity  $\Delta m_F = +1$  for excitation whereas for spontaneous decay  $\Delta m_F = 0, \pm 1$ . After 10-20 cycles of absorption and spontaneous emission, a highly polarized state with  $F = \frac{5}{2}, m_F = \frac{3}{2}$  i.e, a well-defined nuclear spin state with spin 2 is obtained. The polarization may be obtained as high as 80% [34].

The polarized beam is then passed through the He vapor cell to knock off one electron and thereby reionizing a fraction of it, so that it can be guided electrostatically into one of the two experimental stations. The fraction of

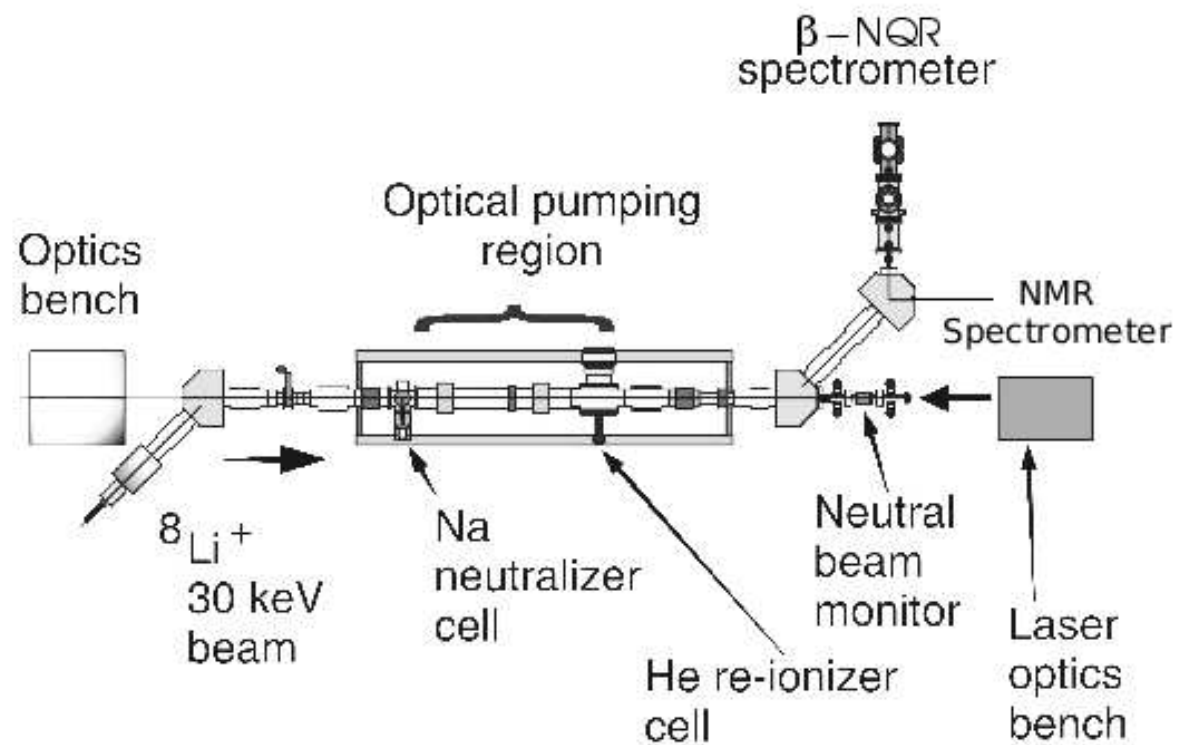


Figure 4.1: A schematic of the experimental layout. The 28 KeV  $^8\text{Li}^+$  ion beam is neutralized in the Na cell and then reionized in the He cell. In between, the beam is optically pumped with a laser tuned to the D1 optical transition of the  $^8\text{Li}$  atom. The resulting polarized beam is guided to  $\beta$ -NMR and  $\beta$ -NQR spectrometers.

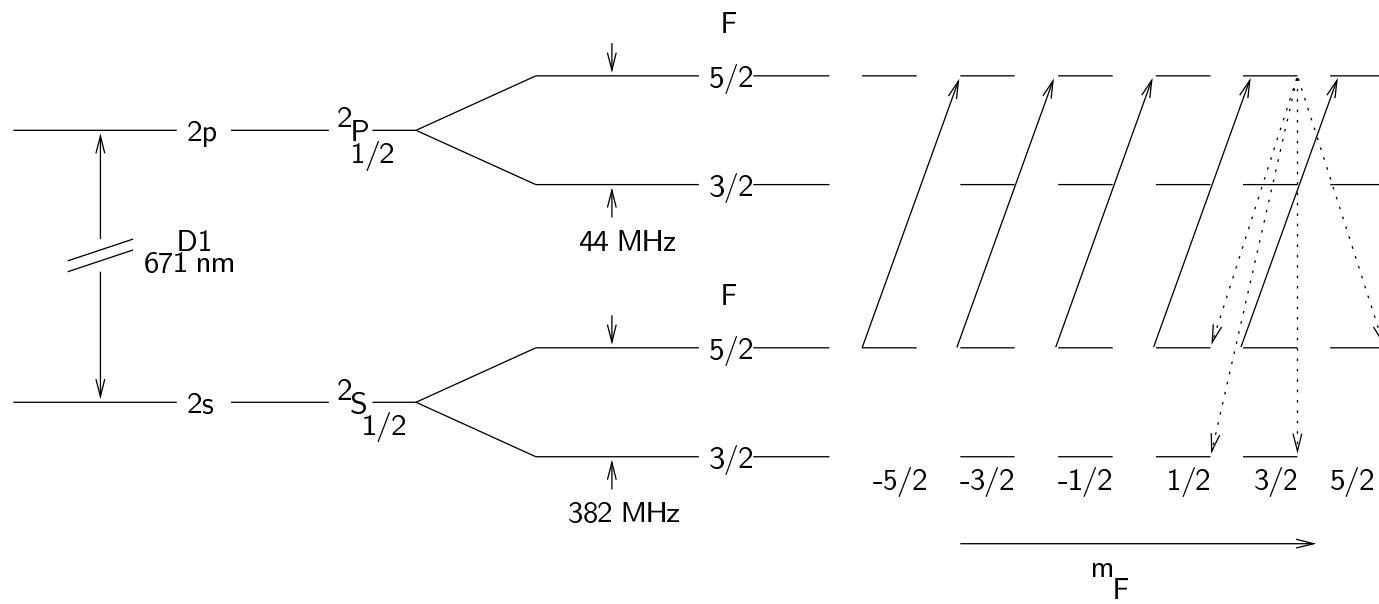


Figure 4.2: Optical Pumping scheme for polarizing  $^8\text{Li}$ .

the beam that does not get reionized by the He vapor cell, goes straight (i.e, not electrostatically bent) to the “neutral beam monitor”. The neutral beam provides an independent measurement of overall asymmetry, which remains constant for a steady  $^8\text{Li}$  ion beam. The polarization direction remains unchanged by these bends. Two of the stations, labeled as “low-field region” and “high-field spectrometer” in figure 4.1 are used for research in  $\beta$ -NQR and  $\beta$ -NMR, respectively. In both spectrometers, a small Helmholtz coil can be used to introduce either a CW or a pulsed RF magnetic field  $H_1$  that is perpendicular to static magnetic field  $H_0$ . The maximum value of  $H_0$  are 9T at high-field spectrometer and 20mT at the low-field spectrometer.

The time evolution of  $^8\text{Li}$  polarization is monitored using fast plastic scintillators placed forward and backward with respect to the initial spin direction. A typical frequency spectrum is shown in Fig 4.4

A schematic diagram of  $\beta$ -NQR spectrometer (where most of the data were taken) is shown in Figure 4.3. A coil in an approximate Helmholtz configuration is used to apply a small oscillating magnetic field perpendicular to static magnetic field. Electrons emitted from  $^8\text{Li}$  pass through thin stainless steel windows out of UHV chamber and reach detectors labeled as L and R. Detector telescopes consist of a pair of plastic scintillators with dimensions  $10\text{cm} \times 10\text{cm} \times 0.3\text{cm}$  and are located outside of UHV chamber. A set of three coils are utilized to apply a static magnetic field (0-20mT) along initial polarization direction or to zero at the field within 0.005mT.

The energy of the beam was set to be 28KeV corresponding to an average implantation depth of about  $2000\text{\AA}$ . However, it has been demonstrated that a beam energy as low as 100eV or less is achievable [35].

## 4.2 The sample

The crystal structure for  $\text{NbSe}_2$  is shown in Fig 4.5. The polytype is 2H- $\text{NbSe}_2$  where the integer 2 stands for the number of layers in a unit cell and hexagonal crystal symmetry [36] is indicated by H. The  $\text{NbSe}_2$  layers are weakly coupled by Van der Waals interaction whereas, within the layers, Nb and Se atoms are covalently bonded. Due to the weak coupling between the layers, it is easy to cleave the sample along a plane parallel to the layers. In our experiment, a freshly cleaved sample was used for measurements. It was exposed to air for only a short period of time ( $\approx 30$  minutes) before being loaded into the vacuum.

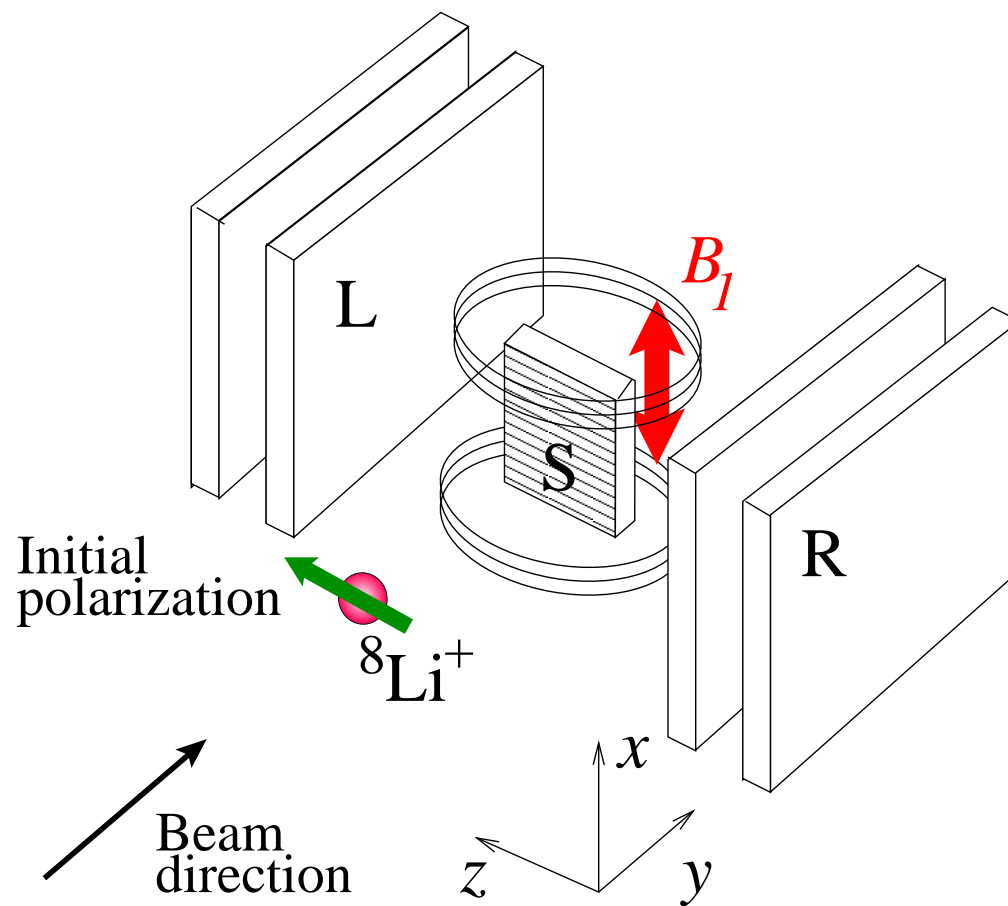


Figure 4.3: A schematic of the spectrometer for  $\beta$ -detected nuclear resonance. The spin polarization is perpendicular to the beam direction. The principal axis of the electric field gradient at the  ${}^8\text{Li}$  stopping site must have a component along  $\hat{z}$  in order for a signal to be detected at zero applied field.

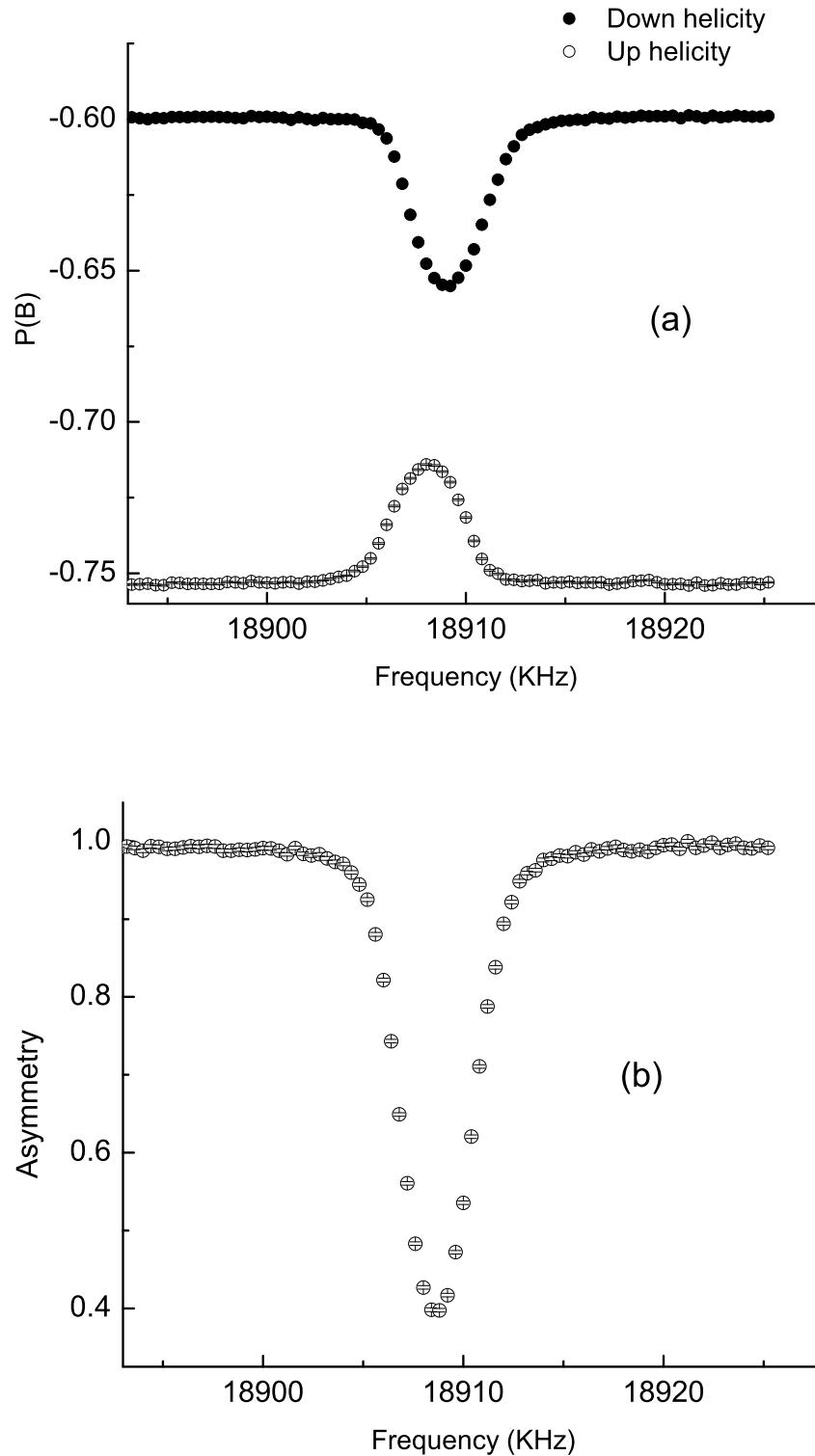


Figure 4.4: (a) Polarization  $P_z(B)$  for both helicities (b) Normalized asymmetry is found by subtracting “down” helicity from “up” helicity to remove the background effect.

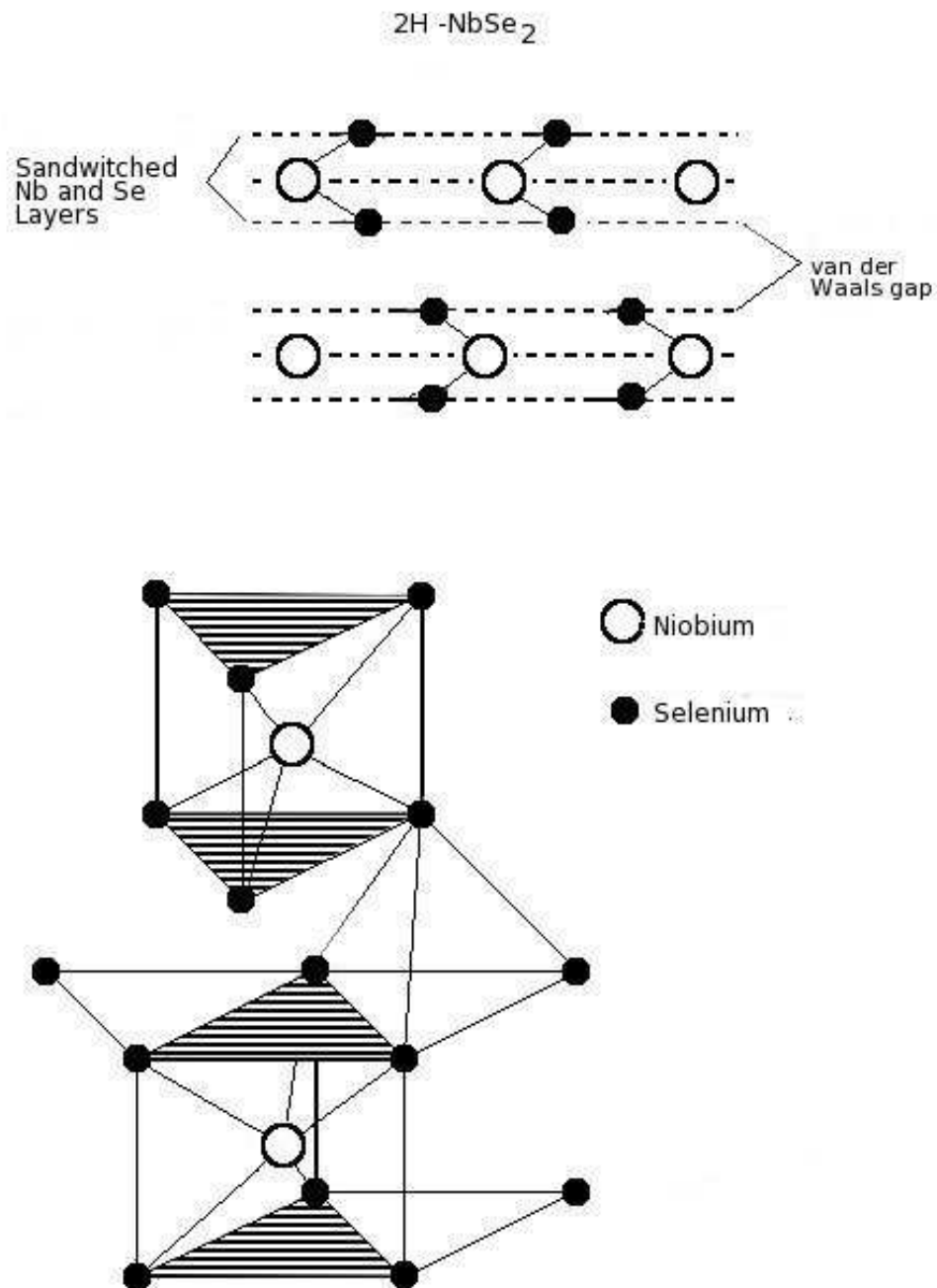


Figure 4.5: Top: NbSe<sub>2</sub> cross-section (in 11 $\bar{2}$ 0 plane). Bottom: Three dimensional structure of 2H-NbSe<sub>2</sub>.

### 4.3 Measurement of Polarization in Low Field

In this section, we discuss the results of measurements at low applied magnetic fields (15 G - 45 G) at T=8K. The same NbSe<sub>2</sub> sample was used to measure polarization decay. Methods for measuring  $P(t)$  are discussed briefly in the next two sections.

#### 4.3.1 P(t) in short pulse method

In this method, <sup>8</sup>Li beam was kept on for a shorter time period (0.5s) and the polarization  $p(t)$  was measured after beam goes off for about 10s. The functional dependence of  $p(t)$  is given by

$$p(t) = p_0 \exp\left[-\frac{t}{T_1}\right], \quad (4.2)$$

where  $T_1$  is the nuclear spin lattice relaxation time. From an experimental perspective, this method has the drawback that significant amount (> 90%) of beam time is lost and since the number of <sup>8</sup>Li is decreasing when the beam goes off the statistical errors gets larger as time goes on. The “long pulse” method was developed to improve the quality of data.

#### 4.3.2 P(t) in Long pulse method

In this method, the <sup>8</sup>Li beam was on for 4s and went off for 8s and the asymmetry was measured over this whole time range.

This method is advantageous since the spectra contains about eight times the number of decay events compared to the short pulse method. Thus it is better for measuring slow relaxation times. Furthermore, it is also better for measuring short relaxation times since one observes polarization back to earlier times. The only disadvantage is that the P(t) is convolved with the pulse shape.

Let  $R_0 dt'$  ( $R_0$  is the constant <sup>8</sup>Li incoming rate) be the number of <sup>8</sup>Li arriving in the sample at time interval  $(t', t' + dt')$  and surviving until time  $t$  is

$$N(t', t) = R_0 \exp\left[-\frac{t-t'}{\tau}\right] dt'. \quad (4.3)$$

The number of <sup>8</sup>Li that haven't decayed in the target at time  $t$  is given by:

$$\begin{aligned} N(t) &= R_0 \int_0^t \exp[-(t-t')/\tau] dt', \\ &= \tau R_0 [1 - \exp(-t/\tau)]. \end{aligned} \quad (4.4)$$

Similarly, the average polarization at time  $t$  is given by:

$$\begin{aligned} p(t) &= \frac{R_{\circ} p_{\circ} \int_0^t \exp[-(t-t')/\tau] \exp[-(t-t')/T_1] dt'}{N(t)}, \\ &= p_{\circ} \frac{\tau'}{\tau} \times \frac{1 - \exp[-t/\tau']}{1 - \exp[-t/\tau]}, \end{aligned} \quad (4.5)$$

where

$$\frac{1}{\tau'} = \frac{1}{\tau} + \frac{1}{T_1}. \quad (4.6)$$

Thus, the average polarization is time dependent for times on the scale of  $\tau'$ . The equation 4.5 is used throughout our calculation to fit the experimentally observed normal state polarization.

As one would expect, the polarization starts off at its maximum  $p_{\circ}$  and relaxes towards its equilibrium value of  $p_{\circ} \frac{\tau'}{\tau}$  on the time scale of  $\tau'$ . If the beam goes off, the polarization will relax from that value with a relaxation time  $T_1$ . Thus, in a  $T_1$ -measurement with a beam pulse width  $\Delta$ , we expect the following form:

$$\begin{aligned} p_{\text{pulse}}(t) &= p_{\text{step}}(t), \quad \text{for } 0 < t < \Delta, \\ &= p_{\text{step}}(\Delta) \exp\left[-\frac{(t-\Delta)}{T_1}\right], \quad \text{for } t > \Delta. \end{aligned} \quad (4.7)$$

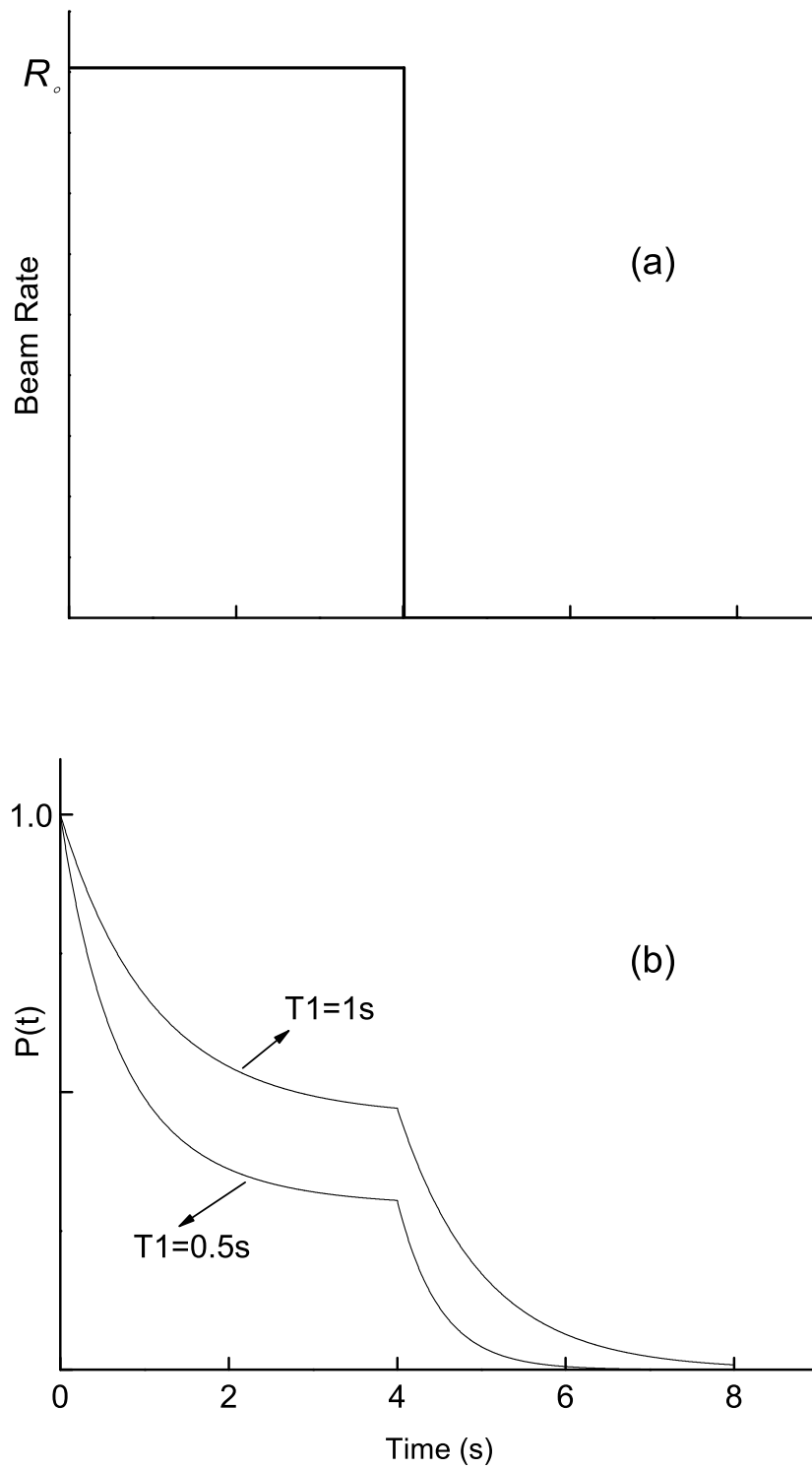


Figure 4.6: (a) Beam is on between time (0,4)s. (b) Schematic polarization  $P(t)$  as a function of time.

## Chapter 5

# Measurements and Results

### 5.1 Normal State in High Magnetic Field

#### 5.1.1 Korringa Relaxation

Due to its layered crystal structure, NbSe<sub>2</sub> shows an array of interesting properties. The atoms are metallicly and covalently bonded within a layer but experience only weak Van der Waals force between adjacent layers. This produces strong anisotropy in all the electronic and mechanical properties such as penetration depth, coherence length and effective mass of carriers.

Measurements of relaxation, in high field, were done using short pulses ( $\approx 0.5$ s) of <sup>8</sup>Li and polarization was measured as a function of time after the pulse. No RF field was present during the experiments. Fits to a single exponential were obtained as shown in Fig 5.1. The relaxation rate was observed to be a linear function of temperature as expected from Korringa relaxation. The anomalously small proportionality constant  $9(1) \times 10^{-5} \text{K}^{-1} \text{s}^{-1}$  (see Fig. 5.2) is 10 times smaller when compared to relaxation of <sup>8</sup>Li in Ag [37]. This suggests that <sup>8</sup>Li in NbSe<sub>2</sub> occupies a site in the Van der Waals gap where overlap with the conduction band is small. The extrapolated fit gives a non-zero relaxation rate at  $T = 0\text{K}$  which we attribute to residual effects from dipolar interaction, which dominates Korringa relaxation at low field but are highly suppressed at high field. As we may observe from Fig 5.2 that the lowest relaxation time measured is  $\sim 100$ s whereas the <sup>8</sup>Li lifetime is  $\approx 1.2$ s and thereby we are in the limit of our measuring capacity. This also contributes to the non-zero relaxation rates near 0K.

#### 5.1.2 Dipolar Broadening of the Resonance

Nuclear resonance was observed in an applied static field  $H_0$  via the detection of time averaged polarization as a function of applied frequency. The position and shape of spectra gives information about the local magnetic field and is attributed primarily to the nuclear dipolar interaction with Nb. Typical spectra are shown in Fig 5.3.

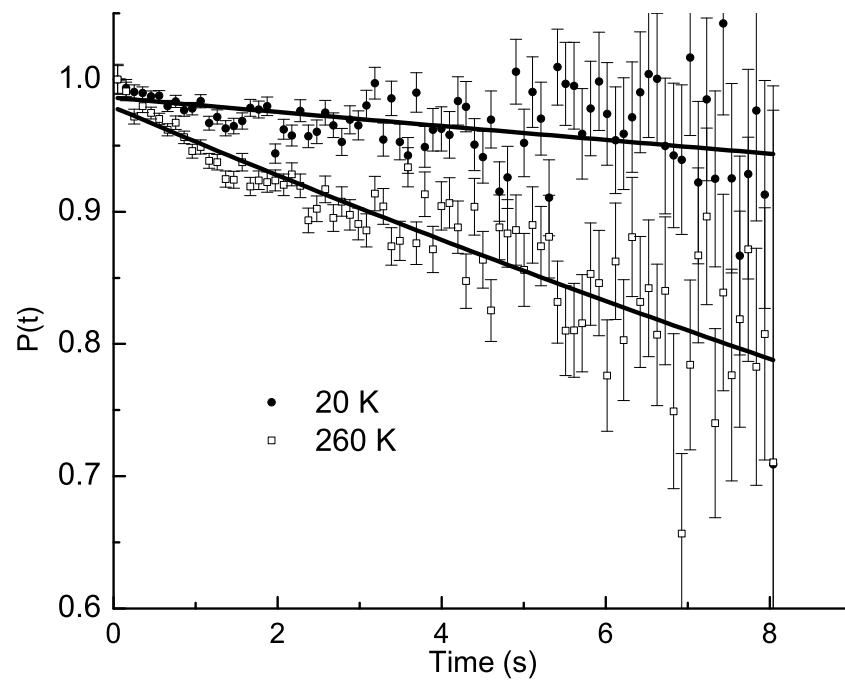


Figure 5.1: The time evolution of normalized spin polarization  $^8\text{Li}$  in  $\text{NbSe}_2$  in a magnetic field of 3T applied along the  $c$ -axis. The time differential measurements were done in short pulse mode. The solid lines are fits to a single exponential without any background.

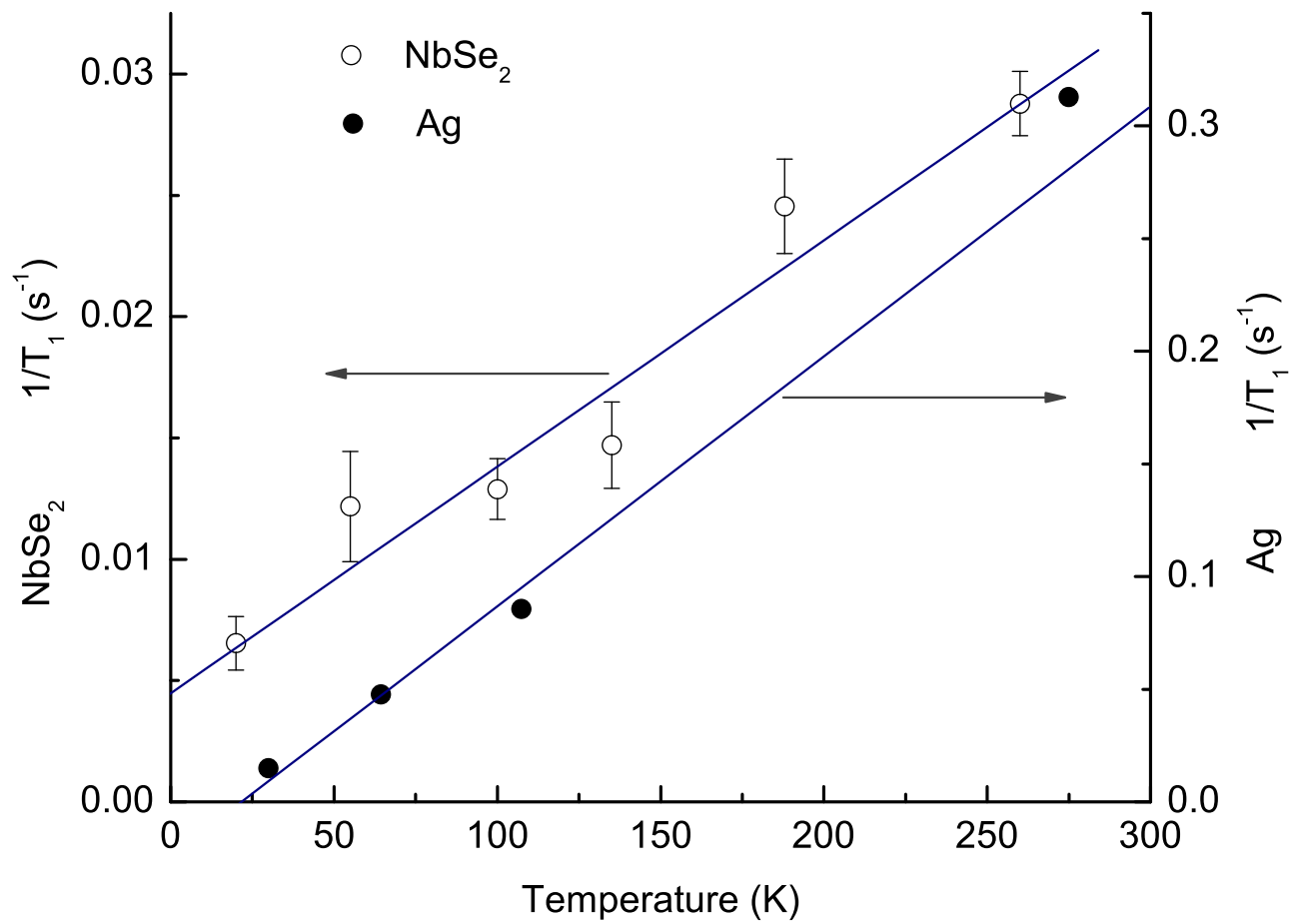


Figure 5.2: Comparison between spin relaxation of Li in Ag and NbSe<sub>2</sub> as a function of temperature. The applied field along c-axis is 3T.

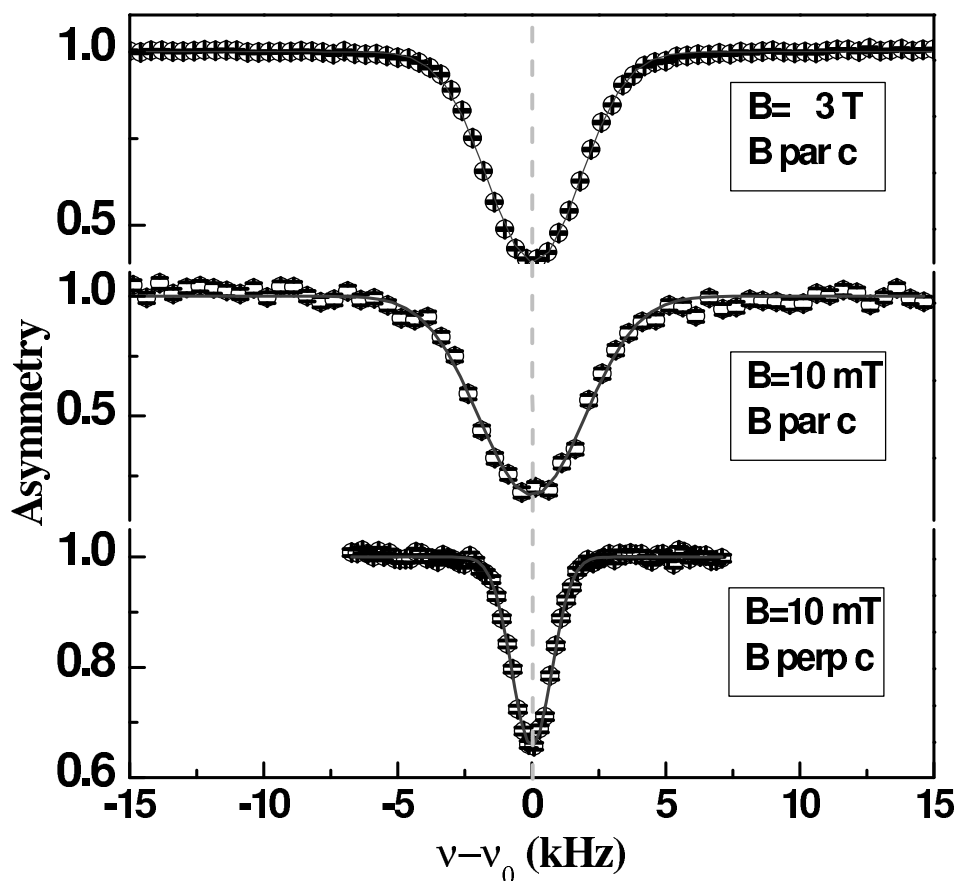


Figure 5.3: The  $\beta$ -NMR resonance in NbSe<sub>2</sub> as a function of field and orientation. The top two scans were taken with the field parallel to the c-axis but at very different fields; whereas, the bottom scan is with the field perpendicular to the c-axis. The temperature is 10K in all cases and so there is no line broadening due to <sup>8</sup>Li motion.

Gaussian fits of the spectra indicate a FWHM (Full Width at Half Maxima), i.e, the dipolar width to be  $\sim 2.4\text{kHz}$ , in case of  $B \perp c$ . The width is very weakly dependent on the radio frequency (RF) power level which indicates that the measured linewidth is close to the intrinsic width. The linewidth also indicates the strength of dipolar interaction i.e. the energy of interaction would be order of  $\hbar\Delta$ . Due to the hexagonal crystal structure of  $2\text{H-NbSe}_2$  and small electric quadrupole moment of  $+33\text{ mB}$ , we would have expected the resonance line to be split by the quadrupolar interaction present at any non-cubic site. The absence of resolved splitting indicates that the electric field gradient at the  $^8\text{Li}$  site is at least 10-100 times smaller than observed in most other non-cubic structures [38].

The linewidth is attributed mainly to nuclear dipolar broadening plus some unresolved quadrupolar splitting. The small asymmetry in the opposite helicities in Fig. 4.4(a) gives an upper limit of quadrupolar strength ( $<1\text{kHz}$ ). The Se (77% abundance) should have a small dipolar interaction with  $^8\text{Li}$  compared to the interaction with Nb since the magnetic moment for Nb is  $6.8\mu_N$  and the moment for Se is  $0.9\mu_N$ , where  $\mu_N$  is the neutron magnetic moment.

The top and middle panel of the Fig 5.3 are almost identical, confirming that there is no significant contribution to the line broadening in high field as such an effect would scale with magnetic field. When the field is parallel to the a-b plane (bottom panel of Fig 5.3), the width is reduced to  $1.5\text{kHz}$ . This is consistent with the fact that  $^8\text{Li}$  occupies a site in Van der Waals gap since we would expect greatest line broadening from Nb moments and quadrupolar splittings when field is parallel to c-axis. In this case, the secular term  $I_z S_z$  in Eqn 3.5 depend on a term involving  $(1 - 3\cos^2\theta)$  where  $\theta$  is the angle between the applied field and the Li-Nb interaction direction.

## 5.2 Low Field Measurements in the Normal State

The time dependence of the asymmetry at 8K is shown in Fig 5.4 for three different fields. These spectra were taken with a 4s beam pulse. Excellent fits were obtained assuming a single exponential relaxation function as may be seen from solid curves.  $\frac{1}{T_1}$  vs  $B$  was fitted using a semi-phenomenological form given in Eq. 3.39,

$$\frac{1}{T_1} = \frac{\Delta^2 \tau_c}{1 + (\gamma B \tau_c)^2}, \quad (5.1)$$

$$= \frac{\frac{\Delta^2}{\tau_c}}{\left(\frac{1}{\tau_c}\right)^2 + (\gamma B)^2}, \quad (5.2)$$

where the two free parameters are  $\Delta$ , an effective nuclear dipolar field strength, and  $\tau_c$ , the correlation time for this field to fluctuate.

As may be noted from Eq. 5.2, the  $^8\text{Li}$  relaxation rate is dependent on the local magnetic field  $^8\text{Li}$  is in, a measurement of relaxation rate will thus be a sensitive probe of magnetic field. At high field,  $\gamma B \tau_c \gg 1$  and the equation 5.1 becomes

$$\frac{1}{T_1} \simeq \frac{\Delta^2}{(\gamma B)^2 \tau_c}, \quad (5.3)$$

with the only fitting parameter being  $\frac{\Delta^2}{\tau_c}$ . To extract both  $\Delta$  and  $\tau_c$ , a slightly modified form (equation 5.2) was used for fitting. The fitted values of the parameters are

$$\begin{aligned} \frac{\Delta^2}{\tau_c} &= (0.71 \pm 0.01) \text{ kHz}^3, \\ \frac{1}{\tau_c} &= (2.96 \pm 0.1) \text{ kHz}, \end{aligned} \quad (5.4)$$

yielding

$$\begin{aligned} \Delta &= (0.49 \pm 0.04) \text{ kHz}, \\ \tau_c &= (0.34 \pm 0.01) \text{ ms}. \end{aligned} \quad (5.5)$$

The values of the fitted parameters are reasonable since dipolar fluctuation time is in the order of ms [29]. Fig 5.5 shows the fitted values of  $\frac{1}{T_1}$  as a function of field at  $T = 8K$ . The solid curve is a fit to the semi-phenomenological form given by Eqn. 3.39.

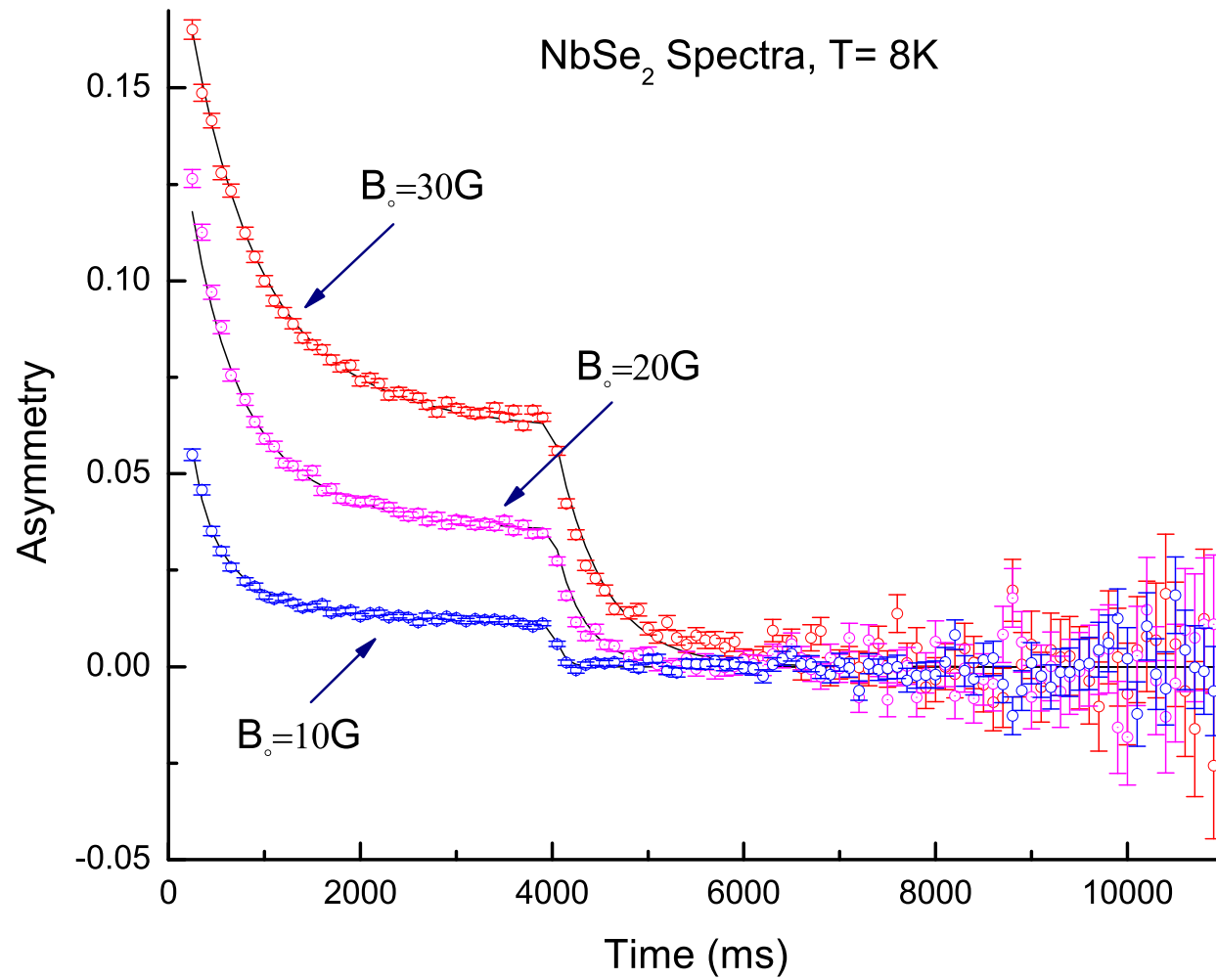
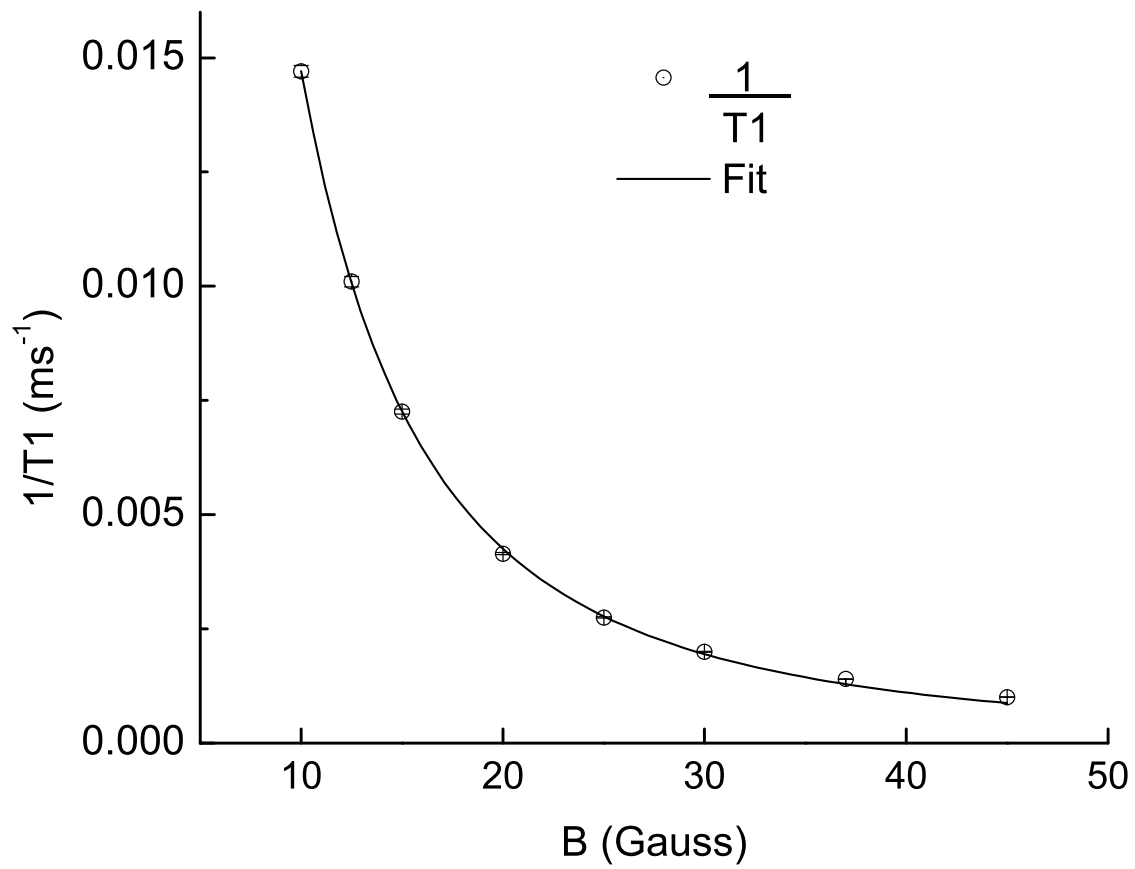


Figure 5.4: Three different field spectra and the corresponding fits.

Figure 5.5: Dependence of relaxation rate on magnetic field at  $T = 8K$ .

### 5.3 Low Field Measurements in the Meissner State

The sample was then cooled to (practical base) a temperature  $\sim 3.4\text{K}$ , in zero magnetic field (to avoid any flux trapping) and then the  $30\text{G}(\parallel ab \text{ plane})$  field was turned on, to get into the Meissner state. A set of three spectra corresponding to temperatures  $3.75\text{K}$ ,  $6.15\text{K}$  and  $6.4\text{K}$  and corresponding fits, to single exponential relaxation model (Eq. 4.5 and Eq. 4.7), are shown in Fig 5.6. It may be noted that the amplitude at  $t = 4\text{s}$  decreases by 50% as the temperature is lowered from  $6.4\text{K}$  to  $6.15\text{K}$ , whereas a similar decrease in amplitude requires a change in temperature from  $6.15\text{K}$  to  $3.75\text{K}$ . This is an indication of the fact that the relaxation rate  $\frac{1}{T_1}$  (and thereby  $\lambda_L(T), \xi(T)$ ) doesn't vary significantly until near the critical temperature.

The open diamonds in Fig 5.7 represent the fitted  $\frac{1}{T_1}$ . The fits yield an "average" relaxation rate of  $^8\text{Li}$  in  $\text{NbSe}_2$  since  $^8\text{Li}$  experiences a range of fields in the Meissner state.

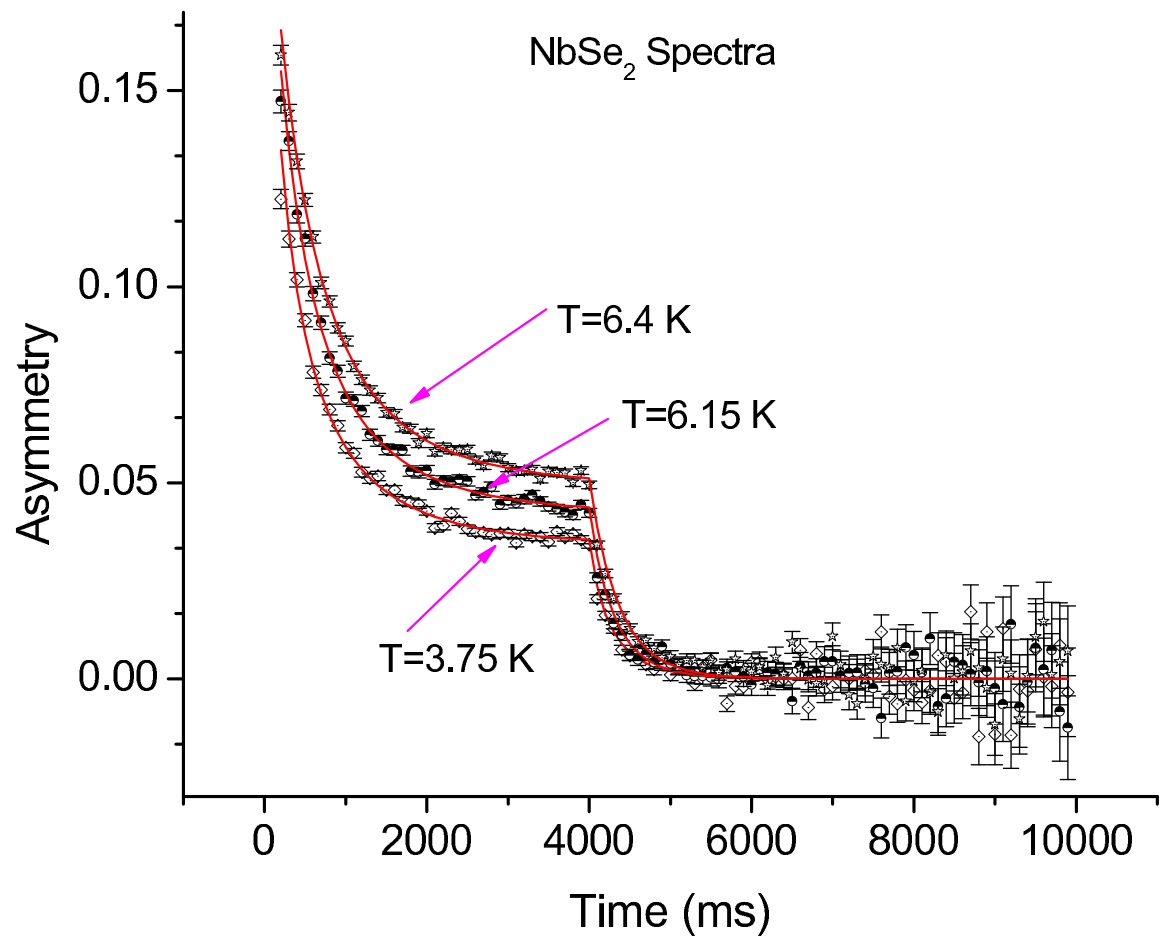


Figure 5.6: Time differential spectra at three temperatures, 3.75K, 6.15K and 6.4K, in long pulse method. Applied magnetic field  $B = 30\text{G}$  for all the runs.

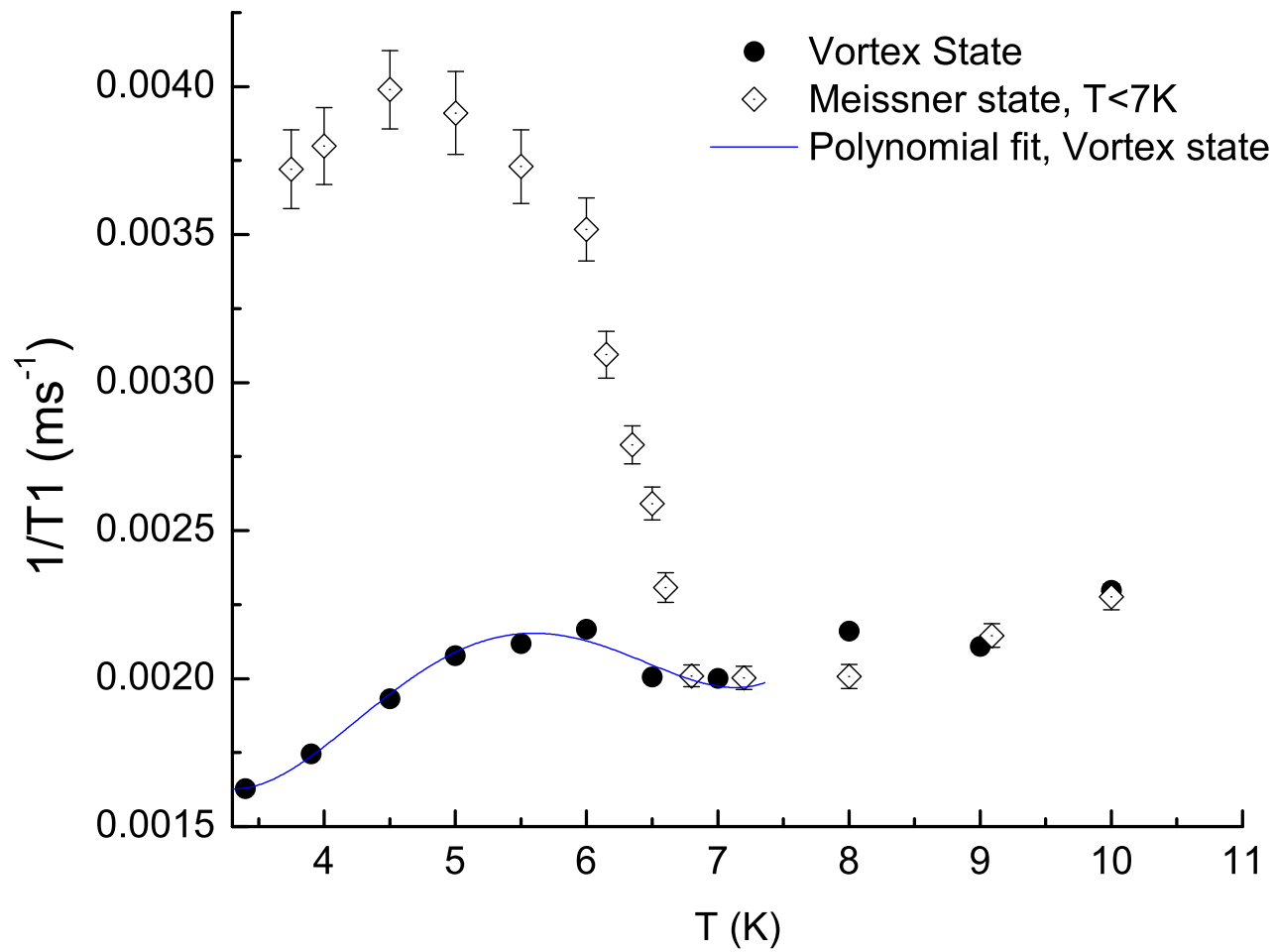


Figure 5.7: Comparison of average relaxation rate between the vortex state and the Meissner state.

## 5.4 Low Field Measurements in the Vortex State

It is necessary to account for the temperature dependence of the relaxation rate at constant magnetic field due to changes in  $\tau_c$  with temperature. Ideally, this should be done at higher field in the vortex state using time differential measurements of  $\frac{1}{T_1}$ . In the vortex state, the average field is almost unchanged so that any T-dependence in  $\frac{1}{T_1}$  is due to change in the  $\tau_c$  and not from changes in the magnetic field due to screening by the superconductor. However, without such measurements, it was necessary to use time integrated measurements of  $\frac{1}{T_1}$  in the vortex state. The vortex state relaxation rates were extracted from the time-integrated asymmetry where the “baseline asymmetry” encodes the information about relaxation rate  $\frac{1}{T_1}$ , since the polarization in absence of any RF field is given by

$$\begin{aligned}\overline{P}_z(T) &= \frac{1}{\tau} \int_0^\infty P_z(T, t) \exp\left[-\frac{t}{\tau}\right] dt, \\ &= \frac{1}{\tau} \int_0^\infty P_o \exp\left[-\frac{t}{T_1}\right] \exp\left[-\frac{t}{\tau}\right] dt, \\ &= P_o \frac{\tau'}{\tau},\end{aligned}\tag{5.6}$$

where

$$\frac{1}{\tau'} = \frac{1}{\tau} + \frac{1}{T_1},\tag{5.7}$$

$P_o$  is the initial asymmetry,  $\tau$  is the  $^8\text{Li}$  lifetime and  $T_1$  is the relaxation time.  $\frac{1}{T_1}$  may be written as

$$\frac{1}{T_1} = \frac{1}{\tau} \left[ \frac{P_o}{\overline{P}_z} - 1 \right],\tag{5.8}$$

where,  $P_o$  is adjusted to match the relaxation rate we measure from time-differential measurement at  $T = 7K$ . The 7K temperature is chosen to be the point of reference as the zero-field critical temperature is  $\approx 7.2K$ .

Fig 5.8 gives time-integrated polarization, as a function of radiofrequency, for three temperatures with an applied magnetic field  $H = 125G$ . The “baseline asymmetry” becomes smaller as temperature goes from 3.9K to 5.5K but rises up again as temperature goes up from 5.5K. Closed circles in Fig. 5.7 represent fitted  $\frac{1}{T_1}$  and the solid curve is a phenomenological polynomial fit to the relaxation rates. It may be noted from Fig. 5.7 that the time-differential and the time-integrated relaxation rates match quite reasonably except at  $T = 8K$ . However, initial asymmetry from the neutral

beam monitor <sup>1</sup> indicates that the <sup>8</sup>Li<sup>+</sup> beam was steady. It is possible that the beam spot on the sample moved from its center position yielding lower count rates and thereby reducing initial asymmetry yielding a higher  $\frac{1}{T_1}$  than we would have expected. The temperature dependence of the vortex state has a peak in  $\frac{1}{T_1}$  at about  $0.8T_c$  which we identify as the Hebel-Slichter coherence peak [39]. However, a peak usually occurs in a conventional superconductor at  $T \approx 0.9T_c$  [40]. Recent microwave conductivity measurements in MgB<sub>2</sub> [41] found a coherence peak at  $\approx 0.6T_c$ , which is attributed to be the result of a second smaller energy gap. The temperature dependence of the relaxation rate, in vortex state, is accounted for via a phenomenological function  $s(T)$  where

$$s(T) \equiv \frac{\overline{P}(T)}{P(T=7K)}, \quad (5.9)$$

and the relaxation rate may then be written as

$$\frac{1}{T_1} \simeq g(B) \times s(T), \quad (5.10)$$

where  $B_o$ ,  $\lambda_L$ ,  $\xi$ ,  $g(B)$  are applied magnetic field, London penetration depth and coherence length, field dependent relaxation rate (Eq. 5.1), respectively. The assumption that  $\frac{1}{T_1}$  may be written as a product of  $g(B)$  and  $s(T)$ , is strictly valid only at high magnetic fields since  $\tau_c$  shouldn't vary with magnetic field. However, for small changes in temperature (3.4K - 7K), Eq. 5.10 may still be considered as a good approximation.

These measurements, coupled with the <sup>8</sup>Li range distribution within NbSe<sub>2</sub>, discussed in the next section, may then be used for extracting  $\lambda_L$  and  $\xi$ .

## 5.5 Stopping Distribution

To properly interpret our measurements, we also require knowledge of the <sup>8</sup>Li range and range distribution inside the sample. We calculated the depth profile of <sup>8</sup>Li using Numerical Monte Carlo program TRIM.SP [42, 43]. Programs like TRIM.SP are largely untested at low energy, nevertheless, there has been work done to test the code using  $\beta$ -NMR technique [44]. These results indicate that reliable values for implantation depth of <sup>8</sup>Li in NbSe<sub>2</sub> may be obtained using TRIM.SP. The stopping distribution is shown

<sup>1</sup>See Ch. 4 for a discussion

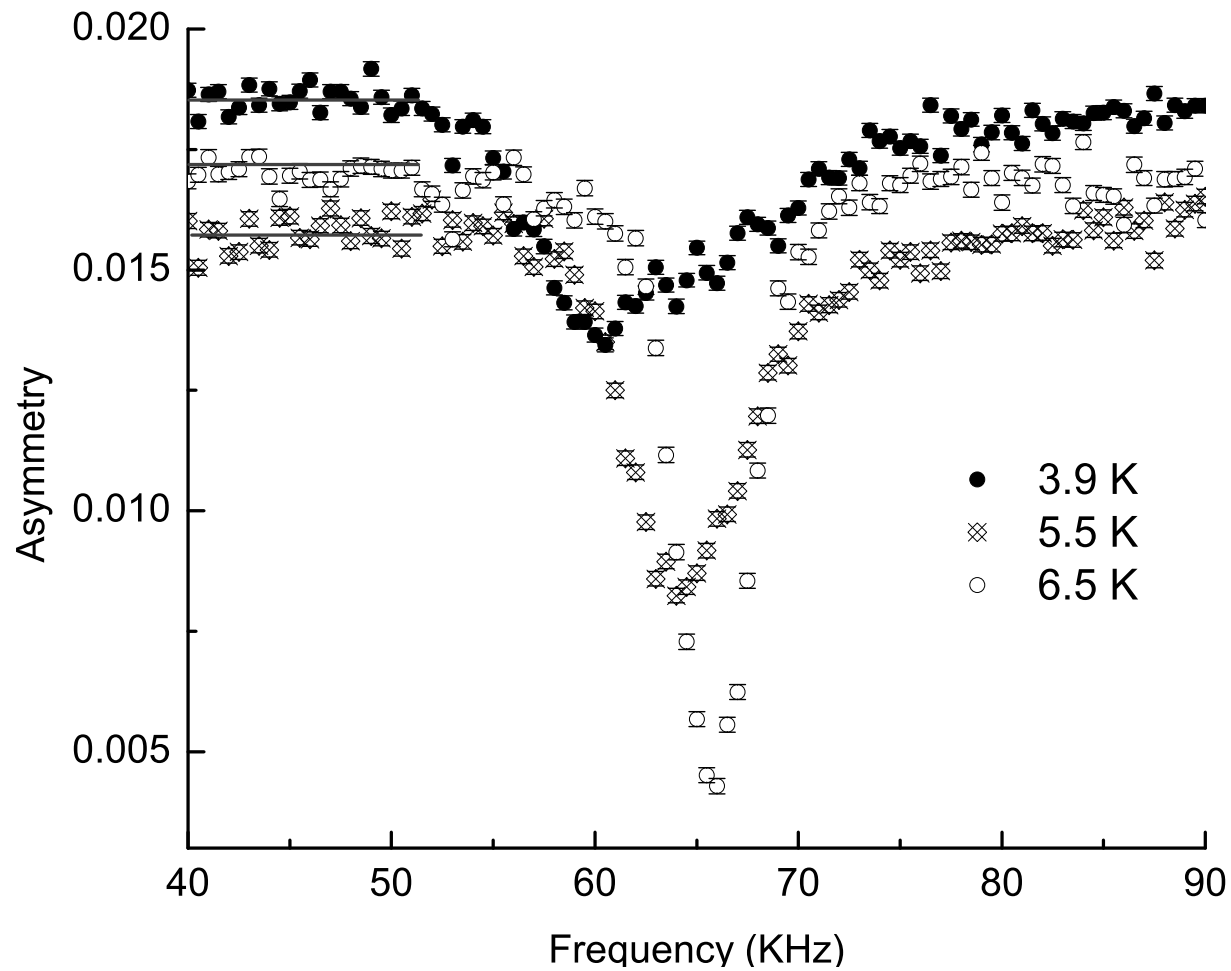


Figure 5.8: Three time integrated spectra at  $B = 125\text{G}$ . Solid lines represent fitted baseline. Resonance line shape changes due to the asymmetrical field distribution in the vortex state.

in Fig 5.9. A phenomenological function involving a Gaussian and a beta function of form

$$\rho(x) = N \left( \frac{x}{x_m} \right)^\alpha \left( 1 - \frac{x}{x_m} \right)^\beta \exp \left[ - \left( \frac{x - x_m}{\sigma} \right)^2 \right] \quad x < x_m \quad (5.11)$$

, where  $N$  is a normalization constant, was used to fit the simulation. The fitted parameters are found to be

$$\begin{aligned} \alpha &= 0.51, \\ \beta &= 3.54, \\ \sigma &= 2490 \text{Å}, \\ x_m &= 4111 \text{Å}. \end{aligned} \quad (5.12)$$

Although, theoretically it's possible that a few of  $^8\text{Li}$  stop beyond  $x_m$ , the probability is vanishingly small. It is clear that equation 5.11 provides a very good approximation to the TRIM.SP result and has the advantage of greatly speeding up the fitting procedure. The normalized stopping distribution  $\rho(x)$  determines the probability per unit depth of  $^8\text{Li}$  stopping at a certain depth  $x$  and was used to fit the observed spectra in the superconducting state and the normalization constant is chosen such that

$$\int_0^\infty \rho(x) dx = 1, \quad (5.13)$$

to ensure that the sum of probabilities of  $^8\text{Li}$  stopping somewhere inside the sample is 1.

## 5.6 Analysis and fitting to determine $\lambda_L$ and $\xi$

In this section,  $\beta$ -NMR measurements of London penetration depth  $\lambda_L$  and coherence length  $\xi$  are presented. To fit the experimentally observed  $P(t)$ , we need the functional dependence of the relaxation rate ( $\frac{1}{T_1}$ ) on the magnetic field  $B$  and the magnetic field's ( $B(x)$ ) dependence on depth  $x$ . Analysis is done using two models for the internal magnetic field.

- In the simple exponential model, the order parameter  $|\phi(r)|$  is assumed to be at it's full value everywhere in the superconductor. In particular, there is no suppression of  $|\phi(r)|$  near the surface. In this case, the magnetic field is given by

$$B(x) = B_0 \exp \left[ - \frac{x}{\lambda_L} \right] \quad (5.14)$$

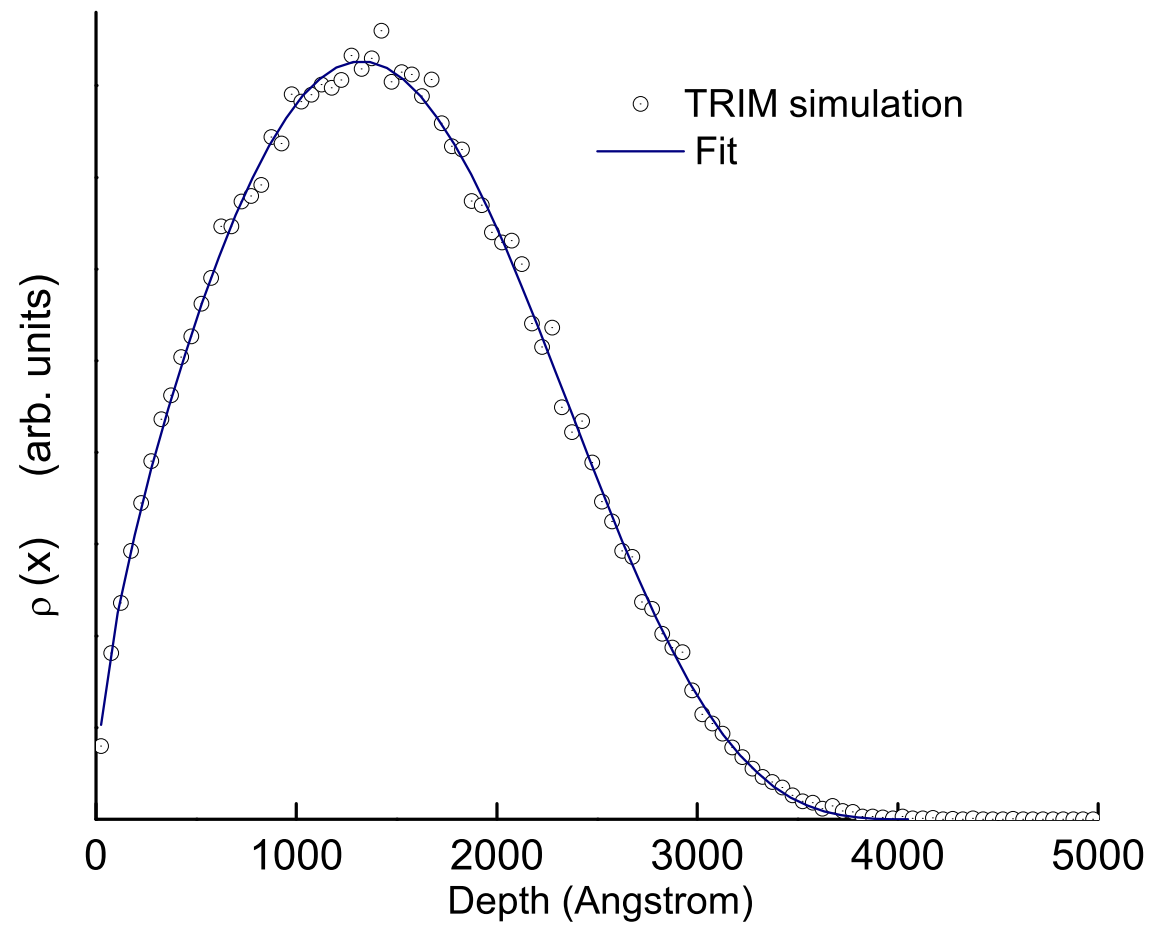


Figure 5.9: Monte Carlo calculated stopping distribution  $\rho(x)$ . Maximum depth  ${}^8\text{Li}$  reaches, at energy 28KeV, is  $\approx 4100\text{\AA}$  and the profile is centered at  $\approx 1360\text{\AA}$ .

- In the more complex ( $\xi$ ) model,  $|\phi(r)|$  is allowed to vary near the surface. In particular, we assume a boundary condition  $\phi = 0$  at  $x = 0$ . Then  $B(x)$  is approximated by,

$$B(x) = B_o \left[ 1 + \left\{ \exp \left[ \frac{\sqrt{2}\xi \tanh\left(\frac{x}{\sqrt{2}\xi}\right)}{\lambda_L} \right] - 1 \right\} \tanh\left(\frac{x}{\sqrt{2}\xi}\right) \right] \\ \times \exp \left[ -\frac{x \tanh\left(\frac{x}{\sqrt{2}\xi}\right)}{\lambda_L} \right]. \quad (5.15)$$

In both analysis, stopping distribution of  ${}^8\text{Li}$  is assumed to be the same as given in equation 5.11.

Now, we have the polarization function  $P(\frac{1}{T_1}, t)$  as function of relaxation rate  $\frac{1}{T_1}$  (see Eq. 4.5 and Eq. 4.7) and  $\frac{1}{T_1}$  is functionally dependent on magnetic field  $B$  which, in turn, depends on depth( $x$ ) from surface. The function  $P(\frac{1}{T_1}, t)$  may be symbolically written as  $P(\frac{1}{T_1}(B(x)), t)$ . The polarization at time  $t$  is the average polarization over the stopping distance of  ${}^8\text{Li}$ , namely

$$\overline{P(t)} = \int_0^\infty P(x, t) \rho(x) dx, \quad (5.16)$$

where  $\rho(x)$  is the normalized stopping distribution of  ${}^8\text{Li}$  inside NbSe<sub>2</sub> and is shown in Fig. 5.9.

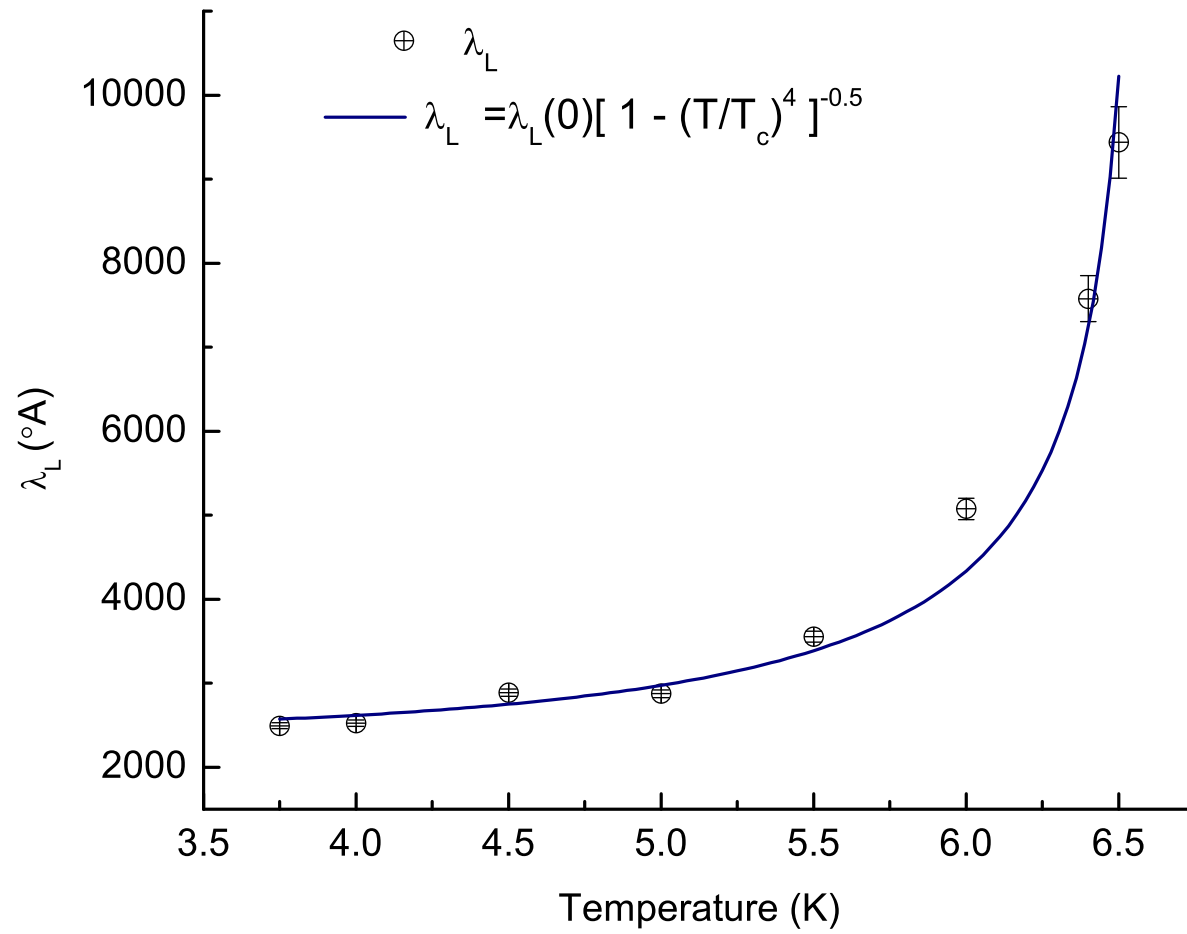
The function  $\overline{P(t)}$  does not have a closed form time dependence since it is composed of a series of exponentials. Computer code was generated to evaluate  $\overline{P(t)}$  and nonlinear least squares fitting algorithm, based on MINUIT [45] was used to fit  $\overline{P(t)}$  to the observed asymmetries of eight time-differential measurements (each representing a different temperature) with shared initial asymmetry and common ratio of penetration depth and coherence length.

Fig 5.10 shows the fitted (with shared initial asymmetry) penetration depth and it's fit according to the empirical model for  $\lambda_L(T)$  using the "Exponential field" model for magnetic field  $B(x)$ .

Fig 5.11 gives the fitted  $\lambda_L(T)$  and  $\xi(T)$  according to the " $\xi$  model". The fitted  $\lambda_L(T)$  and  $\xi(T)$  were further fitted with the  $T^4$  model for  $\lambda_L(T)$  where,

$$\frac{\lambda_L(T)}{\xi(T)} = \frac{\kappa_0}{\left[ 1 + \left( \frac{T}{T_c} \right)^2 \right]}. \quad (5.17)$$

The fitted results are shown in table 5.1.

Figure 5.10: Penetration depth as a function of temperature for an exponential model for  $B(x)$ .

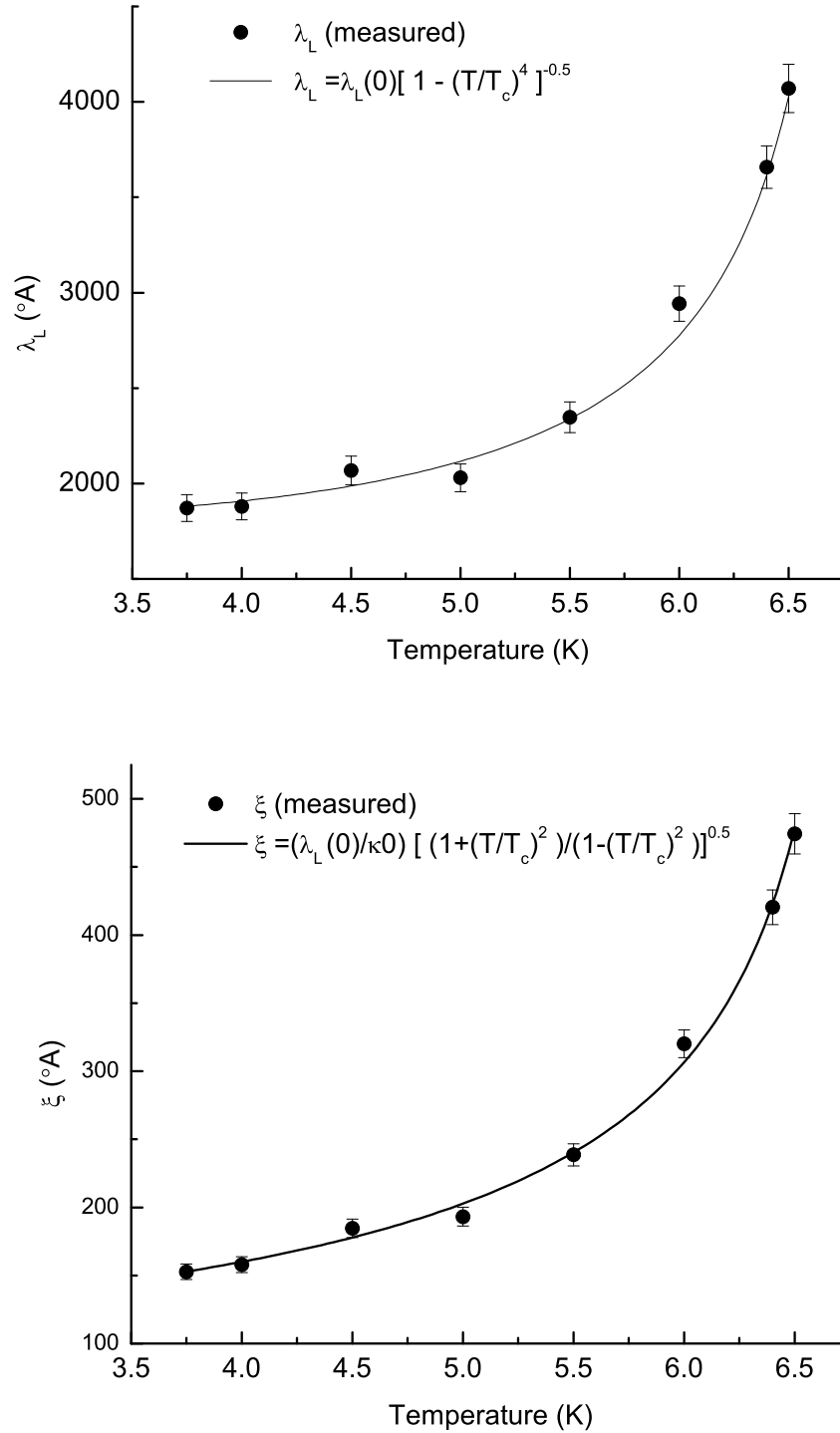


Figure 5.11: Penetration depth and coherence length as a function of temperature.

Model for $B(x)$	$\lambda_L(0)$	$\xi(0)$	$T_c$
Exponential	2434(17)	–	6.6(1)
$\xi$ model	1795(21)	146(1)	6.87(2)

Table 5.1: Penetration depth  $\lambda_L(0)$  and coherence length  $\xi(0)$  at  $T = 0$ 

As can be seen from the table 5.1, that the penetration depth in the case of “exponential  $B(x)$ ” is larger than that from “ $\xi$  model” . This is reasonable since the magnetic field in the second model doesn’t change significantly up to a depth  $\approx \xi$  and the change in relaxation rate in this region is small. This in turn leads to a smaller value of  $\lambda_L$  since the average relaxation rate must remain about the same. The global fits in two models yield

$$\begin{aligned} \frac{\chi^2}{DF} &= 1.3535 \quad \text{exponential } B(x) \\ &= 1.3268 \quad \xi \text{ model} \end{aligned} \quad (5.18)$$

with DF being the degree of freedom in the fit. Even though the ‘goodness of fit’ of both models are nearly same, the empirical  $T^4$  model for  $\lambda_L$  fits significantly better in the “ $\xi$  model”,

$$\begin{aligned} \frac{\chi^2}{DF} &= 12.0 \quad \text{exponential } B(x) \\ &= 0.84 \quad \xi \text{ model} \end{aligned} \quad (5.19)$$

in particular.

This is evidence that the second model is more realistic as the  $T^4$ -dependence is expected to be robust. In other words, the superconducting order parameter is reduced at surface compared to the bulk. For consistency, one would expect that the average field, calculated from the expression 5.20 and using the fit parameters from table 5.1,

$$\langle B \rangle = \int_0^\infty B(x)\rho(x)dx \quad (5.20)$$

to be equal to each other and also be equal to the magnetic field corresponding to average depth

$$\bar{x} = \int_0^\infty x\rho(x)dx \quad (5.21)$$

However, the average magnetic fields in the two models differ by about a Gauss. This is due to the fact that the two models fit to two different initial

T	$\langle B \rangle$ ( $\xi$ model)	$\langle B \rangle$ (Exponential B(x))
3.75	16.6	17.4
6.5	24.9	25.8

Table 5.2: Average magnetic field, calculated using parameter in two models.

amplitudes differing by  $\sim 5\%$ . Refitting the data with an average of two amplitudes from the previous fits, the resulting  $\lambda_L(T)$  and  $\xi(T)$  are shown in Fig 5.12 and Fig 5.13.

Fitted  $\lambda_L(0)$  and  $\xi(0)$  are shown in table 5.3 The previous fit of the “ $\xi$  model” yields higher overall amplitude than that from the “exponential model”. When fitted with the average amplitude from the two previous fits, the “ $\xi$  model” yields lower  $T_c$  to account for the low relaxation rate since a higher magnetic field would yield lower  $\frac{1}{T_1}$ . As a consequence,  $T_c$  is suppressed compared to the previous fit where fits were done independently for two models, as may be noted from table 5.3.

Model for B(x)	$\lambda_L(0)$	$\xi(0)$	$T_c$
Exponential	2341(6)	–	6.6(1)
$\xi$ model	2005(14)	169(1)	6.79(1)

Table 5.3: Penetration depth  $\lambda_L$  and coherence length  $\xi$  at temperature  $T = 0K$ , using a common initial amplitude for fitting.

The average magnetic fields computed from the fitted parameters shown in Table 5.3 in two models are shown in table 5.4

T	$\langle B \rangle$ ( $\xi$ model)	$\langle B \rangle$ (Exponential B(x))
3.75	17.03	17.06
6.5	25.4	25.23

Table 5.4: Average magnetic field, in two models, using parameters from table 5.3

The average magnetic fields are equal to each other within  $\approx 2\%$ . The ‘goodness of fit’, i.e,  $\frac{\chi^2}{DF}$  gets slightly worse (approximately twice the previous fit) for both fits since the average amplitude isn’t the best fit amplitude for any of them. However, one feature that remains similar with the previous fit is the critical temperature of corresponding models.  $T_c$  in ‘ $\xi$ -model’

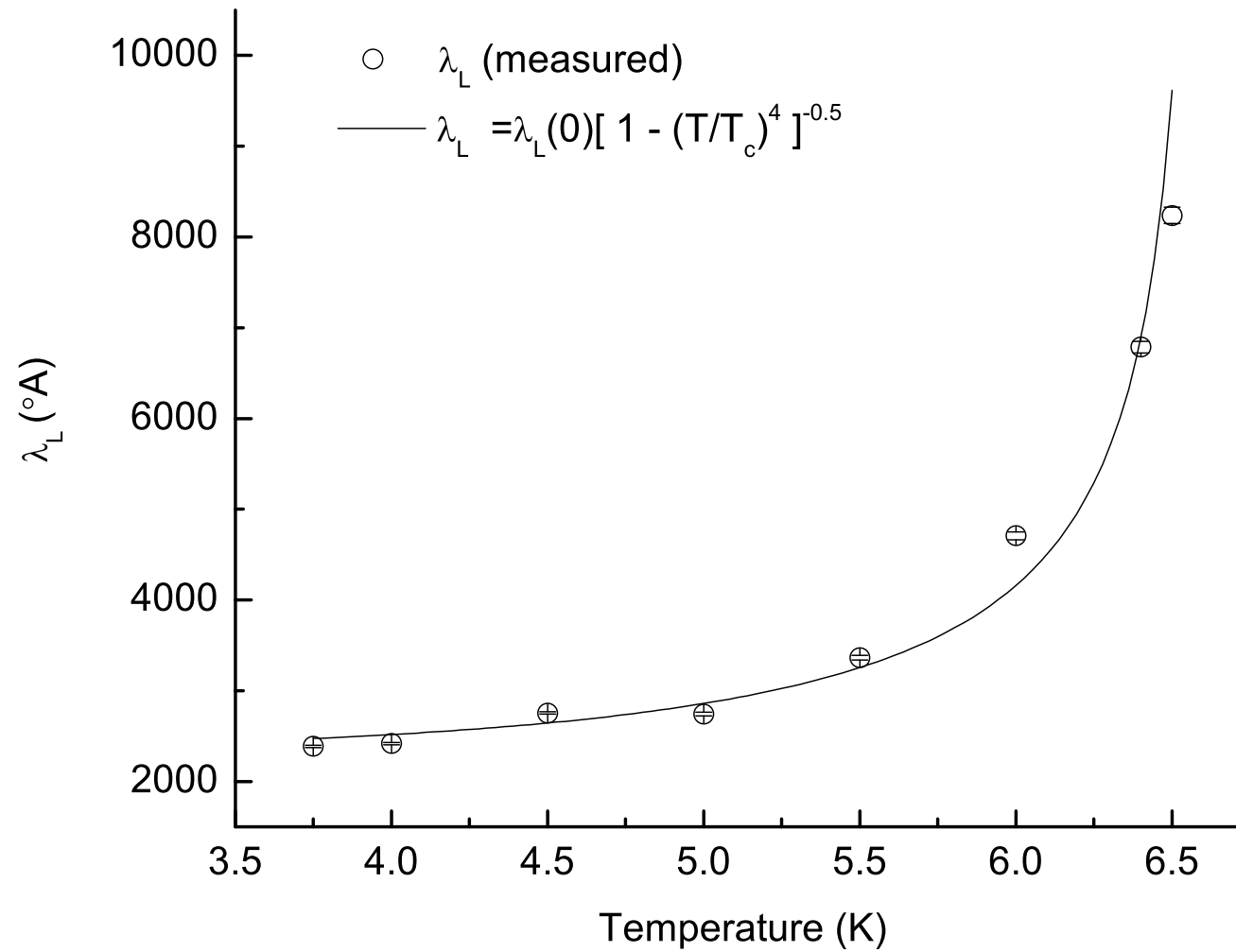


Figure 5.12: Penetration depth as a function of temperature for an exponential model for  $B(x)$  with average overall amplitude.

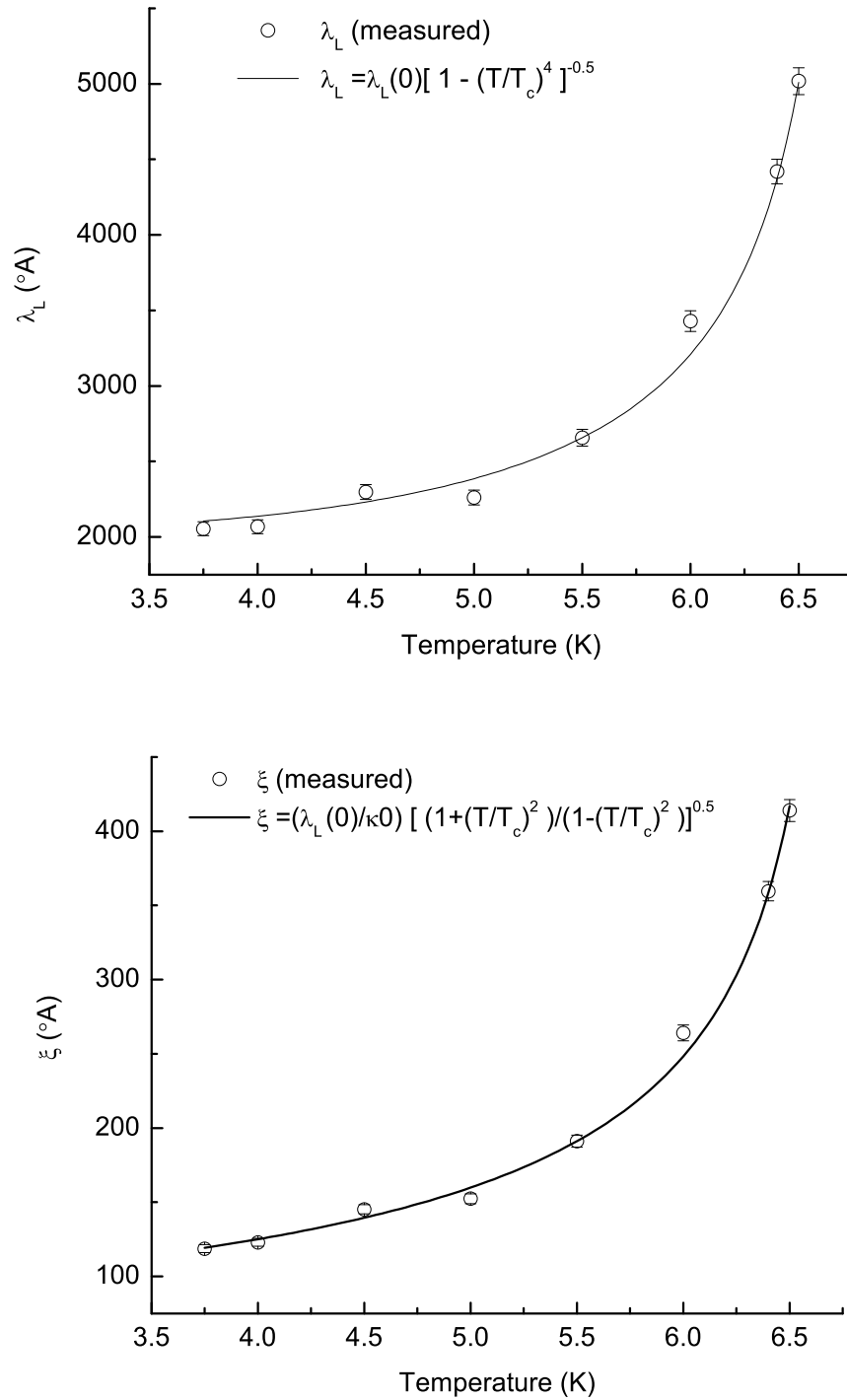


Figure 5.13: Penetration depth and coherence length as a function of temperature with average overall amplitude, for “ $\xi$  model”.

with the fixed initial asymmetry fit is  $\sim 1.2\%$  lower than that from varying initial asymmetry fit. This is reasonable when compared to a corresponding drop in initial asymmetry by  $\sim 2.5\%$ , as explained above.

## Chapter 6

# Summary & Conclusions

We have investigated the normal and the Meissner state of NbSe<sub>2</sub> using spin polarized <sup>8</sup>Li. In the normal state of NbSe<sub>2</sub>, at high field, the relaxation rate increases with temperature, a result we identify with Korringa relaxation, where the dominant interaction is via the conduction electrons scattering off <sup>8</sup>Li nuclei. The Korringa constant is an order of magnitude smaller compared to that in Ag, indicating <sup>8</sup>Li, with a small hyperfine coupling, occupying a site in the Van der Waals gap where the overlap with the conduction band is small. Absence of resolved line splittings in frequency measurements indicate that electric field gradient in <sup>8</sup>Li sites is also very small compared to other non-cubic crystals.

In low fields, the fluctuating dipolar fields from nuclear spin dynamics, dominates the relaxation process.  $\frac{1}{T_1}$  shows a Lorentzian behavior as a function of applied magnetic field  $B$ . The equation for  $\frac{1}{T_1}$  was used to extract the dipolar field strength  $\Delta$  and correlation time  $\tau_c$ , in the normal state at  $T = 8K$ . The values of  $\Delta$  and  $\tau_c$  are reasonable since they are on the order of kHz and ms, respectively. From the vortex state measurements, we obtain the temperature dependence of  $\tau_c$ . The temperature dependence of  $\tau_c$  combined with the field dependence of  $\frac{1}{T_1}$  was then used to extract the coherence length  $\xi$  and London penetration depth  $\lambda_L$ , depending on the model for magnetic field distribution inside NbSe<sub>2</sub>. The two models for magnetic field distribution inside NbSe<sub>2</sub> gives similar  $\chi^2/DF$ . Although absolute value of  $\lambda_L(T = 0)$  is slightly different depending on the assumed magnetic field distribution model inside in Meissner state, the temperature dependence of  $\lambda_L(T)$  fits much better to the two-fluid temperature dependence model, when there is a suppression of order parameter  $\phi(r)$ , near the surface. As our sample was cleaved in air, it's possible that oxidation on surface had an effect on suppressing the order parameter near surface. One way of improving the measurement would be to cleave the sample in vacuum and perhaps cap it with Ag. Since, the average magnetic field in the two models give nearly same value even with independent amplitudes, one way of distinguishing between models would be to do measurements at different implantation energies so that the average implantation depth  $\bar{x}$  and

---

the corresponding average magnetic field  $\langle B \rangle$  would be different from one another.

We have measured  $\lambda_L(T)$  in the Meissner state as a function of temperature which is the first of its kind, since it is a direct measurement of the magnetic field distribution.  $\beta$ NMR measurements in the Meissner state are a completely general method of measuring internal field distribution and can be used in a wide variety of superconductors. In these measurements, only the relaxation rate  $\frac{1}{T_1}$  tells us the internal field distribution and is thereby sensitive to the absolute values of  $\xi$  and  $\lambda_L$  and the nature of boundary conditions at surface. This method has distinct advantages over other methods for measuring  $\xi$  and  $\lambda_L$ , where it is very hard to determine the absolute values of the parameters.

# Bibliography

- [1] Heike Kamerlingh Onnes. The resistance of pure mercury at helium temperatures. *Comm. Leiden.*, 120 b, 1911.
- [2] W. Meissner and R. Oschenfel. *Naturwiss.*, 21(787), 1933.
- [3] F. London and H. London. *Proc. R. Soc. London*, A149(71), 1935.
- [4] V.L. Ginzburg and L.D. Landau. *Zh. Eksp. Teor. Fiz.*, 20(1064), 1950.
- [5] J. Bardeen, L.N. Cooper, and J.R. Schrieffer. *Phys. Rev.*, 108(1175), 1957.
- [6] L. N. Cooper. *Phys. Rev.*, 104(1189), 1956.
- [7] J G Bednorz and Muller K A. A possible high  $T_c$  superconductivity in the Ba-La-Cu-O system. *Z. Phys. B.-Condens. Matter*, 54:189–93, 1986.
- [8] J. E. Sonier, R. F. Kiefl, J. H. Brewer, J. Chakhalian, S. R. Dunsiger, W. A. MacFarlane, R. I. Miller, and A. Wong. Muon-spin rotation measurements of the magnetic field dependence of the vortex-core radius and magnetic penetration depth in NbSe<sub>2</sub>. *Phys. Rev. Letter.*, 79:1742–1745, 1997.
- [9] A. T. Fiory, A. F. Hebard, P. M. Mankiewich, and R. E. Howard. Renormalization of the mean-field superconducting penetration depth in epitaxial YBa<sub>2</sub>Cu<sub>3</sub>O<sub>7</sub> films. *Phys. Rev. Lett*, 61:1419–1422, 1988.
- [10] W. N. Hardy, D. A. Bonn, D. C. Morgan, Ruixing Liang, and Kuan Zhang. Precision measurements of the temperature dependence of  $\lambda$  in YBa<sub>2</sub>Cu<sub>3</sub>O<sub>6.95</sub>: Strong evidence for nodes in the gap function. *Phys. Rev. Lett.*, 70:3999–4002, 1993.
- [11] Zhengxiang Ma, R. C. Taber, L. W. Lombardo, A. Kapitulnik, M. R. Beasley, P. Merchant, C. B. Eom, S. Y. Hou, and Julia M. Phillips. Microwave penetration depth measurements on Bi<sub>2</sub>Sr<sub>2</sub>CaCu<sub>2</sub>O<sub>8</sub> single

- 
- crystals and  $\text{YBa}_2\text{Cu}_3\text{O}_{7-\delta}$  thin films. *Phys. Rev. Lett.*, 71:781–784, 1993.
- [12] N. Klein, N. Tellmann H. Schulz, and K. Urban. Evidence of two-gap s-wave superconductivity in  $\text{YBa}_2\text{Cu}_3\text{O}_{7-x}$  from microwave surface impedance measurements. *Phys. Rev. Lett.*, 71:3355–3358, 1993.
- [13] R.F. Kiefl, W.A. MacFarlane, G.D. Morris, P. Amaudruz, D. Arsenneau, H. Azumi, R. Baartman, T.R. Beals, J. Behr, C. Bommas, J.H. Brewer, K.H. Chow, E. Dumont, S.R. Dunsiger, S. Daviel, L. Greene, A. Hatakeyama, R.H. Heffner, Y. Hirayama, B. Hitti, S.R. Kreitzman, C.D.P. Levy, R.I. Miller, M. Olivo, and R. Poutissou. Low energy spin polarized radioactive beams as a nano-scale probe of matter. *Physica B*, 326:189–195, 2003.
- [14] K.H. Chow, Z. Salman, R.F. Kiefl, W.A. MacFarlane, C.D.P. Levy, P. Amaudruz, R. Baartman, J. Chakhalian, S. Daviel, Y. Hirayama, A. Hatakeyama, D.J. Arsenneau, B. Hitti, S.R. Kreitzman, G.D. Morris, R. Poutissou, and E. Reynard. The new  $\beta$ -NMR facility at TRIUMF and applications in semiconductors. *Physica B*, 340:1151–1154, 2003.
- [15] C. Gros and R. Joynt T. M. Rice. *Z. Phys. B*, 68(425), 1987.
- [16] Z. Y. Weng, T. K. Lee, and C. S. Ting. *d*-wave superconducting condensation in the spin-density-wave background. *Phys. Rev. B*, 38:6561–6567, 1988.
- [17] P. Monthoux, A. V. Balatsky, and D. Pines. *Phys. Rev. Lett.*, 67:3448–3451, 1991.
- [18] J. Annett, N. Goldenfeld, and S. R. Penn. *Phys. Rev. B*, 43:2778–2782, 1991.
- [19] J. E. Sonier, M. F. Hundley, J. D. Thompson, and J. W. Brill. Low field anomaly in the specific heat of *s*-wave superconductors due to the expansion of the vortex cores. *Phys. Rev. Lett.*, 82(24):4914–3491, 1999.
- [20] Hyoungh Joon Choi, David Roundy, Hong Sun, Marvin L. Cohen, and Steven G. Louie. The origin of the anomalous superconducting properties of  $\text{MgB}_2$ . *Nature*, 418:758–760, 2002.
- [21] T. Yokoya, T. Kiss, A. Chainani, S. Shin, M. Nohara, and H. Takagi. Fermi surface sheet-dependent superconductivity in  $2\text{H-NbSe}_2$ . *Science*, 294(5551):2518–2520, 2001.

- 
- [22] Rodrigo J.G. and Vieira S. STM study of multiband superconductivity in NbSe<sub>2</sub> using a superconducting tip. *Physica C*, 404:306–310, 2004.
- [23] G. Rubio-Bollinger, H. Suderow, and S. Vieira. Tunneling spectroscopy in small grains of superconducting MgB<sub>2</sub>. *Phys. Rev. Lett.*, 86:5582–5584, 2001.
- [24] C.J. Gorter. *Paramagnetic Relaxation*. Elsevier, 1947.
- [25] Michael Tinkham. *Introduction To Superconductivity*. McGraw-Hill Companies Inc., 1996.
- [26] P.G. de Gennes. *Superconductivity of Metals and Alloys*. W.A. Benjamin, New York, 1966.
- [27] C.P. Poole, H.A. Farach, and R.J. Creswick. *Superconductivity*. Academic Press, 1995.
- [28] Kenji ISHIDA, Yoshihiro NINO, Guo-Qing ZHENG, Yoshio KITAOKA, Kunisuke ASAYAMA, and Tsukio OHTANI. <sup>93</sup>Nb Study in Layered Superconductor 2H-NbSe<sub>2</sub>. *Journal of the Physical Society of Japan*, 65(7):2341–2342, July 1996.
- [29] C.P. Slichter. *Principles of Magnetic Resonance*. Springer-Verlag, 1980.
- [30] Emil RODUNER and Hanns FISCHER. MUONIUM SUBSTITUTED ORGANIC RADICALS IN LIQUIDS. THEORY AND ANALYSIS OF  $\mu$ SR SPECTRA. *Chemical Physics*, 54, 1981.
- [31] M. Füllergrabe *et al.*, B. Ittermann, H.-J. Stckmann, F. Kroll, D. Peters, and H. Ackermann. Diffusion parameters of B in Cu determined by  $\beta$ -radiation-detected NMR. *Phys. Rev. B*, 64(224302), 2001.
- [32] R.C. Tolman. *The Principles of Statistical Mechanics*. Oxford University Press, 1938.
- [33] B. Ittermann, H. Ackermann, H.J. Stockmann, K. H. Ergezinger, M. Heemeier, F. Kroll, F. Mai, and K. Marbach D. Peters G. Sulzer. *Phys. Rev. Lett.*, 77(4784), 1996.
- [34] Hatakeyama *et al.* A. *Ninth International Workshop on Polarized Sources and Targets*. World Scientific, 2002.

- 
- [35] Z. Salman, R.F. Kiefl, K.H. Chow, W.A. MacFarlane, S.R. Kreitzman, D.J. Arseneau, S. Daviel, C.D.P. Levy, Y. Maeno, and R. Poutissou.  $\beta$ -detected nuclear quadrupole resonance with a low-energy beam of  ${}^8\text{Li}^+$ . *Physical Review B*, 70(104404), 2004.
- [36] H. Drulis, Z.G. Xu, J.W. Brill, L.E. De Long, and J.C. Hou. *Phys. Rev. B*, 44(4731), 1991.
- [37] G. D. Morris, W. A. MacFarlane, K. H. Chow, Z. Salman, D. J. Arseneau, S. Daviel, A. Hatakeyama, S. R. Kreitzman, C. D. P. Levy, R. Poutissou, R. H. Heffner, J. E. Elenewski, L. H. Greene, and R. F. Kiefl. Depth-controlled  $\beta$ -NMR of  ${}^8\text{Li}$  in a thin silver film. *Phys. Rev Lett.*, 93(157601), 2004.
- [38] Z. Salman. *Elsevier Science*, 2005.
- [39] L. C. Hebel and C. P. Slichter. *Phys. Rev.*, 113(1504), 1959.
- [40] R. F. Kiefl et. al. Coherence peak and superconducting energy gap in  $\text{Rb}_3\text{C}_{60}$  observed by muon spin relaxation. *Phys. Rev. Lett.*, 70:3987–3990, 1993.
- [41] B. B. Jin, T. Dahm, A. I. Gubin, Eun-Mi Choi, Hyun Jung Kim, Sung-IK Lee, W. N. Kang, and N. Klein. Anomalous Coherence Peak in the Microwave Conductivity of c-Axis Oriented  $\text{MgB}_2$  Thin Films . *Phys. Rev. Lett.*, 91(127006), 2003.
- [42] J.F. Ziegler and J.M. Manoyan. *Nuclear Instruments and Methods in Physics Research B*, 35:215–228, 1988.
- [43] E. Morenzoni, H. Glckle, T. Prokscha, R. Khasanov and H. Luetkens, M. Birke, E. M. Forgan, Ch. Niedermayer, and M. Pleines. Implantation studies of kev positive muons in thin metallic layers. *Nuclear Instruments and Methods in Physics Research Section B*, 192(3):254–266, May 2002.
- [44] T.R. Beals, R.F. Kiefl, W.A. MacFarlane, K.M. Nichol, G.D. Morris, C.D.P. Levy, S.R. Kreitzman, R. Poutissou, S. Daviel, R.A. Baartman, and K.H. Chow. Range straggling of low energy  ${}^8\text{Li}^+$  in thin metallic films using  $\beta$  – NMR. *Physica B*, 326:205–208, 2003.
- [45] Minuit - function minimization and error analysis. *CERN Program Library entry*, D506, 1994-1998.

## Appendix A

# Low Field Spin Relaxation from Fluctuating Dipolar Fields

This discussion is taken from C.P. Slichter, *Principles of Magnetic Resonance*, Second Edition, Springer-Verlag, 1980, Berlin; Germany.

In this section  $\frac{1}{T_1}$  due to randomly fluctuating magnetic field is discussed. Density matrix formalism is ideally suited for our system as large number of atoms are interacting at the same time and the observables are averages over all atoms. We discuss general time evolution of state  $|\psi\rangle$  of our system in the presence of a general time dependent interaction Hamiltonian  $\mathcal{H}(t)$ .

If our system is described by state  $|\psi\rangle$  then it may be expressed as linear combination of orthogonal energy states

$$|\psi\rangle = \sum_n c_n |n\rangle. \quad (\text{A.1})$$

Expectation value of an operator  $\hat{O}$  (i.e an observable) is given by

$$\langle\psi|\hat{O}|\psi\rangle = \sum_{n,m} c_m^* c_n \langle m|\hat{O}|n\rangle. \quad (\text{A.2})$$

Equation A.2 may be conveniently expressed as multiplication of two matrices

$$\begin{aligned} \langle\psi|\hat{O}|\psi\rangle &= \sum_{n,m} \langle n|\rho|m\rangle \langle m|\hat{O}|n\rangle, \\ &\equiv \text{Tr}\{\rho, \hat{O}\}, \end{aligned} \quad (\text{A.3})$$

where  $\rho$  is the density matrix with components

$$\rho_{mn} \equiv \langle m|\rho|n\rangle. \quad (\text{A.4})$$

In other words, knowing of the density matrix is equivalent to knowing the state  $|\psi\rangle$ . However, we often wish to compute average expectation value of

an operator in an ensemble of systems, i.e.,

$$\overline{\langle \hat{O} \rangle} = \sum_{n,m} \overline{c_n c_m^*} \langle m | \hat{O} | n \rangle. \quad (\text{A.5})$$

Only  $\rho_{nm}$  varies from system to system as the wavefunction varies. In subsequent discussion, the overline indicating ensemble average is omitted to simplify notation, i.e.  $\bar{\rho} = \rho$ . Assuming the Hamiltonian  $\mathcal{H}$  to be identical for all  $\psi$ 's in ensemble, the time dependence of  $\rho$  is given by

$$\frac{d\rho}{dt} = \frac{i}{\hbar} [\rho, \mathcal{H}]. \quad (\text{A.6})$$

When  $\mathcal{H}$  is independent of time (eg. static magnetic field) the solution of equation A.6 is given by

$$\rho(t) = e^{-\frac{i}{\hbar}\mathcal{H}t} \rho(0) e^{\frac{i}{\hbar}\mathcal{H}t}. \quad (\text{A.7})$$

In our case, the Hamiltonian consists of a large time-independent interaction  $\mathcal{H}_0$  (the Zeeman interaction  $-\gamma H_0 I_z$ ) and a smaller time-dependent term  $\mathcal{H}_1(t)$ . Equation of motion for  $\rho$  then becomes

$$\frac{d\rho}{dt} = \frac{i}{\hbar} [\rho, \mathcal{H} + \mathcal{H}_1]. \quad (\text{A.8})$$

To have a solution of equation A.8, a quantity is defined  $\rho^*(t)$  such that

$$\rho(t) = e^{-\frac{i}{\hbar}\mathcal{H}t} \rho^*(t) e^{\frac{i}{\hbar}\mathcal{H}t}. \quad (\text{A.9})$$

Substitution equation A.9 in equation A.8 one may get

$$-\frac{i}{\hbar} [\mathcal{H}_0, \rho] + e^{-\frac{i}{\hbar}\mathcal{H}t} \frac{d\rho^*(t)}{dt} e^{\frac{i}{\hbar}\mathcal{H}t} = \frac{i}{\hbar} [\rho, \mathcal{H}_0 + \mathcal{H}_1(t)], \quad (\text{A.10})$$

which yields

$$\frac{d\rho^*(t)}{dt} = \frac{i}{\hbar} [\rho^*, \mathcal{H}_1^*(t)] \quad (\text{A.11})$$

where

$$\mathcal{H}_1^*(t) = e^{-\frac{i}{\hbar}\mathcal{H}_0 t} \mathcal{H}_1(t) e^{\frac{i}{\hbar}\mathcal{H}_0 t} \quad (\text{A.12})$$

Using a second order iteration, the equation A.11 may be written as

$$\frac{d\rho^*(t)}{dt} = \frac{i}{\hbar} [\rho^*(0), \mathcal{H}_1^*(t)] + \left(\frac{i}{\hbar}\right)^2 \int_0^t [[\rho^*(0), \mathcal{H}_1^*(t')], \mathcal{H}_1^*(t)] dt'. \quad (\text{A.13})$$

Since  $\rho^*(0) = \rho(0)$ , a knowledge of  $\rho(0)$  and  $\mathcal{H}_1$  would lead to an expression for  $\rho^*(t)$ . Assuming that initially only eigenstate  $|k\rangle$  of  $\mathcal{H}_0$  is occupied,  $\frac{d}{dt}\langle m|\rho|m\rangle$  is the probability per second of a transition. Thus,

$$\langle n|\rho^*|m\rangle = \langle n|\rho|m\rangle = 0 \quad \text{unless } n = m = k. \quad (\text{A.14})$$

Then

$$\begin{aligned} \frac{d}{dt}\langle m|\rho^*(t)|m\rangle &= \frac{d}{dt}\langle m|\rho(t)|m\rangle \\ &+ \left(\frac{i}{\hbar}\right)^2 \int_0^t \langle m|[\mathcal{H}_1^*(t')\rho^*(0)\mathcal{H}_1^*(t) \\ &+ \mathcal{H}_1^*(t)\rho^*(0)\mathcal{H}_1^*(t')] |m\rangle dt' \end{aligned} \quad (\text{A.15})$$

Using the matrix elements,

$$\langle m|\mathcal{H}_1^*(t)|n\rangle = e^{\frac{i}{\hbar}(E_m - E_n)t} \langle m|\mathcal{H}_1(t)|n\rangle, \quad (\text{A.16})$$

and adopting a convenient notation

$$\frac{E_m}{\hbar} \equiv m, \quad (\text{A.17})$$

The equation A.15 may be written as

$$\begin{aligned} \frac{d}{dt}\langle m|\rho(t)|m\rangle &= \frac{1}{\hbar^2} \int_0^t \left[ \langle m|\mathcal{H}_1(t')|k\rangle \langle k|\mathcal{H}_1(t)|m\rangle e^{i(m-k)(t'-t)} \right. \\ &+ \left. \langle m|\mathcal{H}_1(t)|k\rangle \langle k|\mathcal{H}_1(t')|m\rangle e^{i(m-k)(t-t')} \right] dt'. \end{aligned} \quad (\text{A.18})$$

As  $\mathcal{H}_1(t)$  varies from ensemble to ensemble, we take the average of the expression in equation A.18 as

$$\begin{aligned} \frac{d}{dt}\overline{\langle m|\rho(t)|m\rangle} &= \frac{1}{\hbar^2} \int_0^t \left[ \overline{\langle m|\mathcal{H}_1(t')|k\rangle \langle k|\mathcal{H}_1(t)|m\rangle} e^{i(m-k)(t'-t)} \right. \\ &+ \left. \overline{\langle m|\mathcal{H}_1(t)|k\rangle \langle k|\mathcal{H}_1(t')|m\rangle} e^{i(m-k)(t-t')} \right] dt'. \end{aligned} \quad (\text{A.19})$$

For sake of simplicity, it may be assumed that the perturbation is stationary on the basis that the temperature of the system is steady and thereby

$$\overline{\langle m|\mathcal{H}_1(t)|k\rangle \langle k|\mathcal{H}_1(t')|m\rangle}.$$

depending on  $t$  and  $t'$  only through their difference  $\tau \equiv t - t'$  and the energy levels  $m$  and  $k$ . The dependence of  $\tau$ ,  $m$  and  $k$  is summarized by defining

“correlation function”  $G_{mk}(\tau)$  as

$$\begin{aligned} G_{mk}(\tau) &= \overline{\langle m|\mathcal{H}_1(t)|k\rangle\langle k|\mathcal{H}_1(t+\tau)|m\rangle} \\ &= \overline{\langle m|\mathcal{H}_1(t+\tau)|k\rangle\langle k|\mathcal{H}_1(t)|m\rangle} \\ &= G_{mk}(-\tau) \end{aligned} \tag{A.20}$$

where the last equality follows from the fact that  $\mathcal{H}(t)$  is stationary.  $G_{mk}(\tau)$  tells how the Hamiltonian  $\mathcal{H}_1(t)$  at time  $t$  is correlated with the Hamiltonian  $\mathcal{H}_1(t+\tau)$  at time  $t+\tau$ . Generally, the thermal movements of nuclear moments is negligible for times less than some characteristic time  $\tau_c$  called the “correlation time”, so that

$$\mathcal{H}_1(t) \approx \mathcal{H}_1(t+\tau). \tag{A.21}$$

A schematic diagram of  $G_{mk}(\tau)$  is given in Fig A.1 the equation A.19 may be written as

$$\frac{d}{dt}\overline{\langle m|\rho(t)|m\rangle} = \frac{1}{\hbar^2} \int_{-t}^t G_{mk}(\tau) e^{-i(m-k)\tau} d\tau. \tag{A.22}$$

For our measurement, resolution time  $t$  is greater than a few  $\tau_c$  and integration limit may be replaced by  $\infty$  yielding

$$\frac{d}{dt}\overline{\langle m|\rho(t)|m\rangle} = \frac{1}{\hbar^2} \int_{-\infty}^{\infty} G_{mk}(\tau) e^{-i(m-k)\tau} d\tau = W_{km}. \tag{A.23}$$

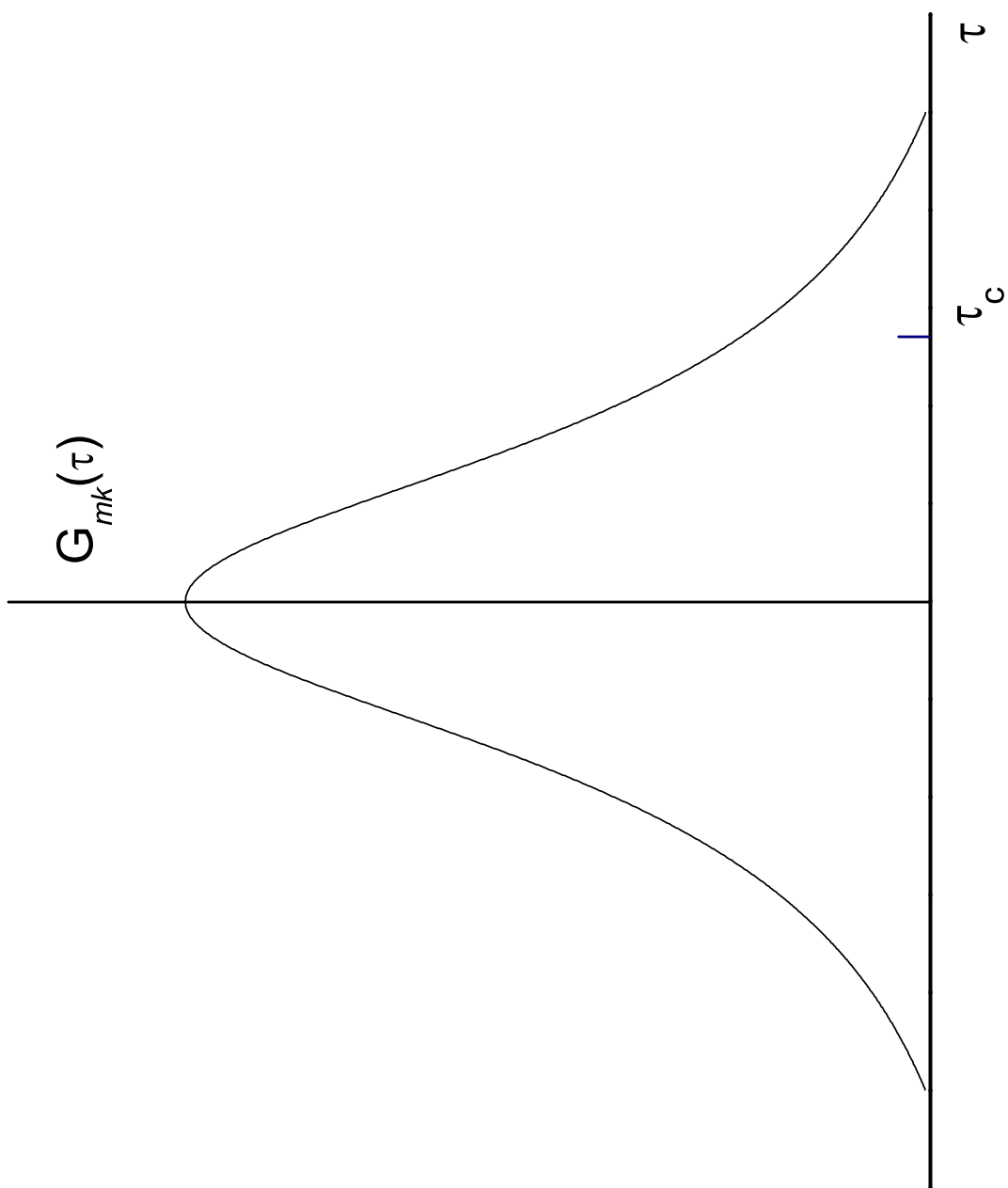


Figure A.1: Typical correlation function.